

Dissertation

# Characterization of acoustic absorbers

ausgeführt zum Zwecke der Erlangung des akademischen Grades  
eines Doktors der technischen Wissenschaften unter der Leitung von

Univ.-Prof. Dr. techn. Manfred Kaltenbacher

E325

Institut für Mechanik und Mechatronik

eingereicht an der Technischen Universität Wien

Fakultät für Maschinenwesen und Betriebswissenschaften

von

Jochen Metzger

Matrikelnummer 1328614

Spengergasse 57/15-16, 1050 Wien

## **Ehrenwörtliche Erklärung**

Ich erkläre ehrenwörtlich, dass ich die vorliegende wissenschaftliche Arbeit selbstständig angefertigt und die mit ihr unmittelbar verbundenen Tätigkeiten selbst erbracht habe. Ich erkläre weiters, dass ich keine anderen als die angegebenen Hilfsmittel benutzt habe. Alle aus gedruckten, ungedruckten oder dem Internet im Wortlaut oder im wesentlichen Inhalt übernommenen Formulierungen und Konzepte sind gemäß den Regeln für wissenschaftliche Arbeiten zitiert und durch Fußnoten bzw. durch andere genaue Quellenangaben gekennzeichnet.

Die während des Arbeitsvorganges gewährte Unterstützung einschließlich signifikanter Betreuungshinweise ist vollständig angegeben. Die wissenschaftliche Arbeit ist noch keiner anderen Prüfungsbehörde vorgelegt worden. Diese Arbeit wurde in gedruckter und elektronischer Form abgegeben. Ich bestätige, dass der Inhalt der digitalen Version vollständig mit dem der gedruckten Version übereinstimmt.

Ich bin mir bewusst, dass eine falsche Erklärung rechtliche Folgen haben wird.

---

**(Unterschrift)**

---

**(Ort, Datum)**

## Kurzfassung

In dieser Arbeit werden Absorber hinsichtlich ihrer akustischen Eigenschaften charakterisiert. Akustische Absorber werden zur Reduktion von Lärm eingesetzt. Solche akustischen Absorber können durch eine Vielzahl von Konzepten realisiert werden. Einerseits existieren aktive Maßnahmen, um Lärm mit Hilfe von elektro-akustischen Methoden zu reduzieren. Auf der anderen Seite stellen passive und damit energieautarke Absorber eine meist kostengünstigere und robustere Alternative zu aktiven Absorbern dar. Passive Absorber können durch resonante Strukturen, beispielsweise ausgeführt als Helmholtz-Resonator, realisiert werden. Alternativ dazu können sie auch aus porösem Material bestehen. Herkömmliche poröse Absorber werden hauptsächlich zur Vermeidung von Lärm im Bereich ab ungefähr 1 kHz verwendet. Hierbei wird die akustische Energie mittels Reibung in Wärme umgesetzt.

Ein wichtiges Werkzeug zur akustischen Charakterisierung stellen Intensitätssonden dar. Durch Intensitätssonden kann mit Hilfe eines Schalldruckmikrofons und einem 3D-Schallschnellesensor der akustische Energiefluss bestimmt werden. In dieser Arbeit wird auf diese Weise das Einfügungsdämmmaß von akustischen Absorbern untersucht. Weiterhin wird eine neuartige, simulationsgestützte Kalibrierungsmethode entwickelt, um alle drei Komponenten des Schallschnellesensors simultan mit Hilfe eines Referenzschallfeldes zu kalibrieren. Dieses Referenzschallfeld wird von einem schwingendem Kolben erzeugt und mittels numerischer Methoden analysiert. Die entstandene Kalibrierungsmethode wird charakterisiert und eine Validierung der Methode präsentiert.

Von äußerster Wichtigkeit ist die Bestimmung des Absorptionsverhaltens von passiven Absorbern als Funktion des Schalleinfallswinkels. Hierzu werden zwei bestehende Methoden implementiert und entsprechend weiterentwickelt. Das erste Verfahren ist eine Subtraktionsmethode im Zeitbereich. Hier werden die Materialeigenschaften durch die Trennung eines einfallenden und reflektierenden Impulses berechnet. Der zweiten Methode liegt die örtliche Fourier Transformation zu Grunde. Im Zuge dessen werden die akustischen Materialeigenschaften durch die Zerlegung des Schallfelds in ebene Wellenkomponenten auf verschiedenen Messebenen bestimmt. Beide Verfahren werden untersucht und Verbesserungen der Methoden vorgestellt. Passive akustische Absorber werden hinsichtlich ihrer akustischen Eigenschaften unter schrägem Schalleinfall charakterisiert und Aussagen über das Absorptionsverhalten abgeleitet. Diese Materialcharakterisierungen stellen einen wichtigen Baustein dar, um ein Verständnis dafür zu entwickeln, an welcher Stelle Absorber platziert werden müssen, um akustische Energie effizient absorbieren zu können. Darüber hinaus können die Materialdaten als Randbedingung für präzise Simulationen realistischer Schallfelder verwendet werden.

Abschließend wird die Entwicklung und Charakterisierung eines akustischen Absorbers für niedrige Frequenzen präsentiert. Durch Anwendung einer massebeladenen Membran kann akustische Energie schmalbandig in mechanische Energie umgewandelt werden, wobei die jeweilige Schwingungsform des Systems einen akustischen Kurzschluss zur

Folge hat. Daraus ergibt sich eine ineffiziente Schallabstrahlung dieser mechanischen Energie einhergehend mit einem hohen Durchgangsdämmmaß des Absorbers. Der passive mechanische Absorber wird charakterisiert und eine Anwendung als Absorberarray zur Absorption schmalbandigen Lärms im Frequenzbereich unter 300 Hz besprochen.

## Abstract

The focus of this thesis is the characterization of acoustic absorbers. Acoustic absorbers are employed to reduce noise and can be realized by means of numerous concepts. Active strategies aim to reduce noise by employing electro-acoustical approaches while passive absorbers present a more cost-efficient and robust alternative. Passive absorbers can be realized by either using resonant structures such as Helmholtz resonators or can be made from porous materials. Traditional porous absorbers are most commonly used for the reduction of noise with frequency components higher than 1 kHz. In porous absorbers, the acoustic energy is transformed into thermal energy by means of friction.

Acoustic intensity probes are crucial tools for acoustic characterization. They consist of a sound pressure microphone and a 3D particle velocity sensor and enable determining the acoustic energy flow. In this thesis, the sound insertion loss of acoustic absorbers is analyzed by means of an acoustic intensity probe. Furthermore, a novel simulation aided calibration method is developed to calibrate all three components of the particle velocity sensor simultaneously by means of a reference sound field. The reference sound field, produced by a moving piston, is investigated by applying numerical calculation methods. The calibration method is then characterized and a validation of the method presented.

In addition to this, two existing measurement methods for characterizing passive acoustic absorber materials under oblique angle of sound incidence are implemented and further improved. The first approach employs subtraction in the time domain, which allows for calculating the properties by separating an incoming and a reflecting impulse. The second method is based on a spatial Fourier transform. Here, the acoustic properties are calculated by decomposition of a sound field into plane wave components on several measurement planes. Both methods are characterized and subsequently improved. A characterization of passive acoustic absorbers in terms of the acoustic properties at oblique angles of sound incidence is performed and the absorption capability of the absorbers identified. The characterization is essential to gain the necessary understanding of where to place which absorber to achieve the optimum absorption of acoustic energy. Moreover, the material data can be used as boundary conditions for a precise simulation of realistic acoustic fields.

Finally, development and characterization of an acoustic absorber for low frequencies is discussed. By applying a mass loaded membrane, acoustic energy can be transformed narrow-bandedly into mechanical energy, which produces an acoustic short circuit. As a consequence, the mechanical energy is not emitted efficiently in the free field, which results in a high sound transmission loss. The passive mechanical absorber is characterized and its application as an absorber array for absorbing narrow band acoustic energy in a frequency range below 300 Hz presented.

## Danksagung

Zuallererst gebührt mein herzlichster Dank Hr. Univ.–Prof. Dr.techn. Manfred Kaltenbacher für die Betreuung dieser Arbeit. Seine kontinuierliche Unterstützung und kompetente Hilfe bei vielen Fragestellungen während meiner Anstellung als Assistent am Institut für Mechanik und Mechatronik haben mir sehr geholfen. In zahlreichen Gesprächen konnte ich mich auf nützliches Feedback verlassen und die Diskussionen waren mir immer sehr hilfreich. Auch der tolle kollegiale Umgang miteinander ist hier zu erwähnen. Darüber hinaus bedanke ich mich für das entgegengebrachte Vertrauen und den Freiraum, die Themengebiete der Dissertation eigenverantwortlich und selbstständig zu bearbeiten.

Außerdem bedanke ich mich bei Prof. Dr.-Ing. Ennes Sarradj und Univ. Prof. Dr.techn. Thomas Bednar für das Interesse an meiner Arbeit und die Übernahme der Gutachten.

Während meiner Zeit am Institut für Mechanik und Mechatronik habe ich das tolle Arbeitsumfeld der dortigen Arbeitsgruppe für Messtechnik und Aktorik sehr genossen und freue mich wirklich außerordentlich, dass ich Teil dieser Gruppe sein durfte. Daher möchte ich mich bei allen Kolleginnen und Kollegen der TU Wien bedanken. Ein besonderer Dank gilt meinem Zimmergenossen Till Kniffka. Die Gespräche mit ihm haben mich nicht nur fachlich sehr bereichert. Weiterhin bedanke ich mich bei Andreas Hüppe, Stefan Zörner, David Tumpold, Kirill Shaposhnikov und Dominik Perchtold für die tolle Unterstützung. Dies gilt ebenfalls für Hendrik Husstedt, welcher mir vor allem bei der Kalibrierung des Schallschnellesensors sehr behilflich gewesen ist. Auch bei den Kollegen Clemens Junger, Stefan Gombots und Felix Gassenmeyer bedanke ich mich für die interessanten Gespräche und Anregungen. Ein ganz großes Dankeschön gilt Frau Ruth Tscherne für Ihre tolle Unterstützung, auch im Privaten, während meiner Zeit in Wien. Auch bei Frau Birgit Pimperl bedanke ich mich für die sorgfältige und zuverlässige Erledigung von organisatorischen Dingen. Ebenfalls gebührt Manfred Neumann, Reinhold Wagner, Johann Schindele, Peter Unterkreuter und Georg Canek ein herzliches Dankeschön für die tolle und hervorragende Mithilfe und Unterstützung bei dem Aufbau verschiedener Messanordnungen und den Durchführungen von Messungen. Danke ebenfalls an Johann Wassermann und Horst Ecker, einerseits für die tolle Zusammenarbeit im Lehrbetrieb und andererseits für die fachliche Diskussion verschiedener Themengebiete.

Ein besonderer Dank gilt meiner Familie, die mich zu jeder Zeit unterstützt hat. Vielen Dank insbesondere meinen Eltern, welche immer an mich geglaubt und mir uneingeschränkt Rückhalt gegeben haben. Ohne diese Unterstützung wäre mein bisheriger Weg in dieser Art und Weise nicht möglich gewesen. Zum Schluss möchte ich mich auch bei meiner Freundin Sandra für ihre tolle und liebevolle Unterstützung während der Zeit meiner Arbeit bedanken. Ich bin froh, sie an meiner Seite zu haben

# Contents

<b>1. Introduction</b>	<b>1</b>
1.1. Motivation	1
1.2. State of the art	2
1.2.1. Calibration of particle velocity sensors in intensity probes	2
1.2.2. Characterization of acoustic absorbers for high frequencies	3
1.2.3. Acoustic Absorbers for low frequencies	5
1.3. Aim of the thesis	7
<b>2. Fundamentals</b>	<b>9</b>
2.1. Sound propagation	9
2.1.1. Propagation of plane waves	10
2.1.2. Propagation of spherical waves	11
2.2. Acoustic intensity and power	12
2.3. Absorption and acoustic surface properties	14
2.3.1. Attenuation mechanism	14
2.3.2. Interaction at an interface	15
2.3.3. Reflection factor and absorption coefficient	17
2.3.4. Modeling of the characteristic field impedance	18
2.4. Spatial Fourier transformation (Fourier acoustics)	20
2.5. Sound field above an acoustic interface	22
2.5.1. Monopole	22
2.5.2. Dipole	23
2.6. Impulse response and transfer function of a LTI-system	24
<b>3. Calibration of particle velocity sensors</b>	<b>27</b>
3.1. Simultaneous calibration method for 3D particle velocity sensors	28
3.1.1. Sensitivity of a sensor's component	29
3.1.2. Analysis of the reference sound field	29
3.1.3. Orientation analysis	33
3.1.4. Implementation of the simultaneous calibration method	34
3.2. Calibration results	42
3.3. Validation of the calibration method	44
3.3.1. Measurement setup for validation measurements	44
3.3.2. Acoustic particle velocity measurements above a vibrating plane	45

*Contents*

<b>4. Characterization of absorbers for high frequencies</b>	<b>48</b>
4.1. Characterization of acoustic surface properties . . . . .	48
4.1.1. Subtraction method (Time domain) . . . . .	48
4.1.2. Spatial Fourier transform method (Wavenumber domain) . . . . .	56
4.2. Acoustic surface properties of absorbers for high frequencies . . . . .	76
4.2.1. Perpendicular sound incidence . . . . .	76
4.2.2. Oblique angles of sound incidence . . . . .	77
<b>5. Absorbers for low frequencies</b>	<b>82</b>
5.1. Working principle of the mechanical absorber . . . . .	83
5.1.1. Theory of a mass loaded plate . . . . .	83
5.2. Unit cell absorber . . . . .	86
5.2.1. Measurement setups for characterization . . . . .	87
5.2.2. Characterization of the unit cell absorber . . . . .	90
5.3. Array absorber . . . . .	93
5.3.1. Measurement setup for array characterization . . . . .	94
5.3.2. Characterization of the absorber array . . . . .	95
<b>6. Conclusion</b>	<b>98</b>
<b>A. Appendix</b>	<b>100</b>
A.1. Modeling of the characteristic field impedance . . . . .	100
A.2. Derivation of Spatial Fourier transform formulations . . . . .	100
A.2.1. Monopole . . . . .	100
A.2.2. Dipole . . . . .	101
A.3. Derivation of the sound field above an acoustic interface . . . . .	102



## Abbreviations

ACC	acceleration sensor
DOF	degree of freedom
EPDM	ethylene propylene diene monomer
ESM	equivalent source method
FE	finite element
FHT	fast Hadamard transformation
IL	insertion loss
IR	impulse response
LOC	location of calibration
LRAMS	locally resonant acoustic meta materials
LSPW	local specular plane wave method
LTI	linear time-invariant
MEMS	micro-electro-mechanical-system
MLS	maximum length sequence
NAH	near field acoustic holography
NFL	near field length
PLA	polylactide
PML	perfectly matched layer
POR	point of reflection
POS	piston on a sphere calibrator
PV	particle velocity sensor
RMS	root mean square
SFT	spatial Fourier transform
SNR	signal to noise ratio
SONAH	statistically optimized NAH
SPL	sound pressure level
STL	sound transmission loss
TF	transfer function
USP	ultimate sound probe

## Notations and Symbols

In this thesis, scalars are represented by normal letters ( $x$ ) and vectors are set bold ( $\mathbf{x}$ ). In general, time-dependent values are denoted with a lowercase, whereas time Fourier transformed variables are indicated with capital letters.

$\nabla$	differential operator
$\partial/\partial t$	partial derivation in respect to time
$*$	symbol for convolution
$\star$	symbol for cross correlation
$\text{Im}(\square)$	imaginary part of $\square$
$\text{Re}(\square)$	real part of $\square$
$\text{arg}(\square)$	argument of $\square$
$\square^T$	transpose of $\square$
$\square^*$	complex conjugate of $\square$
$\tilde{\square}$	spatial Fourier transform of $\square$
$\ \square\ $	vector norm of vector $\square$
$\mathbf{n}$	unit normal vector
$\square_0$	constant part of $\square$
$\square_a$	alternating (acoustic) part of $\square$
$\square_n$	component of $\square$ in direction of $\mathbf{n}$
$\square_{\text{RMS}}$	root mean square value of $\square$
$a$	length of square $A$
$\mathbf{a}$	vector of measured acceleration
$c$	speed of sound
$d$	thickness
$\mathbf{g}$	vector of the local gravity field
$f$	frequency
$f_0$	design frequency
$f_s$	sample frequency
$h$	impulse response
$i$	running index
$k$	wave number
$k_0$	wave number of air
$k_s$	stiffness
$\mathbf{k}$	wave vector
$\mathbf{k}_i$	wave vector of incoming wave
$\mathbf{k}_t$	wave vector of transmitted wave
$\mathbf{k}_r$	wave vector of reflected wave
$m$	complex mass ratio
$m_\square$	mass of element $\square$ per unit area
$n$	order of MLS
$n_{\text{max}}$	phase shifting factor

$n_{ov}$	oversampling factor
$p$	pressure
$p_a$	acoustic pressure
$q$	volume velocity (strength of sound source)
$r_d$	distance sound source–observer/direct sound path
$r_{ref}$	reflected sound path
$t$	time
$\mathbf{u}$	mechanical displacement
$\mathbf{v}$	velocity
$\mathbf{v}_a$	acoustic particle velocity
$A$	area
$C$	amplitude correction factor
$E$	overall mean error
$H$	transfer function
$I$	active intensity
$\mathbf{I}_a$	acoustic intensity
$J$	reactive intensity
$J_\square$	Bessel function of first kind and $\square$ th order
$L$	length of MLS
$M$	total mass per unit area
$N$	number of evaluated frequencies
$P$	acoustic power
$P_a$	time Fourier transformed acoustic pressure
$P_{ab}$	absorbed acoustic energy
$P_i$	incoming acoustic energy
$Q$	volume velocity (strength of a sound source)
$R$	sound pressure reflection coefficient
$R_K$	sound pressure reflection coefficient obtained by using the Ko- matsu model
$R_{SFT}$	sound pressure reflection coefficient obtained by SFT
$RF$	reduction factor
$S$	sensitivity (of the particle velocity sensor)
$STL$	sound transmission loss
$T$	time period
$\mathbf{T}$	transfer matrix
$\mathbf{V}_a$	time Fourier transformed acoustic particle velocity
$V_{dis}$	displaced volume
$V_s$	voltage output of the particle velocity sensor amplifier
$Z$	specific acoustic impedance
$Z_0$	characteristic field impedance
$Z_C$	characteristic impedance
$Z_W$	surface/wall impedance

$\alpha$	sound absorption coefficient
$\alpha'$	attenuation coefficient
$\Gamma$	arbitrary surface
$\delta_{-\square}$	dirac delta function with maximum at $\square$
$\eta$	damping parameter
$\theta_i$	angle of sound incidence
$\theta_t$	angle of transmitted wave
$\vartheta$	radiation angle
$\lambda$	acoustic wavelength
$\rho$	density
$\rho_w$	density of a wall
$\sigma$	flow resistivity
$\tau$	time shift
$\omega$	angular frequency

# 1. Introduction

## 1.1. Motivation

The human auditory system is an astonishing organ of perception. Beating all artificial audio systems, it provides the human body with an outstanding sensor. The human ear is a particularly sensitive sensor which in healthy individuals can typically perceive sound over a wide frequency range (16 Hz to 16 kHz) as well as over a wide acoustic pressure (level) range (0 dB to 120 dB, or 20  $\mu$ Pa to 20 Pa respectively). However, this renders it and consequently us humans particularly sensitive to noise. This disturbing influence on human life can even result in health effects, such as tinnitus and agrypnia [102].

In order to reduce such disturbances, a lot of time and effort is dedicated to finding a suitable silencer for each product, regardless of whether it is for a premium or a budget product. In the design process, the characterization of acoustic absorbers is obligatory in order to gain an understanding of how to best absorb the acoustic energy. In addition to the design of an acoustic absorber, finding the optimum location for where to place the component is also vital for reducing noise efficiently.

While the process of manufacturing materials to absorb acoustic energy at high frequencies is well known and a standard procedure, the sound insulation for sources emitting low frequency noise is still an open topic. For instance, power transformers radiate, due to electromagnetic forces and magnetostriction, noise at very low frequencies in the 100 Hz region. Here, the acoustic wavelength is too large and traditional porous absorbers only have a little effect, if any. The conventional way to overcome this problem is to encapsulate the whole noise source in heavy material to quieten it by means of the mass effect. At these low frequencies what is referred to as metamaterials can be beneficial, as they show more efficiency in terms of absorbing acoustic energy and are lightweight structures. This thesis deals with the characterization of acoustic absorbers, standard porous absorbers for high frequencies and mechanical absorbers for low frequencies. The characterization of absorbers for high frequencies is done by means of a pressure microphone, which is calibrated by the manufacturer. Absorbers for low frequencies are characterized with an intensity probe containing a particle velocity sensor, which is calibrated by means of a novel simulation aided calibration method in this thesis.

## 1.2. State of the art

### 1.2.1. Calibration of particle velocity sensors in intensity probes

A sensor for determining the particle velocity is a very efficient tool for the characterization of acoustic devices. The easiest and most common way to analyze an acoustic particle velocity field in an acoustic intensity measurement is the pp-measurement principle [40] [42]. This method, based on two microphones placed in close proximity to each other is applied to determine the acoustic intensity by means of pressure measurements. Often, condenser microphones are used in the pp-probe which makes the calibration of the probe straightforward since the calibration of microphones, e.g. by means of the reciprocity method [128] is well known. Furthermore, such pressure microphones can be produced inexpensively and are very stable towards environmental influences [129]. However, the particle velocity in the direction of the axis through the two microphones is approximated by means of obtaining the pressure gradient with the two microphones. As mentioned in [40], the accuracy of the sound intensity measurement system strongly depends on the sound field under study. The most relevant error sources [41] in the pp-principle are finite-difference approximation [111], scattering and diffraction [52], and phase mismatch of the microphones [108].

Another principle to determine the acoustic intensity is the pv-measurement principle [53]. Here, as opposed to the pp-principle where two identically sensors are used, two fundamentally different transducers are employed. In the pv-measurement principle, the acoustic particle velocity is determined directly by means of a particle velocity sensor. The most relevant source of errors for determining the acoustic intensity in this setup is a phase mismatch between the two different sensors. As shown in [40] and in particular reactive sound fields, e.g. in the near field of a sound source, this mismatch is critical. Another problem in measuring the sound intensity with the pv-measurement principle is airflow. Distinguishing between the acoustic particle velocity and the velocity of the airflow can be problematic; in order to minimize this effect, windscreens made of foam are used.

The Microflown, which is a Micro-Electro-Mechanical-System (MEMS) device, is a sensor for directly measuring the acoustic particle velocity. A commercial probe (a Microflown sensor in combination with a MEMS pressure microphone) is available [37]. By using an ultimate sound probe (USP), a 3D intensity probe [36] consisting of three components of a 3D particle velocity sensor positioned orthogonally and a pressure microphone, the spatial intensity vector can be obtained. The Microflown sensor itself consists of two tiny strips that are heated by electrical current to an operational temperature of about 300 °C [35]. The resistance of these platinum strips varies with their temperature and the temperature changes if a particle velocity signal affects on them, one wire will be cooler than the other. As a consequence, there is a temperature difference between the wires which alters with the acoustic particle velocity.

However, the calibration of the particle velocity sensor is crucial [54]. Calibration by comparison is not possible as no standard sensor to compare with exists. There is a full bandwidth calibration procedure proposed in [21]. For calibrations at frequencies above

## 1. Introduction

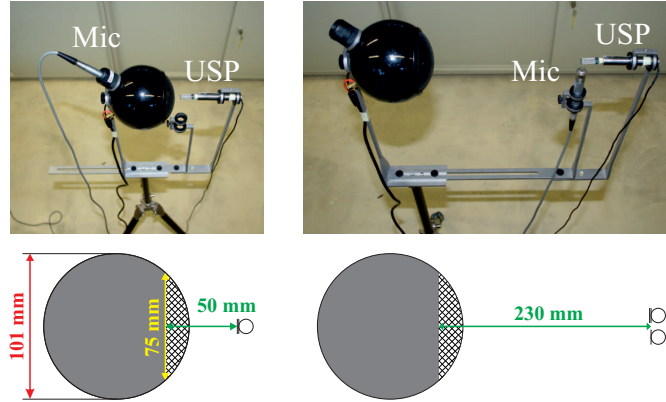


Figure 1.1.: Measurement setup for the piston on a sphere calibrator for low frequencies (left) and high frequencies (right) including its dimensions.

400 Hz the particle velocity sensor is placed in front of a specially designed loudspeaker at nearly the same position as a calibrated reference microphone. The measurement setup for the calibration at low and high frequencies is shown in 1.1. The calibration setup for high frequencies is displayed on the right side of fig. 1.1. This loudspeaker is assumed to be a vibrating circular piston on a rigid spherical baffle where its acoustic radiation impedance can be approximated [127]. This method is extended to low frequencies (20 Hz to 400 Hz, see left side of fig. 1.1) by measuring the acoustic pressure inside the spherical source and placing the sensor directly in front of the moving membrane. The velocity of this membrane is known since at low frequencies it is proportional to the acoustic pressure inside the sphere. This calibration idea is presented as piston on a sphere calibrator (POS) provided by Microflown Technologies. Another method to calibrate a particle velocity sensor by means of a known relation between acoustic pressure and particle velocity is the use of standing wave tubes [68] [112]. These approaches are always limited because of the tube's cut-off frequency. In [56], the sensitivity of a particle velocity sensor is determined by means of near field acoustic holography (NAH) in a frequency range from 400 Hz to 3 kHz with a good congruence to the manufacturer calibration data. Optical techniques are also employed in the calibration process. In [31], photon correlation spectroscopy is used to calibrate the particle velocity sensor. Here, the magnitude of the sensitivity has been calibrated but not the phase information. A calibration method based on a moving rigid enclosure can be found in [32]. Again, only the magnitude response of a particle velocity sensor is investigated.

### 1.2.2. Characterization of acoustic absorbers for high frequencies

In order to obtain precise data for an acoustic field by simulation, the acoustic wave equation with accurate boundary conditions has to be solved. Such an acoustic boundary condition can be the acoustic impedance at the boundary surface or the sound pressure reflection coefficient.

## 1. Introduction

Based on Sabine's formula [110], measurements of the absorbing and scattering properties of a sample in diffuse sound fields can be conducted [6] [7] [8]. However, since the sound absorption coefficient is linked to the absolute value of the sound pressure reflection coefficient, information about the acoustic boundary obtained with such standardized methods in a reverberation room is insufficient. In order to measure the complex acoustic surface properties, several standardized methods can be utilized. By measuring the standing wave ratio [3] as well as the transfer function between the signals of the two microphones in the impedance tube [4], these acoustic properties can be obtained for sound incidence perpendicular to a plane surface. Applying the transfer matrix method described in [9], the transfer matrix of a sample under test can be identified. Here, the sound pressure at four positions (two on the upstream and two on the downstream side of the sample) in a rigid tube needs to be measured. Following these standardized measurement methods, however, only allows for investigating the acoustic properties with perpendicular or random sound incidence. Furthermore, the tube methods assume an excitation by a plane wave. A real sound excitation will never be a perfect plane wave and the cutting process, if at all possible, may change the acoustic behavior.

For all reasons listed above, an in situ method for determining the acoustic properties of a sample, installed in real life situations, can be beneficial. In addition to the methods described in Sec. 4.1.1 and 4.1.2, a large number of investigations can be found in literature. For a detailed overview, the reader is referred to [33]. A two microphone method for obtaining acoustic surface properties at perpendicular [19] and oblique sound incidence [16] [17] [86] exists. Here, two microphones are placed above the sample and problems at frequencies lower than 500 Hz, due to the finite-difference approximation of the particle velocity with the sound pressure measured at the two positions are described. The method is extended [18] by abandoning the plane wave assumption and instead employing the theory proposed in [99] to overcome the problems at low frequencies. The results show good agreement with the theoretical values of a model for frequencies above 300 Hz and an angle of sound incidence of up to  $75^\circ$ . The two microphone method was applied in [71] by using Maximum Length Sequences (MLS) for excitation and a single microphone to measure the sound pressure at two locations above the sample.

A technique based on the equivalent source method (ESM) [135], using a pv-probe is proposed in [105]. In this the sound pressure and the acoustic particle velocity are measured on a single plane in order to obtain the acoustic surface properties of a sample. However, these results can only be obtained for locally reacting materials and thus, the material cannot be investigated as to how the acoustic surface properties change with sound incidence under an oblique angles of incidence. In [103], the finite sample size is taken into account. Here, the results are compared to the ones obtained with the subtraction method (see Sec. 4.1.1) and the statistically optimized near field acoustic holography (SONAH) [45]. It is shown that for small absorber samples and large angles of sound incidence, the finite absorber dimensions are substantial. A method for obtaining acoustic surface properties based on spatial filtering to separate incoming and reflecting sound by using spherical harmonics [89] in combination with two hemispheres is reported in [90].

With the local specular plane wave method (LSPW), the acoustic surface properties are



## 1. Introduction

determined by assuming that the acoustic field can be approximated by a set of two plane waves that represent local specular reflection [63].

Applying not only a sound pressure transducer but also a particle velocity sensor, several pv methods were investigated. In [69], a Microflow *pv*-probe is used to measure the acoustic field impedance in the free field and above a sample under study. A study is presented in [88] where the uncertainty factors, such as sound source, sensor and geometry of absorber are examined. In this paper it was pointed out that the geometry of the sensor as well as the finite sample size lead to errors in determining the acoustic surface properties. In [38] an analysis of existing methods is undertaken. A literature overview can be found in [29]. The reader is referred to this overview for more detailed information on the listed techniques.

### 1.2.3. Acoustic Absorbers for low frequencies

Since the sound absorption of traditional porous materials drops towards the low frequency range, acoustic waves at low frequencies have to be insulated by other materials. The most common way to achieve quieting at low frequencies is to encapsulate the sound source with heavy materials, such as concrete walls. Here, the sound transmission loss (STL) and the insertion loss (IL) are of importance and are mainly governed by the mass law [23]. This law gives the upper limit of a single wall's STL. Thereby, the STL increases with mass, frequency and thickness of the material. Thus, in particular for sound insulation at low frequencies, a high mass is necessary which can lead to problems if a product is bound by a mass limit. One idea to increase STL in a light-weight manner can be found in [64], where a STL-model of a mass loaded plate (a light plate attached with a regular grating of masses) at normal and diffuse sound incidence is presented. Here, the assumption is that the mass loaded plate acts as a normal wall, meaning the damping is defined by the mass law, at frequencies below and above a particular value. At this characteristic frequency, the phase shift between the plate and masses is  $180^\circ$  and the spatial average of the surface velocity in normal direction is zero which results in theory in infinite STL. It is obvious that this approach can only be applied where a pure tone has to be shielded. An STL over a wide frequency range cannot be achieved with a regular grid of equal masses. With a random distribution of masses, an increase of STL in respect to the mass law below 400 Hz is realized [64]. The idea of a regular mass loaded plate was researched in [47] and additional tension [46] was given to the plate to vary the stiffness and therefore the characteristic frequency of the mechanical system. In [27] [122] [123], a panel consisting of multiple cells produced by a membrane on a grid frame is presented. It is shown that the peak of the STL can be tuned by varying the density and the thickness of the membrane and the frame.

Over the last years, a variety of research into materials which absorb acoustic energy more than predicted by the mass law at low frequencies has been conducted; these materials are called metamaterials. Most commonly, the idea of a mass loaded plate is modified and a membrane with an attached mass is built as an unit cell, tuned to a special frequency, and partly arranged to a panel. An overview of these metamaterials can be found in [50]. In [132], measurements and simulations on a metamaterial unit

## 1. Introduction

cell consisting of a mass attached on a membrane are presented. It is found that the STL as a function of frequency shows one peak between two dips (the authors of the paper speak of two peaks and one dip in the transmitted energy). The frequency of the first dip and peak can be shifted, when the attached mass changes. The second dip is not affected by a change in the attached mass. The presented approach, named locally resonant acoustic metamaterials (LRAMs), is extended to an array of cells and stacked arrays are used for a broadband sound reduction [131]. In fig. 1.2, the curve of STL as a function of frequency can be seen for two similar LRAMs (sample 2 and sample 3) and a combination of both. The STL can nearly be doubled at a characteristic design frequency. Furthermore, a broadband STL can be found for a multi-layer panel of different LRAMs.

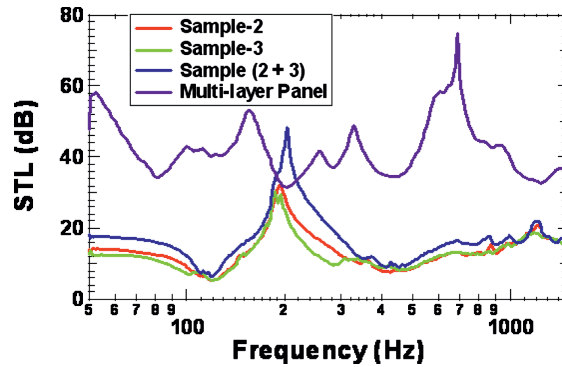


Figure 1.2.: STL of two different LRAM samples and a combination of the two LRAMs along with the STL as a function of frequency of stacked LRAMs [131].

The same approach also can be found as dark acoustic metamaterial [79] or acoustic metasurface [75]. A slightly different method called membrane-constrained acoustic metamaterial [126] uses a stick to constrain the center of a membrane. Some approaches, like the metasurface, use sealed gas or even apply additional pressure [67] to increase the frequency of the STL's peak.

A circular fabricated unit cell is introduced and further mass variations and additional tensions are applied on the membrane and investigated. An increased tension on the membrane has been found to increase the frequency of the dips and the peak in the STL. Moreover, the higher the tension applied to the membrane, the higher the magnitude of the peak [95]. In order to increase the bandwidth of the peak in STL, the mass application on the membrane can be varied. It is shown in [96] that multiple coaxial ring masses on circular membranes gain a broadband sound insulation and a large number of peaks in the STL. In fig. 1.3, an exemplary setup and STL curves of such elements are shown. In contrast to the circular cells, rectangular cells with different masses on the same membrane are investigated in [98]. Here, the STL was found to be multi-peaked because of the different masses applied. By stacking multiple panels of LRAM, the STL was found to be increased not only at the frequency of the peak but also broadband [97]. A circular metamaterial with two membranes attached with circular plates in the center

## 1. Introduction

and connected by an acrylic ring can be found in [130]. Here, three peaks in STL caused by resonances can be observed.

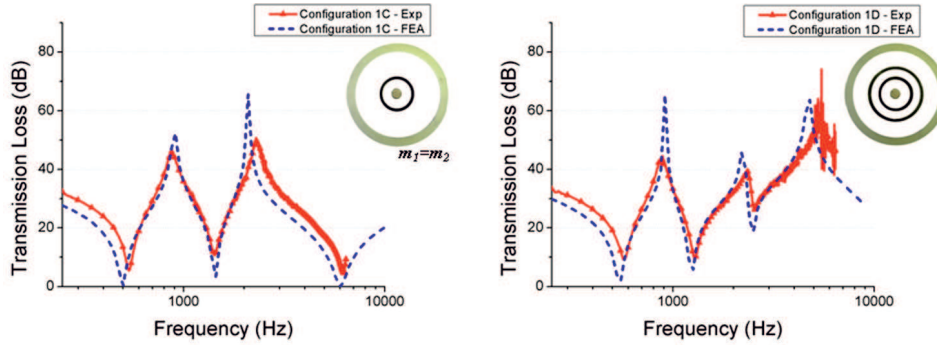


Figure 1.3.: Measurement and simulation of the Sound Transmission Loss of circular membranes with multiple ring masses [96].

The idea was developed to not only insulate the sound at low frequencies, but also to harvest energy with these membrane type metamaterials [106], e.g. by applying a flexible piezoelectric patch on the metamaterials [72].

Many analytical models can be found in literature. Among these are an analytical model for a circular membrane LRAM [30], a model for LRAM with single mass [136], a model for circular and rectangular LRAM [25] with arbitrarily shaped masses [66] and a model for a circular membrane with ring-shaped mass [117].

### 1.3. Aim of the thesis

The introduction has shown that the characterization of acoustic absorbers, especially at oblique angles of sound incidence is of great interest for efficient noise reduction. In this thesis, two methods to achieve the characteristic material data of acoustic absorbers for high frequencies are characterized and substantially improved. Furthermore, a mechanical system to absorb acoustic energy at low frequencies is designed. Subsequently, a novel method to calibrate 3D particle velocity sensors is developed to characterize this mechanical absorber.

In Chap. 2, the theoretical background of the thesis is explained. A brief introduction into the topic of sound propagation is given. Furthermore, the absorption of sound is discussed and the definition of parameters describing the acoustic behavior of surfaces can be found. Chapters 3 to 5 describe tools for the characterization of the acoustic absorption behavior. Chapter 3 deals with the particle velocity sensor and reviews the calibration of such a sensor. In Chap. 4, the characterization of absorbers for high frequencies can be found while Chap. 5 addresses the same for low frequencies. Both chapters are mostly concerned with the measurement setups for the characterization. The focus for the characterization of absorbers for high frequencies is determining the dependency between the acoustic surface properties and the angle of sound incidence

## *1. Introduction*

whereas the absorbers for low frequencies on the other hand are investigated in terms of the sound transmission and insertion loss. Finally, Chap. 5 will present an absorber that has been developed for sound insulation for frequencies below 300 Hz.

## 2. Fundamentals

In this chapter, the basic definitions following [10] and equations will be provided. Furthermore, the basic methods to understand the calculations in the further sections will be given.

### 2.1. Sound propagation

The propagation of sound waves can be described by the time and spatial variation of the density  $\rho$ , the pressure  $p$  and the velocity  $\mathbf{v}$ . Each of these quantities consists of a mean (static) and alternating part, whereas the order of magnitude of the alternating (acoustic) parts are assumed to be much lower than the static ones. The acoustic quantities in this thesis will be denoted with an subscript a. Hence, the acoustic quantities are the acoustic density  $\rho_a$ , the acoustic pressure  $p_a$  and the acoustic particle velocity  $\mathbf{v}_a$ . With the continuity equation, given here in the differential form

$$\nabla \cdot (\rho \mathbf{v}) = -\frac{\partial \rho}{\partial t}, \quad (2.1)$$

the conservation of mass is ensured.  $\partial/\partial t$  denotes the partial derivation with respect to time and  $\nabla$  is the differential operator, e.g. in the Cartesian coordinate system  $\nabla = \left(\frac{\partial}{\partial x}, \frac{\partial}{\partial y}, \frac{\partial}{\partial z}\right)^T$ . The conservation of momentum for a non-viscous fluid reads as

$$\rho \left( \frac{\partial \mathbf{v}}{\partial t} + (\mathbf{v} \cdot \nabla) \mathbf{v} \right) = -\nabla p. \quad (2.2)$$

For linear acoustic wave propagation and since the quantities can be decomposed in their mean and alternating part and additionally assume a quiescent and non-viscous media with density  $\rho_0$ , both basic equations (2.1) and (2.2) read as

$$\frac{\partial \rho_a}{\partial t} + \rho_0 \nabla \cdot \mathbf{v}_a = 0, \quad (2.3)$$

$$\rho_0 \frac{\partial \mathbf{v}_a}{\partial t} + \nabla p_a = 0. \quad (2.4)$$

Applying a time derivative to (2.3), a space derivative to (2.4), combining the two equations and using the linearized pressure-density relation (an adiabatic state is considered and  $c$  is the speed of sound)

$$\frac{p_a}{\rho_a} = c^2, \quad (2.5)$$

## 2. Fundamentals

the wave equation

$$\Delta p_a = \frac{1}{c^2} \frac{\partial^2 p_a}{\partial t^2}. \quad (2.6)$$

is obtained. A detailed derivation of (2.1) – (2.5) can be found in [58] and [65]. Assuming harmonic excitation with frequency  $f$  (angular frequency  $\omega = 2\pi f$ ), the wave equation results in the Helmholtz equation

$$\Delta P_a + k^2 P_a = 0. \quad (2.7)$$

In (2.7),  $P_a$  is the time Fourier transformed of the acoustic pressure and  $k = |\mathbf{k}|$  is the wave number, being the angular frequency divided by the speed of sound. The wave vector is denoted with  $\mathbf{k}$ , e.g. in Cartesian coordinate system  $\mathbf{k} = (k_x, k_y, k_z)^T$ .

### 2.1.1. Propagation of plane waves

If the acoustic pressure only depends on one spatial coordinate, one speaks of a plane wave. This is the most simple model for propagating waves. Here, the acoustic variables only vary along the direction of propagation  $x$ . In 1D the expression

$$p_a(x, t) = \text{Re} \left( \hat{p} e^{j(\omega t - kx)} \right) \quad (2.8)$$

solves the wave equation (2.6) and models a propagating plane wave in  $+x$ -direction with amplitude  $\hat{p}$ . Since, the total acoustic pressure is a superposition of a propagating wave in  $+x$ - and  $-x$ -direction, the acoustic pressure can be expressed by

$$p_a(x, t) = \text{Re} \left( \hat{p}^+ e^{j(\omega t - kx)} \right) + \text{Re} \left( \hat{p}^- e^{j(\omega t + kx)} \right). \quad (2.9)$$

In (2.9),  $\hat{p}^+$  is the amplitude of the wave propagating in  $+x$  and  $\hat{p}^-$  the one propagating in  $-x$ -direction. The concept of a plane wave is of theoretical nature. In reality, only waves in a tube show approximately the form of plane waves. Strictly speaking, plane waves do not have a source and origin, they easily exist with no reduction of level over the propagation distance, because they are a solution of (2.7), where no source term can be found on the right hand side. By using (2.4), the acoustic particle velocity computes to

$$v_a = -\frac{1}{\rho_0} \int \frac{\partial}{\partial x} p_a dt \quad (2.10)$$

$$= \text{Re} \left( \frac{\hat{p}}{\rho_0 c} e^{j(\omega t - kx)} \right). \quad (2.11)$$

The specific acoustic impedance defines the ratio of the complex quantities acoustic pressure and acoustic particle velocity. In case of a plane wave propagating in free space

## 2. Fundamentals

one speaks of the characteristic impedance  $Z_C$ , which is equal to the characteristic field impedance of the propagation medium

$$Z_C = Z_0 = \rho_0 c. \quad (2.12)$$

The characteristic field impedance of air at 20°C is 413 kg/(m<sup>2</sup>s). The relation in (2.12) shows that the acoustic particle velocity and the acoustic pressure are always in phase, if the propagation medium is not lossy. In case of a lossy medium, the density and speed of sound can be modeled as a complex quantity. Furthermore it can be seen that this relationship is a constant with respect to the frequency of the plane wave.

### 2.1.2. Propagation of spherical waves

We assume a spherically symmetric wave spreading out radially from a source into a free space. This assumption implies that the acoustic quantities only depend one spatial variable, the radius from the source  $r$  and time. In this case the spherical coordinate system seems to be preferable and therefore the Laplacian reduces to [40]

$$\Delta p_a = \frac{1}{r} \frac{\partial^2 (r p_a)}{\partial r^2}. \quad (2.13)$$

Applying (2.13) to the wave equation (2.6), the resulting equation can be solved by

$$p_a(r, t) = \frac{g_1(r - ct)}{r} + \frac{g_2(r + ct)}{r}, \quad (2.14)$$

with arbitrary functions  $g_1$  and  $g_2$ , determined by boundary and initial conditions. In (2.14)  $g_1$  corresponds to a propagation in  $+r$ - and  $g_2$  in  $-r$ -direction. In case of a point source, characterized by its volume velocity  $q(t) = \text{Re}(\hat{Q}e^{j\omega t})$  located at the origin of the coordinate system, (2.14) gets

$$p_a(r, t) = \text{Re} \left( \frac{j\omega\rho_0\hat{Q}}{4\pi r} e^{j(\omega t - kr)} \right) = \frac{\omega\rho_0\hat{Q}}{4\pi r} \sin(kr - \omega t). \quad (2.15)$$

A detailed derivation can be found in [65]. Again by using (2.10) the acoustic particle velocity in radial direction computes to

$$V_{a,r} = \frac{P_a}{\rho_0 c} \left( \frac{1 + jkr}{jkr} \right). \quad (2.16)$$

Hence, the specific acoustic impedance of a spherical wave is

$$Z|_{\text{spherical wave}} = Z_0 \frac{jkr}{1 + jkr}. \quad (2.17)$$

## 2. Fundamentals

Taking (2.15) and (2.16) into account it can be observed that the acoustic pressure and the particle velocity are, in contrast to the plane wave propagation, not in phase. For very small distances the phases differ by nearly  $90^\circ$ . In fig. 2.1 the phase shift between the acoustic pressure and the acoustic particle velocity as a function of frequency and distance to the source can be seen. It can be observed that the phase shift gets smaller, the larger the distance to the sound source is. This effect is enhanced by increasing the frequency. If  $kr \gg 1$ , this is at distances, which are large in comparison to the acoustic wavelength  $\lambda$ , this phase shift gets  $0^\circ$  and (2.17) gets the characteristic field impedance of the propagation medium  $Z_0$ . This means that at these distances, where the phase shift is nearly  $0^\circ$  and the specific acoustic impedance gets the characteristic field impedance of the propagation medium, the wave can be treated as a plane wave. This region is called the far field of a sound source, whereas the near field is the region, where the phase shift between the acoustic field quantities has to be taken into account. However, for  $kr = 5$  the magnitude of the specific acoustic impedance is 98.06% of  $Z_0$  and the phase shift between the acoustic pressure and acoustic particle velocity is  $11.31^\circ$ .

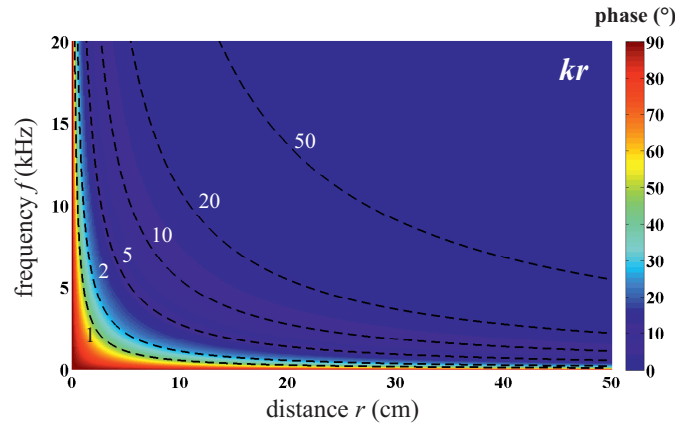


Figure 2.1.: Phase shift between acoustic pressure and acoustic particle velocity in case of a point source as function of frequency and distance to the source with iso-lines, where  $kr$  is constant.

### 2.2. Acoustic intensity and power

The instantaneous acoustic intensity is the product of the acoustic sound pressure and the acoustic particle velocity

$$\mathbf{I}_a(t) = p_a(t)\mathbf{v}_a(t). \quad (2.18)$$



## 2. Fundamentals

For the case of stationary sound fields, the time-averaged sound intensity  $\langle \mathbf{I}_a(t) \rangle_t$ <sup>1</sup> is the quantity of interest. Moreover, since the sound field is harmonic, the complex representation of the acoustic quantities can be used, which leads to [78]

$$\mathbf{I}_a = \mathbf{I} + j\mathbf{J} = \frac{1}{2}(P_a \mathbf{V}_a^*), \quad (2.19)$$

where  $\mathbf{V}_a^*$  denotes the complex conjugate of  $\mathbf{V}_a$ . In (2.19), the complex acoustic intensity is calculated, which consists of the active intensity  $\mathbf{I}$  and the reactive intensity  $\mathbf{J}$ . The reactive intensity describes the non propagating energy flux [51]. It is characteristic of a sound field in which the acoustic pressure and the acoustic particle velocity are present with a phase shift of  $90^\circ$ . This can be found in the near field of a small source, as can be seen in fig. 2.1 or at standing waves, e.g. in a tube excited at one end by a loudspeaker and terminated on the other end by a rigid wall. However, the reactive intensity has no contribution to the radiated power from the sound source into the free field. The acoustic power of a steady sound source spreading sound into the free field can be determined by

$$P = \oint_{\Gamma} \mathbf{I} \cdot d\mathbf{\Gamma} = \oint_{\Gamma} \underbrace{\mathbf{I} \cdot \mathbf{n}}_{I_n} d\Gamma. \quad (2.20)$$

In (2.20)  $\Gamma$  is a surface, which encloses the sound source and  $\mathbf{n}$  is the normal vector of this surface  $\Gamma$ . It can be seen that  $I_n$ , the active intensity normal to a surface surrounding a sound source, is applied to calculate the radiated acoustic power. The sound transmission loss

$$STL = 10 \log \left( \frac{P_i}{P_t} \right) \quad (2.21)$$

describes the logarithmic ratio of incoming and transmitted acoustic energy through a certain area. If the incoming and outgoing area are equal and the intensity across these areas is constant, (2.21) can be calculated via the incoming and transmitted intensity normal to these areas with

$$STL = 10 \log \left( \frac{I_{n,i}}{I_{n,t}} \right). \quad (2.22)$$

The insertion loss

$$IL = L_{P,w} - L_{P,0} \quad (2.23)$$

denotes the reduction of the sound power level  $L_P$  ( $L_{P,w}/L_{P,0}$ : with/without device) at a given location due to the placement of a device in the sound path between the

---

<sup>1</sup> $\langle \mathbf{I}_a(t) \rangle = \frac{1}{T} \int_0^T \mathbf{I}_a(t) dt$ , with the time-period  $T = 1/f$

## 2. Fundamentals

sound source and that location. In case of a propagating plane wave, the active acoustic intensity in direction of propagation (there is only an active part of the intensity and the reactive part vanishes here) can be calculated by

$$\mathbf{I}|_{\text{plane wave}} = \frac{\langle p_a^2(t) \rangle_t}{Z_0} = \frac{p_{a,\text{RMS}}^2}{Z_0}. \quad (2.24)$$

In (2.24)  $p_{a,\text{RMS}}$  is the root mean square (RMS) of the acoustic pressure. In general, the active intensity and therefore the acoustic power is related to the RMS of the acoustic pressure. Hence, the acoustic power of a sound source can be determined by measuring the acoustic pressure in the far field. This builds the basis of the sound power determination in practice, where the acoustic pressure is measured at a number of positions located on a sphere that encloses the sound source. This measurement can be done in an anechoic room [14], over a reflecting plane [11] [12] or in a reverberant environment [13]. Besides the methods measuring the sound pressure applying a far field assumption, the direct measurement of the acoustic pressure and acoustic particle velocity can be beneficial. The determination of acoustic power involving an intensity probe (pp- and pv-probes can be used) are described for discrete measurement points [1] and by scanning the surface [2].

### 2.3. Absorption and acoustic surface properties

In the wave equation (2.6) it is assumed that no losses of acoustic energy occurs. In a more realistic point of view, losses have to be considered. Following [59], there are two essential sources for attenuation. On the one hand, a reduction of the acoustic energy will take place because of medium intrinsic reasons and on the other hand because of reasons associated with the boundary of the medium.

#### 2.3.1. Attenuation mechanism

Attenuation caused by the medium itself can be viscous losses (occur, when there is a relative motion between adjacent parts of the medium), heat conduction losses (caused by the conduction of thermal energy due to a temperature gradient) and losses brought by molecular processes (absorption of energy through conversion of the kinetic energy in stored potential, rotational, heat and vibrational energy). The attenuation in the propagation process is taken into account by introducing a complex wave number

$$k = \frac{\omega}{c} - j\alpha', \quad (2.25)$$

with the attenuation coefficient  $\alpha'$ , which can be applied to (2.8) and (2.15).

## 2. Fundamentals

### 2.3.2. Interaction at an interface

At an interface between two media (and therefore on the boundary of one medium), there can occur several effects. First, there can be reflection, second, the not reflected part of the acoustic wave is absorbed at medium behind the interface, third a part is transmitted through the interface and fourth, a part can be dissipated (acoustic energy conversion to heat energy). The interface between two media can be described via the surface impedance (or wall impedance)

$$Z_W = \frac{P_a}{\mathbf{V}_a \cdot \mathbf{n}} \Big|_{\text{surface}}, \quad (2.26)$$

the complex ratio of acoustic pressure and acoustic particle velocity normal to the interface. This definition of impedance in (2.26) is defined in the frequency domain.

The following considerations about plane wave interaction with an interface in this section is mainly based on the Book of Allard and Atalla [15]. In the following, we assume a planar interface between two fluids (fluid 1 and fluid 2). Furthermore, the interface is large in comparison to the acoustic wavelength and no diffraction at the edge is considered. A schematic of this issue can be seen in fig. 2.2. Additionally, we assume a

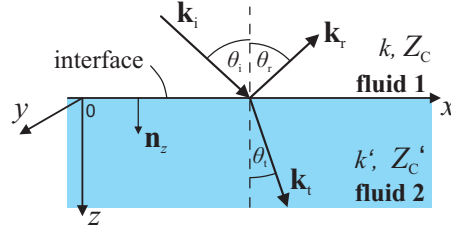


Figure 2.2.: Reflection and refraction at an interface between two fluids with different acoustic properties.

plane wave traveling in fluid 1 in direction of its wave vector  $\mathbf{k}_i = (k_{ix}, k_{iy}, k_{iz})^T$ . The wave number in fluid 1 is  $k$ , whereas the wave number in fluid 2 is  $k'$ . The incoming wave is reflected ( $\mathbf{k}_r = (k_{rx}, k_{ry}, k_{rz})^T$ ) at the interface ( $z = 0$ ) and additionally refracted and transmitted ( $\mathbf{k}_t = (k_{tx}, k_{ty}, k_{tz})^T$ ) since fluid 1 and fluid 2 have different acoustic properties (characteristic field impedances  $Z_C$  and  $Z'_C$ ). The wave vectors are in the same plane ( $y = 0$ ) and therefore the  $y$  component of the vectors vanishes. The wave vector of the incoming wave can be determined with

$$\mathbf{k}_i = \begin{pmatrix} k \sin \theta_i \\ 0 \\ k \cos \theta_i \end{pmatrix} = \begin{pmatrix} k \sin \theta_i \\ 0 \\ k \sqrt{1 - \sin^2 \theta_i} \end{pmatrix}, \quad (2.27)$$

where  $\theta_i$  is the angle of sound incidence at the interface. The angles of the incoming and reflected wave are equal, whereby these angles in the upper half plane are related to the angle of transmission  $\theta_t$  by the law of refraction (Snell's law)

## 2. Fundamentals

$$k \sin \theta_i = k' \sin \theta_t. \quad (2.28)$$

The wave vectors of the reflected and transmitted waves by using (2.28) and  $|\mathbf{k}_t| = k'$  are given by

$$\mathbf{k}_r = \begin{pmatrix} k \sin \theta_i \\ 0 \\ -k \cos \theta_i \end{pmatrix} \quad \mathbf{k}_t = \begin{pmatrix} k \sin \theta_i \\ 0 \\ \sqrt{k'^2 - k^2 \sin^2 \theta_i} \end{pmatrix}. \quad (2.29)$$

The surface impedance [15] following (2.26) with  $\mathbf{n} = \mathbf{n}_z$  can be computed with

$$Z_W = Z(z=0) = \frac{Z'_C k'}{k_{tz}} \left[ \frac{Z'_C \frac{k'}{k_{tz}} - jZ(z_1) \cot(k_{tz} z_1)}{Z(z_1) - jZ'_C \frac{k'}{k_{tz}} \cot(k_{tz} z_1)} \right]. \quad (2.30)$$

Thereby the impedance at  $z = z_1$  is known and denoted by  $Z(z_1)$ .

### Wall impedance of an infinite fluid

Following (2.30) it can be seen that at a perpendicular sound incidence  $\theta_i = 0^\circ$  at an infinite fluid 2 ( $\frac{k'}{k_{tz}} = 1$ ,  $Z(z_1) = Z'_C$ ;  $\forall z_1 > 0$ ), the wall impedance is equal to the characteristic field impedance of fluid 2

$$Z_W|_{\theta_i=0^\circ} = Z'_C. \quad (2.31)$$

The wall impedance for an oblique angle of sound incidence can be calculated by

$$Z_W(\theta_i) = \frac{Z'_C}{\cos \theta_t}. \quad (2.32)$$

By using (2.28), the wall impedance in (2.32) gets

$$Z_W(\theta_i) = \frac{Z'_C}{\sqrt{1 - \left(\frac{k}{k'}\right)^2 \sin^2 \theta_i}}. \quad (2.33)$$

### Wall impedance of a hard backed fluid with thickness $d$

In reality, absorbers are mostly backed by a rigid wall, so fluid 2 is assumed to be backed by an impervious rigid wall at  $z_1 = d$ . This corresponds to a flat hard backed absorber with thickness  $d$ . Therefore, the specific acoustic impedance at  $z_1$  is infinity and the wall impedance by using (2.30) computes to

## 2. Fundamentals

$$Z_W = -jZ'_C \frac{k'}{k_{tz}} \cot(k_{tz}d). \quad (2.34)$$

Again for a perpendicular sound incidence (2.34) gets

$$Z_W|_{\theta_i=0^\circ} = -jZ'_C \cot(k'd). \quad (2.35)$$

The wall impedance for oblique angles of sound incidence can be derived by inserting (2.29) into (2.34) and thus the wall impedance at oblique sound incidence of a hard backed fluid reads as

$$Z_W(\theta_i) = -jZ'_C \frac{1}{\sqrt{1 - \left(\frac{k}{k'}\right)^2 \sin^2 \theta_i}} \cot \left( k'd \sqrt{1 - \left(\frac{k}{k'}\right)^2 \sin^2 \theta_i} \right). \quad (2.36)$$

### 2.3.3. Reflection factor and absorption coefficient

A more concrete quantity than the surface impedance is the sound pressure reflection coefficient defined as the ratio of the reflected and incoming amplitude of the acoustic pressure. The sound pressure reflection coefficient at the interface in fig. 2.2 computes to [15]

$$R = \frac{Z_W \cos \theta_i - Z_C}{Z_W \cos \theta_i + Z_C}. \quad (2.37)$$

A quantity carrying less information as the wall impedance or the sound pressure reflection coefficient is the sound absorption coefficient

$$\alpha = \frac{P_{ab}}{P_i} = 1 - |R|^2, \quad (2.38)$$

defined as the ratio of absorbed acoustic power  $P_{ab}$  and power of the incoming acoustic wave  $P_i$ . In the calculation of the absorption coefficient the phase of  $R$  is removed. However, there are the following theoretical cases in which the incoming acoustic power is totally reflected or absorbed.

1. In case of a sound hard interface, the acoustic particle velocity normal to the interface vanishes.  $Z_W \rightarrow \infty$ ,  $R = 1$  and  $\alpha = 0$ .
2. A sound soft interface describes an interface, where the acoustic pressure is zero.  $Z_W = 0$ ,  $R = -1$  and  $\alpha = 0$ .

## 2. Fundamentals

3. At a totally absorbing interface, the reflecting wave vanishes and all energy is absorbed in the medium behind the interface.  $Z_W = Z_C$ ,  $R = 0$  and  $\alpha = 1$ .

Since the wall impedance can be split into a real part  $\text{Re}(Z_W)$  and imaginary part  $\text{Im}(Z_W)$  and insert (2.37) into (2.38) some important conditions for the sound absorption coefficient

$$\alpha = \frac{4Z_C \text{Re}(Z_W) \cos \theta_i}{(\text{Re}(Z_W) \cos \theta_i + Z_C)^2 + (\text{Im}(Z_W) \cos \theta_i)^2} \quad (2.39)$$

can be derived. The passivity condition has to be fulfilled and therefore, the sound absorption coefficient cannot be negative

$$\alpha \geq 0 \quad \Rightarrow \quad \text{Re}(Z_W) \in \mathbb{R}^{\geq 0}. \quad (2.40)$$

Thus, the real part has to be a positive real number for angles of sound incidence of  $0 \leq \theta_i \leq 90^\circ$ . Furthermore, the sound absorption coefficient has to be smaller or equal to 1, and therefore the following condition has to be fulfilled

$$\alpha \leq 1 \quad \Rightarrow \quad (\text{Re}(Z_W) \cos \theta_i + Z_C)^2 + (\text{Im}(Z_W) \cos \theta_i)^2 \geq 0 \quad \Rightarrow \quad \text{Im}(Z_W) \in \mathbb{R}. \quad (2.41)$$

Hence, the argument of the wall impedance only can be in a range between  $-\pi/2$  and  $\pi/2$ .

### 2.3.4. Modeling of the characteristic field impedance

We assume fluid 1 now to be air with a real valued characteristic field impedance  $Z_C = Z_0$  and wave number  $k = k_0 = \frac{\omega}{c}$ . Fluid 2 is an absorber with thickness  $d$  and sound hard termination at  $z = d$ . To calculate the wall impedance at the interface with (2.36) the characteristic field impedance  $Z'_C$  and the wave number in the absorber  $k'$  have to be known. Such characteristics can be modeled by using the Delany–Bazley model [39], Miki model [85] or the Komatsu model [61]. The description of the models can be found in the appendix A.1. These empiric models only use the flow resistivity as input and are later used to validate measurement results.

In fig. 2.3 the magnitude and phase of the wall impedance calculated with the different models are displayed. It can be seen that the Delany & Bazley and the Miki models give similar results. The Komatsu model differs a little from both. Furthermore, the surface impedance of an air layer of the same thickness is shown. At low frequencies a similar behavior of all curves can be observed (all curves show spring like behavior) until the first resonance is reached. The surface impedance shows resonant behavior because of the rigid termination at the back. These resonance peaks of the curve representing the material behavior are lower of course and shifted in frequency because of the higher speed of sound in the medium in comparison to the air layer. If  $k_{tz}$  is close to  $k'$  for a

## 2. Fundamentals

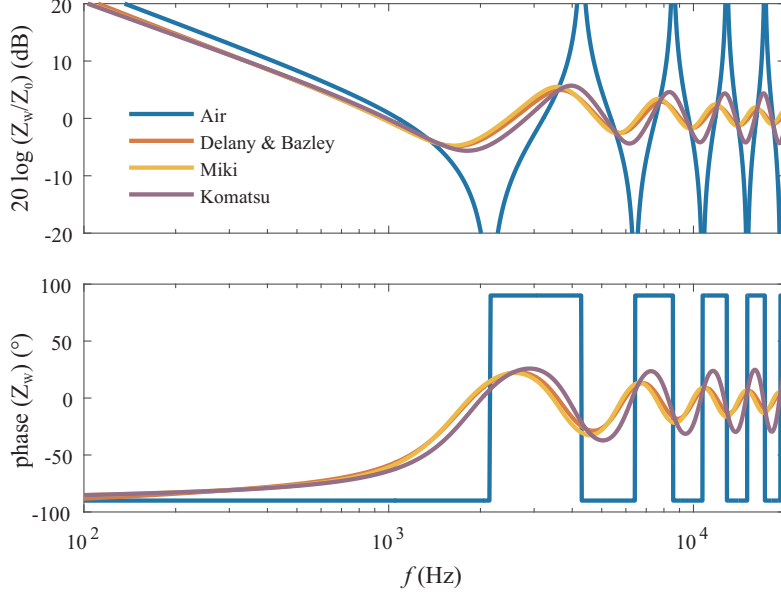


Figure 2.3.: Magnitude and phase of the surface impedance at perpendicular sound incidence to the interface between fluid 1 and fluid 2 calculated with (2.35) using the different approaches to model the fluid 2 with (A.1) – (A.4) ( $d = 40$  mm,  $\sigma = 8 \text{ kPas/m}^2$ ) in comparison to the surface impedance calculated of the same layer of air ( $Z'_C = Z_0$ ,  $k' = k_0$ ).

large range of angles  $\theta_i$  the wall impedance given by (2.36) is close to (2.35) and weakly depends on the angle of sound incidence. Fluid 2 then is called a locally reacting medium. This means that the response (acoustic particle velocity) at the surface of the medium only depends on the pressure at the surface and not on the angle of sound incidence [137]. Beyond that, the response of a certain point on the surface is independent of the response of other points. As a consequence, the surface impedance is no more a function of the angle of sound incidence and can be seen as constant for all angles of incidence (calculated with (2.35)), since the speed of sound inside the medium is lower than the one in air. This results in a wave propagation in the medium perpendicular to the surface. The simplification to treat a medium as a locally reacting one is valid in case of small angles of sound incidence and thin porous materials [15]. It falls short, if the flow resistivity is low or the angles of sound incidence are large [60] [62]. However, if the surface behaves locally reacting, the measurement of its acoustic absorption properties is very easy. The surface impedance has to be only measured at perpendicular sound incidence as described in the first part of Sec. 1.2.2 and the acoustic behavior can be predicted for oblique angles of sound incidence.

In fig. 2.4 the real and imaginary part of the sound pressure reflection coefficient for different angles of sound incidence are shown. The solid lines represent locally reacting behavior of the surface, whereas the dashed lines are calculated don't making this simplification and using (2.36) for the wall impedance. It can be clearly seen that for the

## 2. Fundamentals

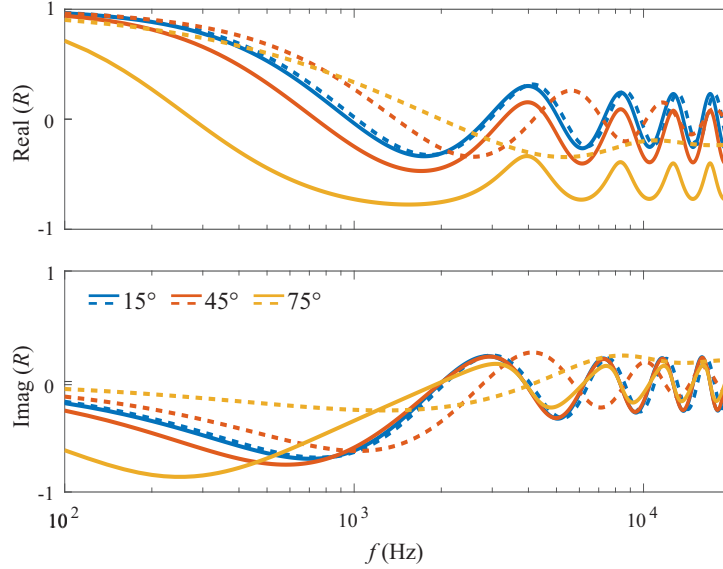


Figure 2.4.: Sound pressure reflection coefficient as a function of frequency for different angles of sound incidence  $\theta_i$  calculated with (2.37). The solid lines represents a locally reacting material using (2.35) and the dashed lines are calculated with (2.36) by applying the Komatsu model employing (A.3) and (A.4) with  $d = 40$  mm and flow resistivity  $8 \text{ kPas/m}^2$ .

angle of sound incidence  $15^\circ$  there is slightly no difference in the sound pressure reflection coefficient by using the simplification of a locally reacting behavior. In contrast, the difference grows with higher angles of sound incidence.

There is no consistent convention in literature how to name the behavior of a surface, which is not locally reacting. Allard and Attala [15] introduced the non-locally reacting behavior. In [62] this behavior was split to be able to distinguish between surfaces who scatter sound (non-locally reacting) and who do not (extensively reacting). The extensively reacting surface is characterized, that the wall impedance is a function of the angle of sound incidence, whereas the wall impedance of a non-locally reacting surface is additionally a function of the spatial vector. An example for such a behavior is a periodic diffuser, which can be found in [62]. Furthermore the extensively reacting behavior can be found as bulk reacting [24] or laterally reacting surfaces [20]. In this thesis only locally and non-locally reacting behavior without scattering (called extensively reacting behavior in [62]) are considered.

### 2.4. Spatial Fourier transformation (Fourier acoustics)

The measurement technique presented in Sec. 4.1.2 is based on the spatial Fourier transformation of an acoustic pressure field above an acoustic surface. Therefore, the Fourier transformation has to be introduced. For a detailed introduction the reader is



## 2. Fundamentals

referred to [127]. The well known concept of a Fourier transform not only can be applied on a time–signal but also can be used to calculate the spatial Fourier transform in 1D

$$\tilde{F}(k_x) = \int_{-\infty}^{\infty} F(x)e^{-jk_x x} dx \quad (2.42)$$

of a spatial function  $F(x)$ . The spatial function  $F(x)$  is denoted with a capital letter here, since it is assumed as a time Fourier transformed signal. The inverse Fourier transformation is defined as

$$F(x) = \frac{1}{2\pi} \int_{-\infty}^{\infty} \tilde{F}(k_x)e^{jk_x x} dk_x. \quad (2.43)$$

Assuming a  $z$ –plane with a spatial distribution  $F(x, y)$  and performing a spatial Fourier transformation in 2D (2.42) has to be done in two dimensions  $x$  and  $y$ . Thus, the spatial Fourier transformation gets

$$\tilde{F}(k_x, k_y) = \int_{-\infty}^{\infty} \int_{-\infty}^{\infty} F(x, y)e^{-j(k_x x + k_y y)} dx dy. \quad (2.44)$$

Now a radial symmetric distribution on the  $z$ –plane is assumed, such as the function  $F(r)$  only depends on the radial variable  $r$ . Such a distribution plays an important role in acoustics particularly since most of the sound fields above an acoustic surface show a radial symmetric distribution of the acoustic pressure (if the wall impedance is not a function of the spatial vector). The spatial Fourier transform in polar coordinates computes to

$$\tilde{F}(k_r) = 2\pi \int_0^{\infty} F(r)J_0(k_r r)r dr, \quad (2.45)$$

whereas the inverse Fourier transformation is defined as

$$F(r) = \frac{1}{2\pi} \int_0^{\infty} \tilde{F}(k_r)J_0(k_r r)k_r dk_r. \quad (2.46)$$

In (2.45) and (2.46)  $J_0$  is the Bessel function of first kind and 0th order. The derivation of the simplification in (2.45) is known as the Fourier–Bessel transform and can be found in [44]. For a more practical aspect the spatial Fourier transform of a pressure distribution in space can be seen as a decomposition into plane wave components, and is used to calculate the acoustic sound field near a source by means of acoustic holography [49].

## 2. Fundamentals

The idea of near field acoustic holography is to extrapolate fields from a measured spatial distribution of acoustic pressure in a plane to another. The extrapolation of a known spatial Fourier transformed function  $\tilde{F}(k_x, k_y, z_0)$  at the plane  $z_0$  can be expressed by [127]

$$\tilde{F}(k_x, k_y, z) = \tilde{F}(k_x, k_y, z_0)e^{-jk_z(z-z_0)}. \quad (2.47)$$

### 2.5. Sound field above an acoustic interface

Now, the sound field above an acoustic interface (see Sec. 2.3.2) excited by a sound source (e.g. a spherical sound source, see Sec. 2.1.2) can be described. In this section, the sound field above an acoustic interface is computed using the spatial Fourier transform presented in Sec. 2.4. First, the sound field caused by a monopole and second caused by a dipole is considered. The sound field is assumed to show a symmetry in the  $xy$ -plane, so the sound field only depends on  $r = \sqrt{x^2 + y^2}$  and  $z$ . In fig. 2.5 the schematic for the following calculations can be seen. The sound field is excited by a sound source located at  $\mathbf{x}_s = (z_s, r_s)^T$ . The direct distance to the observer  $\mathbf{x}_o = (z_o, r_o)^T$  is denoted with

$$r_d = \|\mathbf{x}_o - \mathbf{x}_s\| = \sqrt{(z_o - z_s)^2 + (r_o - r_s)^2}. \quad (2.48)$$

Furthermore, there are the following relations between the spatial Fourier transformed acoustic pressure at the observer and at the origin with  $\tilde{P}_{a,\text{dir}}$  being the direct wave and  $\tilde{P}_{a,r}$  the reflected one

$$\tilde{P}_{a,\text{dir}}(0) = \tilde{P}_{a,\text{dir}}(z)e^{-jk_z z} \quad (2.49)$$

$$\tilde{P}_{a,r}(z) = \tilde{P}_{a,r}(0)e^{-jk_z z} \quad (2.50)$$

The sound reflecting plane will be at  $z = 0$  and therefore, the direct and reflected sound pressure are linked by the sound pressure reflection coefficient  $\tilde{R}$

$$\tilde{P}_{a,r}(0) = \tilde{P}_{a,\text{dir}}(0)\tilde{R}. \quad (2.51)$$

#### 2.5.1. Monopole

In case of a free radiation the time Fourier transformed acoustic pressure can be computed from (2.15) by

$$P_a = \frac{j\omega\rho_0\hat{Q}}{4\pi r_d}e^{-jkr_d}. \quad (2.52)$$

## 2. Fundamentals

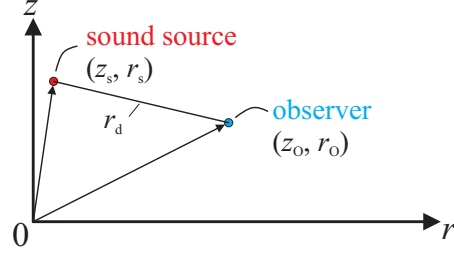


Figure 2.5.: Schematic for the calculation of the sound field above an acoustic interface.

If the sound source is located at  $r_s = 0$ , the spatial Fourier transform of (2.52) is [104]

$$\tilde{P}_{a,\text{dir}} = j\omega\rho_0\hat{Q} \left( \frac{j}{2\sqrt{k^2 - k_r^2}} e^{j\sqrt{k^2 - k_r^2}|z_o - z_s|} \right)^* . \quad (2.53)$$

A derivation of (2.53) can be found in the appendix A.2.1. It can be seen in (2.53) that the spatial spectrum has a pole at  $k_r = k$ . The time Fourier transform of the acoustic pressure above an acoustic surface at  $z = 0$  (the sound pressure reflection coefficient of the interface is  $\tilde{R}$ ) can be calculated by inserting (2.52) and (2.53) in (A.16)

$$P_a = \frac{j\omega\rho_0\hat{Q}}{4\pi r_d} e^{-jk r_d} + \frac{\omega\rho_0\hat{Q}}{2\pi} \int_0^\infty \frac{1}{2\sqrt{k^2 - k_r^2}} e^{-j\sqrt{k^2 - k_r^2}(z_s + z_o)} k_r \tilde{R}(k_r) J_0(r k_r) dk_r . \quad (2.54)$$

### 2.5.2. Dipole

Since a dipole consists of two monopoles  $Q_1$  and  $Q_2$  located at  $\mathbf{x}_{s1} = (z_{s1}, r_{s1})^T$  and  $\mathbf{x}_{s2} = (z_{s2}, r_{s2})^T$  with equal strength  $\hat{Q}$  (and different sign), separated by the distance  $d$ , the acoustic pressure can be computed by [65]

$$P_a = j\omega\rho_0\hat{Q} \left( \frac{1}{4\pi r_1} e^{-jk r_1} - \frac{1}{4\pi r_2} e^{-jk r_2} \right) , \quad (2.55)$$

with the distance between sound source and observer  $r_{1/2}$ .

We assume  $Q_1$  and  $Q_2$  located on the  $z$ -axis as can be seen in fig. 2.6. In this special case, the expression in the brackets in (2.55) can be replaced by the derivation of the Green's functions of both monopoles with respect to  $z_s$  and a multiplication with  $d$  and therefore, the acoustic pressure can be computed by [104]

$$P_a = j\omega\rho_0\hat{Q}d \frac{\partial}{\partial z_s} \left( \frac{1}{4\pi r_d} e^{-jk r_d} \right) \quad (2.56)$$

$$= \frac{j\omega\rho_0\hat{Q}d(jk r_d + 1)(z_o - z_s)}{4\pi r_d^3} e^{-jk r_d} . \quad (2.57)$$

## 2. Fundamentals

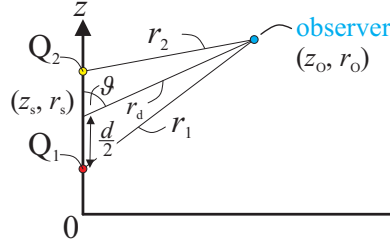


Figure 2.6.: Sketch of dipole consisting of two monopoles.

By introducing the radiation angle  $\vartheta$  ( $\cos \vartheta = (z_o - z_s)/r_d$ ), the acoustic pressure reads as

$$P_a = \frac{j\omega\rho_0\hat{Q}d(jkr_d + 1)}{4\pi r_d^2} \cos \vartheta e^{-jkr_d}. \quad (2.58)$$

Again, the time Fourier transform of the acoustic pressure above the interface can be calculated by using (A.16) with (2.57) and (A.12)

$$\begin{aligned} P_a &= \frac{j\omega\rho_0\hat{Q}d(jkr_d + 1)(z_o - z_s)}{4\pi r_d^3} e^{-jkr_d} \\ &- \frac{j\omega\rho_0\hat{Q}d}{4\pi} \int_0^\infty \tilde{R} e^{-j\sqrt{k^2 - k_r^2}(z_s + z_o)} J_0(rk_r) k_r dk_r. \end{aligned} \quad (2.59)$$

## 2.6. Impulse response and transfer function of a LTI-system

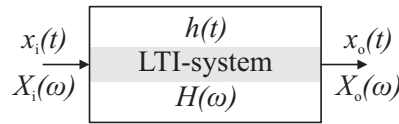


Figure 2.7.: LTI-system with impulse response  $h(t)$  and transfer function  $H(\omega)$ .

Since the measurement techniques described in Chap. 4 are mainly based on determining the impulse response (IR), a short introduction in the topic is given. For a detailed introduction the reader is referred to [48]. We consider a linear and time-invariant (LTI) system (see fig. 2.7). The LTI system is described by its impulse response  $h(t)$  and the corresponding complex transfer function (TF)  $H(\omega)$ . Both represent the same information content since the IR can be transformed into the TF with the Fourier transform and vice versa the IR can be calculated from the TF with the inverse Fourier transform. However, the system's output  $x_o(t)$  (in frequency domain  $X_o(\omega)$ ) in time domain is a convolution (denoted with  $*$ ) of the input signal  $x_i(t)$  and the IR and in frequency domain a simple multiplication of the Fourier transformed input signal  $X_i(\omega)$  and the TF

## 2. Fundamentals

$$x_o(t) = (x_i * h)(t) = \int_{-\infty}^{\infty} x_i(\tau)h(t - \tau)d\tau \quad (2.60)$$

$$X_o(\omega) = X_i(\omega)H(\omega). \quad (2.61)$$

The IR and TF can be determined by deconvolution and division with

$$h(t) = x_o(t) * x_i^{-1}(t) \quad (2.62)$$

$$H(\omega) = \frac{X_o(\omega)}{X_i(\omega)}. \quad (2.63)$$

In (2.62),  $x_i^{-1}(t)$  is the signal with the spectrum  $1/X_i$  and is called matched filter. When the power spectral density of  $X_i(\omega)$  is constant [94], the following relation holds

$$\frac{1}{X_i(\omega)} = \text{const. } X_i^*(\omega) \quad (2.64)$$

$$x_i^{-1}(t) \equiv x_i(-\cdot)(t). \quad (2.65)$$

By using the relation in (2.65) the IR in (2.62) can be computed with

$$h(t) = (x_o * x_i(-\cdot))(t) = \int_{-\infty}^{\infty} x_o(\tau)x_i(t + \tau)d\tau, \quad (2.66)$$

which is the cross correlation

$$h(t) = (x_o \star x_i)(t). \quad (2.67)$$

Hence, the IR can be obtained with an arbitrary input signal and a cross correlation with the output signal, when the power spectral density of the input signal is constant. The benefit of using a MLS as input signal is that there is a very efficient cross-correlation algorithm available. The MLS [76] [125] are special classes of binary sequences. The deterministic MLS sequence of length  $L = 2^n - 1$  with the order of the sequence  $n$  shows a constant frequency spectrum and is produced by a binary shift register. The brilliant characteristic of a MLS is the fact that the auto correlation shows a dirac-delta impulse and (2.66) in case of an excitation with a MLS  $x_{i,\text{MLS}}(t)$  as input results in [94]

$$\underbrace{(x_{i,\text{MLS}} * h \star x_{i,\text{MLS}})}_{x_o}(t) \approx (\delta_i * h)(t). \quad (2.68)$$

In (2.68)  $\delta_i$  is the dirac delta function shifted by  $i$  times the length of the MLS-sequence with  $i = 0, \pm 1, \pm 2, \dots$  the order of the dirac delta series. The outcome is the wanted IR

## 2. Fundamentals

convolved with a series of dirac delta pulses. To be able to separate the IR from (2.68), the IR has to be decayed within the time period  $L\Delta t$  ( $\Delta t$  is the sample time of the data aquisition). Therefore, the length  $L$  of the MLS has to be chosen sufficient long. Calculating (2.68) with an conventional algorithm,  $(2^n - 1)^2$  multiplications are required, whereas using the fast Hadamard transformation (FHT) [28] only  $n2^n$  summations and subtractions are needed. Therefore, the FHT is an efficient tool to determine the IR of a LTI system excited by a MLS-signal.

### 3. Calibration of particle velocity sensors

This chapter deals with the calibration of particle velocity sensors. The calibration, in particular the phase calibration is very important in measuring the sound intensity. For demonstration a phase mismatch between the sensor for acoustic pressure and acoustic particle velocity  $\varphi_{pv}$  is considered. According to (2.19), the active intensity with a phase mismatch computes to

$$\begin{aligned}\dot{\mathbf{I}} &= \frac{1}{2} \text{Re} \left( P_a \mathbf{V}_a^* e^{-j\varphi_{pv}} \right) \\ &\approx \mathbf{I} + \varphi_{pv} \mathbf{J}.\end{aligned}\tag{3.1}$$

In (3.1) it can clearly be seen that the active intensity and hence the acoustic power with a phase mismatch using (2.20)

$$\dot{P} \approx P + \varphi_{pv} \int_{\Gamma} \mathbf{J} \cdot d\Gamma\tag{3.2}$$

strongly depends on the sound field under test, since there will be a remaining not compensated phase mismatch in every case, even with a good calibration. For a detailed derivation of (3.1) the reader is referred to [40]. However, if  $\mathbf{J} \gg \mathbf{I}$ , there can be expected a significant error by determining the acoustic power with pv-probes even if the phase mismatch is small. This results in errors, if measurements are carried out in the near field of a source but it can be stated that the phase calibration is not critical if the measurements are done in the far-field. Since the measurements presented in Sec. 5.2.1 are carried out with a Microflown USP in an reactive sound field in the near field of a sound source, the calibration of the particle velocity sensor is crucial. The sensitivity of a Microflown sensor, which measures the acoustic particle velocity depends on the frequency. The sensor shows the highest sensitivity at frequencies around 200 Hz. The sensitivity drops to lower frequencies due to the thermal layer on the wires. At higher frequencies, the sensitivity decreases due to thermal diffusion (it takes time for heat to travel from one wire to the other) and the thermal mass (temperature of the wires cannot vary at infinite speed)[121]. This frequency behavior of the sensitivity can be modeled by an electric circuit [36] [113], which can be seen in the left part of fig. 3.1. The magnitude of the complex Sensitivity  $S$  can be approximated with

$$|S| = \frac{S_0}{\sqrt{1 + \left(\frac{f_1}{f}\right)^2} \sqrt{1 + \left(\frac{f}{f_2}\right)^2} \sqrt{1 + \left(\frac{f}{f_3}\right)^2} \sqrt{1 + \left(\frac{f_4}{f}\right)^2}}.\tag{3.3}$$

### 3. Calibration of particle velocity sensors

In (3.3)  $f_1$ ,  $f_2$ ,  $f_3$  and  $f_4$  are the characteristic magnitude corner frequencies associated to the high pass ( $R1$  &  $C1$ ,  $R4$  &  $C4$ ) and low pass filters ( $R2$  &  $C2$ ,  $R3$  &  $C3$ ) and  $S_0$  is an amplitude constant (given in V/(m/s)). The approximation of the sensitivity's phase computes to

$$\arg(S) = \arctan\left(\frac{c_1}{f}\right) - \arctan\left(\frac{f}{c_2}\right) - \arctan\left(\frac{f}{c_3}\right) + \arctan\left(\frac{c_4}{f}\right), \quad (3.4)$$

where  $c_1$ ,  $c_2$ ,  $c_3$  and  $c_4$  are phase corner frequencies being approximately the same corner frequencies of (3.3). An exemplary magnitude and phase response of the sensitivity can be seen in the right part of fig. 3.1.

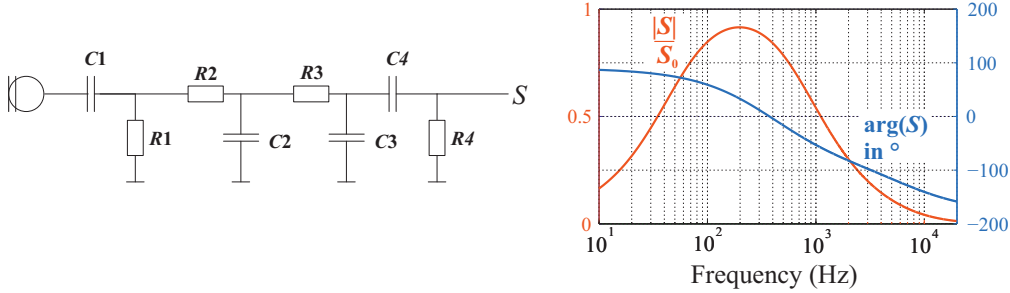


Figure 3.1.: Model of the Microflow sensor's sensitivity. Left: electric circuit. Right: exemplary magnitude and phase response as a function of frequency (calculated with (3.3) and (3.4) using  $f_1 = 66$  Hz,  $f_2 = 487$  Hz,  $f_3 = 4987$  Hz,  $f_4 = 190$  Hz,  $c_1 = 50$  Hz,  $c_2 = 402$  Hz,  $c_3 = 14599$  Hz,  $c_4 = 190$  Hz).

There are some drawbacks in the conventional calibration technique with the POS. First, the acoustic particle velocity affecting the sensor has to be calculated from the measured acoustic pressure and the estimated impedance of the loudspeaker, where measurement and estimation errors can occur. Second, the calibration cannot be done over the whole frequency range of interest at once and third, the calibration of all three components of the particle velocity sensor has to be accomplished sequentially. Furthermore, the manufacturer of the USP only gives the correction curves by default in form of a calibration report containing the corner frequencies  $f_1$ ,  $f_2$ ,  $f_3$ ,  $f_4$ ,  $c_1$ ,  $c_2$ ,  $c_3$  and  $c_4$  and the amplitude constant  $S_0$ , which are results of the calibration using the POS and a model-fit. The correction curves produced by the model only estimates the frequency behavior of the particle velocity sensor. Thus an own calibration of the particle velocity sensor is surely preferred.

#### 3.1. Simultaneous calibration method for 3D particle velocity sensors

In contrast to the calibration method employing the POS, the method described in this section is first a simultaneous calibration technique, providing the sensitivities of



### 3. Calibration of particle velocity sensors

all three components of the particle velocity sensor, second does not need any anechoic conditions and third is not restricted to a specific frequency range. The simulation aided calibration method uses a acoustic particle velocity field in front of a moving circular plane as a reference sound field to obtain the sensitivity of each component.

#### 3.1.1. Sensitivity of a sensor's component

To calibrate one of the three components of a particle velocity sensor ( $\text{dir} = 1,2,3$ ), the output of the sensor's component  $V_{s,\text{dir}}$  has to be compared to the acting acoustic particle velocity on the component  $\mathbf{V}_a \cdot \mathbf{n}_{\text{dir}}$  in direction of the sensor's component  $\mathbf{n}_{\text{dir}}$ . If the acting acoustic particle velocity is known, the sensitivity of the component can be computed with

$$S_{\text{dir}} = S_{r,\text{dir}} + jS_{i,\text{dir}} = \frac{V_{s,\text{dir}}}{\mathbf{V}_a \cdot \mathbf{n}_{\text{dir}}}, \quad (3.5)$$

where the sensitivity can be split into the real  $S_{r,\text{dir}}$  and imaginary part  $S_{i,\text{dir}}$ . Thus, the sensitivities of all three components can be determined simultaneously, if additionally to the acoustic particle velocity at the location of calibration (LOC) the orientation of the particle velocity sensor with respect to the orientation of the acoustic particle velocity vector is known. In the simultaneous calibration method, the acoustic particle velocity vector  $\mathbf{V}_a$  is obtained by using finite element (FE) simulation data of a reference sound field and the orientation  $\mathbf{n}_{\text{dir}}$  of the sensor is measured by means of a 3D acceleration sensor [81].

#### 3.1.2. Analysis of the reference sound field

To obtain the acoustic particle velocity vector (orientation and value) in the reference sound field acting on a component of a particle velocity sensor during the calibration process, a study of the sound field is obligatory. This study can be found in [83] and was done by using the multiphysics software of CFS++ based on the FE method [58] [120]. The axially symmetric simulation setup for the calculation of the reference sound field can be seen in fig. 3.2. This simulation setup consists of an excitation line with length  $r_p$ , which represents the excitation via a moving circular plane and a propagation region, which models the air in front of the plane. The propagation region is surrounded by a perfectly matched layer (PML) [57] for modeling free radiation. Moreover, an observation point 10 mm in front of the excitation line at the line of symmetry can be seen. This will be the LOC, where the particle velocity sensor is being calibrated, see Sec. 3.2. In the implementation of the simultaneous calibration method described in Sec. 3.1.4, a piston is used to produce the reference sound field. Hence, to take diffraction on the edge of the piston into account, a part of the piston is modeled, which can be seen as a rigid boundary condition (sound hard) on the edge of the circular plane. The analysis of the acoustic particle velocity field above the circular plane is done by the investigation of the acoustic particle velocity relative to the velocity  $\mathbf{V}_p \cdot z$  of the excitation since the

### 3. Calibration of particle velocity sensors

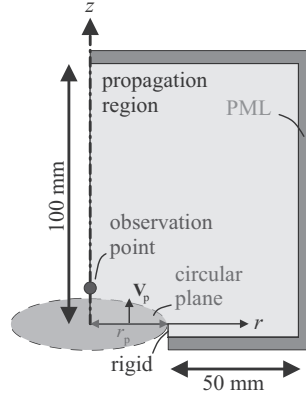


Figure 3.2.: Axially symmetric simulation setup for the calculation of the reference sound field in front of a moving circular plane with radius  $r_p$ .

problem is linear and does not depend on the amplitude of excitation.  $\mathbf{z}$  is the unit vector in  $z$ -direction. This relative acoustic particle velocity computes to

$$v_{\text{rel}} = \frac{\mathbf{V}_a \cdot \mathbf{n}_{\text{dir}}}{\mathbf{V}_p \cdot \mathbf{z}}, \quad (3.6)$$

where  $\mathbf{n}$  denotes the direction of the acoustic particle velocity.

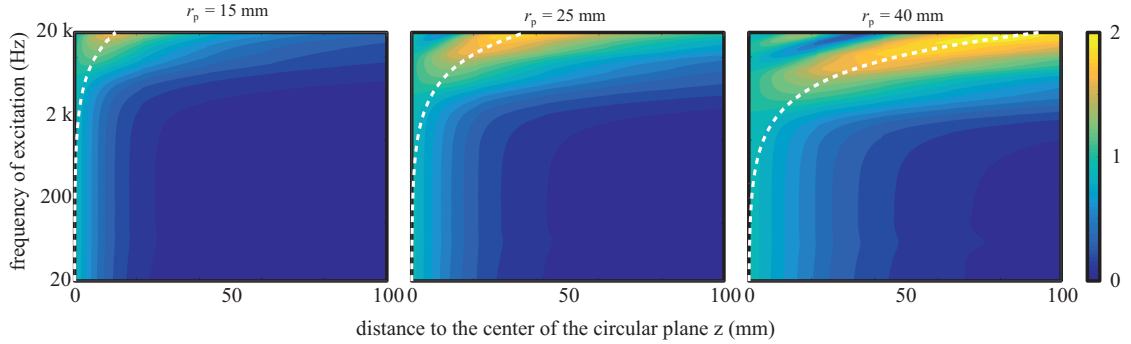


Figure 3.3.: Amplitude of the relative acoustic particle velocity  $|v_{\text{rel}}|$  calculated with (3.6) as a function of frequency of excitation and the distance to the circular plane. The dashed line is the near field length of a piston in an infinite wall with the same radii.

The acoustic particle velocity on the axis of symmetry only shows a  $z$ -component, since this is a symmetry condition. This relative acoustic particle velocity on the symmetry axis for different radii of the circular plane calculated with (3.6) is shown in fig. 3.3. Moreover, the near field length (NFL) of a moving piston in an infinite plane wall calculated following [70] is displayed. This only can be an estimation of the NFL here,

### 3. Calibration of particle velocity sensors

since the moving plane is not located in an infinite plane baffle, but is surrounded with air, but it should be used here for a better understanding. The higher the frequency of excitation, the larger is the NFL. The larger the radius of the moving plane, the larger is the NFL at the same frequency. It can be observed that the amplitude of the relative acoustic particle velocity in front of the plane can be higher than 1 due to near field effects (interference), which means that the acoustic particle velocity is larger than the surface velocity of the excitation. During the calibration process, location errors in placing the sensor can occur. Therefore, the best distance to calibrate the probe can be found, where the gradient of the reference field is a minimum. An indicator might be the sum over all frequencies of interest of the absolute gradient of the relative velocity amplitude on the axis of symmetry

$$G_1 = \frac{1}{N|\mathbf{V}_p \cdot \mathbf{z}|} \sum_{i=1}^N \left| \frac{\partial}{\partial z} |\mathbf{V}_a(f_i) \cdot \mathbf{z}| \right|, \quad (3.7)$$

where  $N$  is the number of evaluated frequencies ( $f_i, i = 1, \dots, N$ ) and  $\mathbf{V}(f_i)$  the acoustic particle velocity at frequency  $f_i$ . In fig. 3.4  $G_1$  is shown for different radii of the plane. The factor  $G_1$  decreases with increasing distance to the plane for all radii. At distances smaller than 20 mm,  $G_1(r_p = 40 \text{ mm})$  shows the smallest values in comparison to both other curves. For a larger distance  $G_1(r_p = 40 \text{ mm})$  is higher than the others and  $G_1(r_p = 15 \text{ mm})$ , the curve for the smallest radius can be found to be the one with the smallest values. All in all the distance to the circular plane has to be chosen as large as possible to reduce problems caused by inaccurate placing the sensor in the reference sound field. In case of small calibration distances, the sound field generated with the largest radius is advantageous.

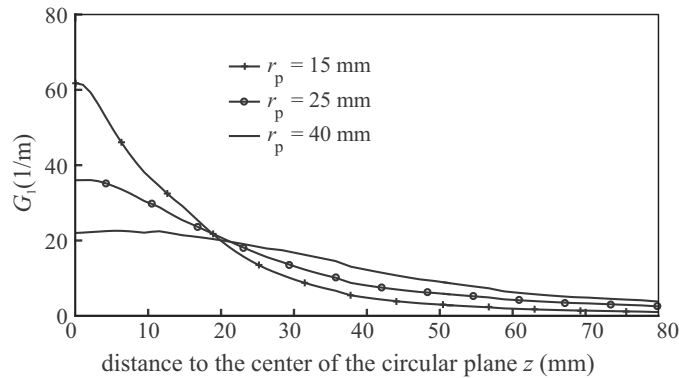


Figure 3.4.: Sum of absolute gradient of the relative acoustic particle velocity  $G_1$  calculated with (3.7) and  $N = 500$ ,  $f_1 = 20 \text{ Hz}$  and  $f_N = 20 \text{ kHz}$ .

A second indicator, where the best LOC is, might be the summation of the acoustic particle velocity amplitudes

### 3. Calibration of particle velocity sensors

$$G_2 = \frac{1}{N |\mathbf{V}_p \cdot \mathbf{z}|} \sum_{i=1}^N |\mathbf{V}_a(f_i) \cdot \mathbf{z}|. \quad (3.8)$$

The higher the amplitude of the acoustic particle velocity at the LOC, the better is the signal to noise ratio (SNR). In fig. 3.5  $G_2$  as a function of the distance to the center of the plane is shown. It can be seen that  $G_2$  decreases with growing distance to the plane with all radii of the excitation plane. Furthermore,  $G_2$  is higher for a larger plane radius, because of interference in the near field and, therefore higher amplitudes in front of the plane. To conclude, the analysis of the reference sound field shows that there is no perfect location to place the sensor since there is at any LOC a trade off by a smaller gradient of the amplitude with larger distances to the center of the plane, to avoid errors in the determined sensitivity as a result of an inaccurate position and a smaller SNR with growing distances to the plane.

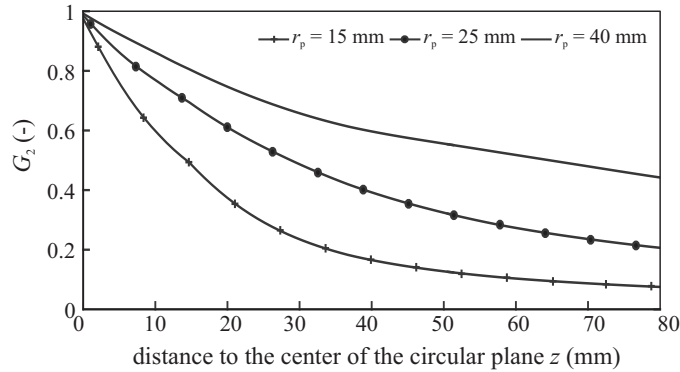


Figure 3.5.: Sum of the relative acoustic particle velocity  $G_2$  calculated with (3.8) and  $N = 500$ ,  $f_1 = 20$  Hz and  $f_N = 20$  kHz.

Nevertheless, a reference sound field generated by a larger excitation surface seems to be more beneficial for the calibration process in a distance up to 20 mm in front of the plane, since the sound field shows the lowest value  $G_1$  and the highest  $G_2$ . However, the highest gradients in the acoustic particle velocity amplitude at higher frequencies can be observed in the sound field with the excitation radius of 40 mm. Therefore, it seems to be reasonable to perform the calibration with different sound fields and merge the obtained sensitivities by averaging the results of each measurement setup. In our implementation presented in Sec. 3.1.4, the LOC will be at a distance of 10 mm in front of the circular plane's center. In fig. 3.6 the real and imaginary part of the relative acoustic particle velocity as a function of the excitation frequency can be seen. At frequencies below 2 kHz the imaginary part of the acoustic particle velocity is nearly zero and therefore the acoustic particle velocity is dominated by its real part. It can be observed that the amplitude is higher below 2 kHz for larger radii of the excitation. At higher frequencies above 2 kHz the acoustic particle velocity at the LOC is very sensitive regarding changes in the frequency of excitation.

### 3. Calibration of particle velocity sensors

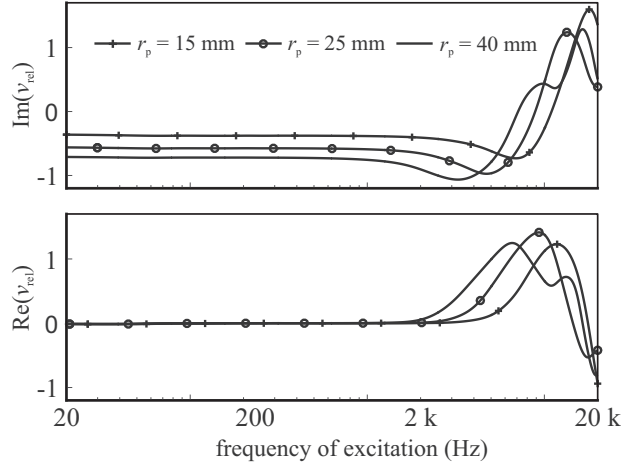


Figure 3.6.: Real and imaginary part of the relative acoustic particle velocity  $v_{\text{rel}}$  at the LOC 10 mm in front of the plane.

Additional to the frequency dependency of the magnitude of the acoustic particle velocity due to the nature of the reference sound field, the surface velocity to generate the reference sound field in the implementation of the calibration method is provided by a moving piston mounted on a vibration exciter (see Sec.3.1.4). Furthermore, two different piston materials will be used, so the frequency response when the surface velocity is not being controlled to be constant over frequency will depend on the material and geometry of the mounted piston, as can be seen in fig. 3.8.

#### 3.1.3. Orientation analysis

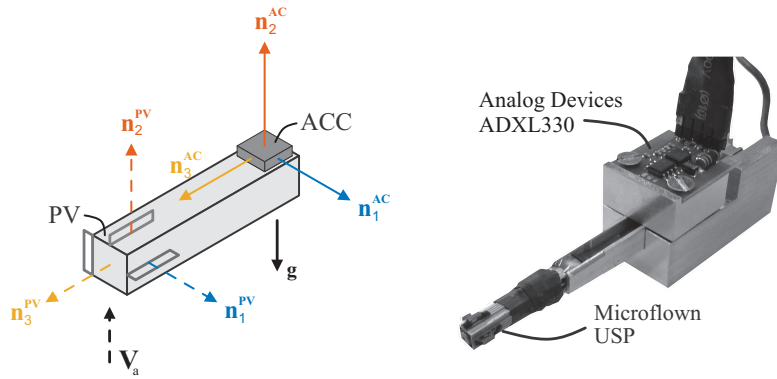


Figure 3.7.: Left: 3D particle velocity sensor (PV) equipped with a 3D acceleration sensor (ACC). Right: Microflowm USP equipped with an Analog Devices ADXL330.

To calculate the sensitivities of the sensor's components with (3.5), the orientation of the

### 3. Calibration of particle velocity sensors

sensor with respect to the particle velocity sensor has to be known. Since the LOC is on the axis of symmetry  $z$ , the acoustic particle velocity points in the same direction as the surface velocity on the circular plane. To identify the orientation of the sensor in relation to the acoustic particle velocity at the LOC, the orientation of the sensor in relation to the surface velocity has to be found. In the following investigations a homogeneous local gravity field  $\mathbf{g}$  acting in  $z$ -direction is assumed. Moreover, we assume the particle velocity sensor equipped with a 3D-acceleration sensor, whereas the three components of the acceleration sensor and the particle velocity sensor are equally orientated as depicted in the left part of fig. 3.7. With the 3D-acceleration sensor, the acceleration vector  $\mathbf{a}$  can be obtained. Thus, the acting acoustic particle velocity on each component of the sensor can be determined with [82]

$$\mathbf{V}_a \cdot \mathbf{n}_{\text{dir}}^{\text{PV}} = \frac{-\mathbf{a} \cdot \mathbf{n}_{\text{dir}}^{\text{ACC}}}{\mathbf{g} \cdot \mathbf{z}} \mathbf{V}_a \cdot \mathbf{z}. \quad (3.9)$$

#### 3.1.4. Implementation of the simultaneous calibration method

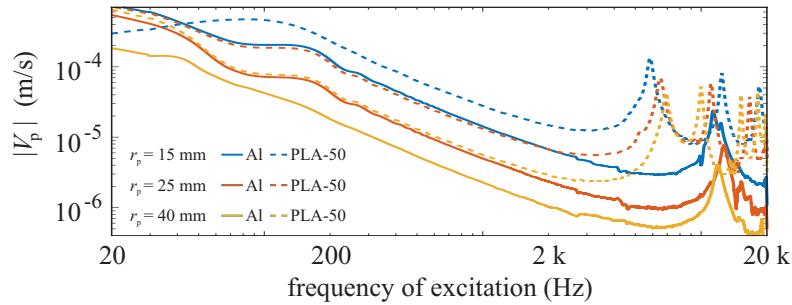


Figure 3.8.: Measured magnitude of the surface velocity with a constant excitation voltage as a function of the excitation frequency (dashed curves; PLA-50; solid curves: Aluminium pistons).

The calibration method proposed in the preceding section is implemented by means of a Microflow USP as a 3D particle velocity sensor and an Analog devices ADXL330 as a 3D acceleration sensor. The calibration was done in an ordinary room without any anechoic conditions. The resulting measurement system can be seen in the right part of fig. 3.7. The reference sound field is generated by means of a moving piston. Pistons made of aluminum and PLA-50 with different radii ( $r_p = [15 \text{ mm}, 25 \text{ mm}, 40 \text{ mm}]$ ) and height 100 mm are mounted on an electrodynamic vibration exciter BK4809 driven by a Power Amplifier BK2718. In total there are six different pistons and hence, six different calibration setups with different mechanical resonance frequencies available. The excitation of the vibration exciter can either be done with a sine sweep or in a harmonic way with a sine signal of a single frequency. The surface velocity is measured on the moving front side at a point 5 mm out of center by means of a laser vibrometer and is assumed to be constant over the surface, perpendicular to the moving surface and orientated

### 3. Calibration of particle velocity sensors

anti-parallel to the local gravity field. The magnitude of the surface velocity measured on top of the six pistons with a constant excitation voltage in form of a sweep signal [83] applied to the vibration exciter as a function of the excitation frequency can be seen in fig. 3.8. The frequency range up to 5 kHz can be found without resonances in all configurations. The system with the aluminum piston (solid line) shows one resonance frequency in the frequency range of interest, whereas three resonance frequencies can be found at the system with the plastic piston (dashed line). The first resonance peak of the plastic pistons can be found to be at first at the piston with smaller radius, while the second and third resonance appear at first at the piston with the largest radius. The resonance peaks of the system with the aluminum piston can all be found in a frequency range around 10 kHz. However, it can be observed that the magnitude of the plastic pistons is higher due to the lower density of PLA-50 in comparison to aluminum (and hence, a lower mass with the same dimensions). Additional to the possibility exciting

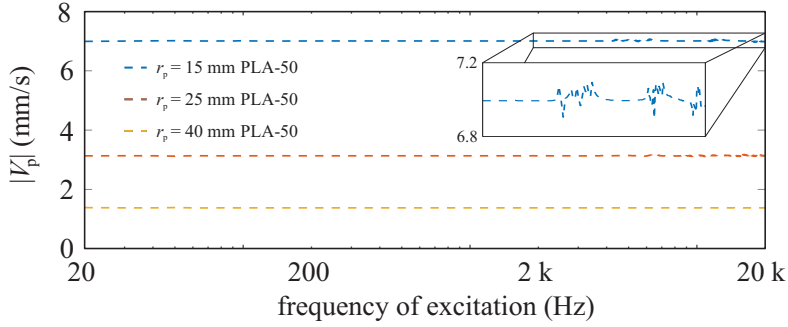


Figure 3.9.: Measured magnitude of the surface velocity with a variable excitation voltage to control the magnitude as a function of the excitation frequency.

the shaker with a constant voltage amplitude, the surface velocity can be controlled to show a constant magnitude over the excitation frequency [81]. Here, the magnitude response of the system is reversed and furthermore, the magnitude was readjusted with a simple P-controller. The resulting magnitude of the systems with the plastic pistons can be seen in fig. 3.9. Here the magnitude can be determined to be constant over the frequency. Small deviations can be detected at the resonance frequencies of the system.

#### Calibration of the 3D acceleration sensor

For determining the sensitivity of the 3D acceleration sensor ADXL330, the system of linear equations

$$\underbrace{\begin{bmatrix} V_{11} & V_{21} & V_{31} \\ \vdots & \vdots & \vdots \\ V_{1n} & V_{2n} & V_{3n} \end{bmatrix}}_{[V]} = \underbrace{\begin{bmatrix} a_{11} & a_{21} & a_{31} & 1 \\ \vdots & \vdots & \vdots & \vdots \\ a_{1n} & a_{2n} & a_{3n} & 1 \end{bmatrix}}_{[a]} \cdot \underbrace{\begin{bmatrix} S_1 & 0 & 0 \\ 0 & S_2 & 0 \\ 0 & 0 & S_3 \\ S_{10} & S_{20} & S_{30} \end{bmatrix}}_{[S]} \quad (3.10)$$

### 3. Calibration of particle velocity sensors

has to be solved. In (3.10)  $[V]$  is the matrix of voltages measured at the acceleration sensor,  $[a]$  the matrix of accelerations and  $[S]$  the system matrix containing the sensitivities ( $S_1, S_2, S_3$ ) of the three components including the offsets ( $S_{10}, S_{20}, S_{30}$ ), where  $n$  is the number of performed measurements. With  $n \geq 2$  one can solve for the system matrix by using the least square method

$$[S] = \left( [a]^T [a] \right)^{-1} [a]^T [V] \quad (3.11)$$

and hence determine the sensitivities of each component of the acceleration sensor. The previous described calibration of the acceleration sensor was done by using  $n = 6$  measurements with

$$[a] = \begin{bmatrix} 1 & 0 & 0 & 1 \\ 0 & 1 & 0 & 1 \\ 0 & 0 & 1 & 1 \\ -1 & 0 & 0 & 1 \\ 0 & -1 & 0 & 1 \\ 0 & 0 & -1 & 1 \end{bmatrix} 9.81 \text{ m/s}^2. \quad (3.12)$$

The obtained sensitivities of the acceleration sensor by using (3.11) and (3.12) can be found in tab. 3.1.

Table 3.1.: Sensitivities of the acceleration sensor ADXL330 determined using (3.11) and (3.12) with  $g = 9.81 \text{ m/s}^2$ .

<b>Component dir</b>	<b>1</b>	<b>2</b>	<b>3</b>
<b>Sensitivity</b> $S_{\text{dir}}$ (V/g)	0.325	0.335	0.320
<b>Offset</b> $S_{\text{dir } 0}$ (V/g)	1.625	1.643	1.613

#### Spatial orientation of the moving piston

To identify the orientation of the surface velocity in relation to the local gravity field, the acceleration sensor is mounted on the surface of the piston. The measured acceleration signal when moving the piston shows a constant  $\mathbf{a}_c$  and alternating  $\mathbf{a}_a$  part. The constant part caused by the local gravity field and the alternating part caused by the motion of the piston. The angle between both acceleration vectors computes to

$$\alpha_{\text{dev}} = \arccos \left( \frac{\mathbf{a}_c \cdot \mathbf{a}_a}{\|\mathbf{a}_c\| \|\mathbf{a}_a\|} \right) \quad (3.13)$$

and was found to be in the range of  $180^\circ \pm 1^\circ$  and therefore the surface velocity can be assumed to be anti-parallel in respect to the local gravity field.



### 3. Calibration of particle velocity sensors

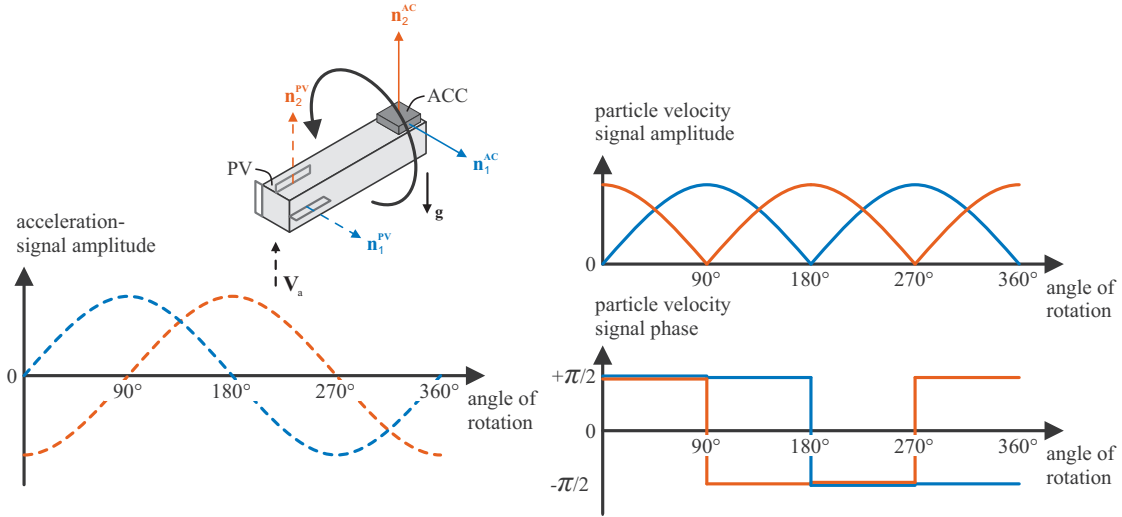


Figure 3.10.: Amplitude and phase of the sensors' signal when the particle velocity sensor and the acceleration sensor are turned around axes 3 (blue: component 1, orange: component 2). The phase of the particle velocity sensor's signal differs by  $\pi$ , when the acoustic particle velocity signal switches from a positive to a negative value.

#### Spatial orientation of the sensors

To analyze the spatial orientation of both sensor's component to each other and to verify the assumption that the axes of both sensors are equally orientated ( $\mathbf{n}_{\text{dir}}^{PV} = \mathbf{n}_{\text{dir}}^{ACC} = \mathbf{n}_{\text{dir}} \forall \text{dir} = 1, 2, 3$ ), the USP equipped with the ADXL330 is rotated around each pair of axes in the reference field. In case of an ideal reference field for both sensors and a perfect anti-parallelism between both fields, a perfect orthogonality between the single sensor's components and a perfect parallelism between the pairs of axes, the expected signals as a function of the rotation angle have to be sine signals and shifted to each other. As an example, the measurement system depicted in fig. 3.7 is turned around the axes marked with  $\mathbf{n}_3$ . The expected sensor signals as a function of rotation angle can be seen in fig. 3.10. Since the acceleration sensor measures a constant quantity, only the amplitude can be analyzed. In theory, the acceleration sensor's signal follows a sine function and there is a shift of  $90^\circ$  between the two components' signal of the acceleration sensor (e.g. component 1 (blue) and component 2 (red) as displayed in fig. 3.10). The amplitude of the particle velocity sensor's signal follows an absolute value of a sine function, whereby a phase shift of  $\pi$  can be expected, where the acoustic particle velocity switches from a positive to a negative value. The orientation analysis has been performed three times, so the measurement system was turned around the axes 1, 2 and 3. Each measurement was repeated ten times with an angle resolution of  $0.5^\circ$  and the result in case of an angle between two axes are given as a mean value of the ten identified angles and with the confidence limits of 99%. The measurements to obtain the spatial orientation of the

### 3. Calibration of particle velocity sensors

sensors have been performed during the work for a bachelor thesis [55] and have been reported in [80].

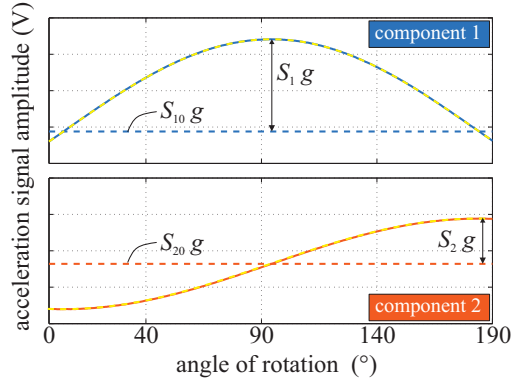


Figure 3.11.: Measured amplitude of the acceleration sensor’s signal (component 1 (blue) and component 2 (red)) while turning the measurement system around  $\mathbf{n}_3$  as sketched in 3.10. The yellow line represents the sine fit of the signals.

**3D Acceleration sensor** The analysis of the acceleration signal can easily be done by means of a sine-fit. Thereby, the phase shift between the amplitude of two signals as a function of frequency is determined. In fig. 3.11 the acceleration signal’s amplitude of component 1 (blue) and component 2 (red) at a rotation of  $190^\circ$  around  $\mathbf{n}_3$  as sketched in fig. 3.10 can be seen. The sine-fitting process works well, since the local gravity field can be assumed to be homogeneous in a small operation range used here for the orientation analysis. The sine functions show nearly no deviation to the measured data. As expected, the amplitude as a function of the rotation angle shows the behavior displayed in fig. 3.10. Since the starting angle of the rotation can be chosen arbitrarily, the function might be shifted. For instance, the acceleration signal is zero at component 1 at an angle of rotation of about  $0^\circ$  since the local gravity field is perpendicular to the component’s axis  $\mathbf{n}_1^{\text{ACC}}$ , whereas the amplitude is maximum when  $\mathbf{n}_1^{\text{ACC}}$  and  $\mathbf{g}$  are orientated parallel. This is at a rotation angle of about  $90^\circ$ .

Table 3.2.: Angles between the components of the ADXL330.

Angles between $\mathbf{n}_i^{\text{ACC}}$ and $\mathbf{n}_j^{\text{ACC}}$	Angle (deg)
$i = 1, j = 2$	$90.238 \pm 0.032$
$i = 2, j = 3$	$90.053 \pm 0.049$
$i = 3, j = 1$	$89.872 \pm 0.051$

Since the signals of the acceleration sensor are fitted with a sine signal, the angle between two components can be determined more precisely than the angle resolution of  $0.5^\circ$ . The identified angles between the components of the acceleration sensor can be found in tab. 3.2. The deviation of the ADXL330 from perfect orthogonality is very small and at most

### 3. Calibration of particle velocity sensors

0.238°.

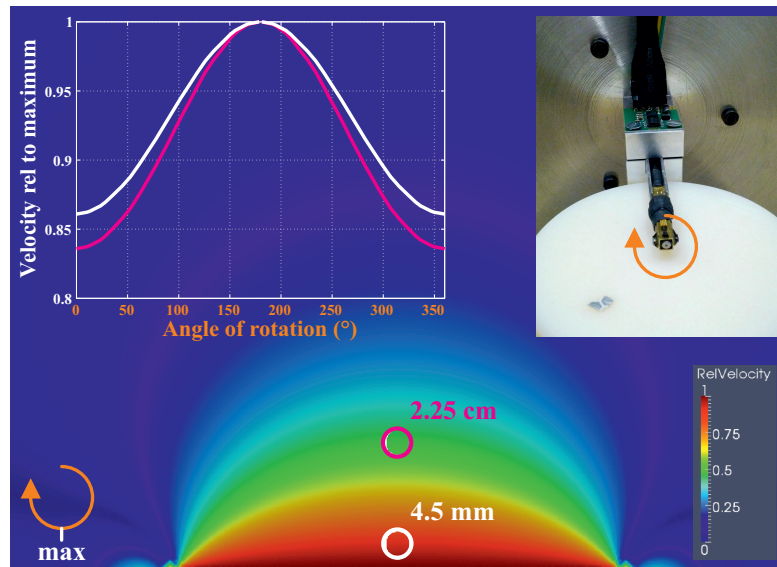


Figure 3.12.: Distribution of the acoustic particle velocity's amplitude 4.5 mm and 2.25 cm in front of the moving piston with with radius 40 mm at 500 Hz. The plot shows the velocity relative to the maximum at 180°.

**3D particle velocity sensor** The implementation of the analysis of the orientation of the sensor's component does not perfectly turn around the axis of each component. For

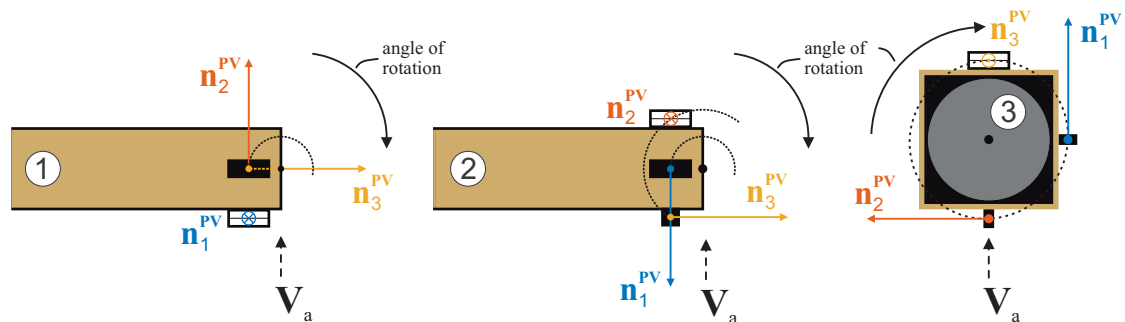


Figure 3.13.: Scenario 1–3 to find out the angles between component 2 and 3 (scenario 1), 3 and 1 (scenario 2) and 1 and 2 (scenario 3).

the analysis of the orientation of the particle velocity sensor a sound field above the moving piston excited with 500 Hz is used. The reference field is not homogeneous and additionally, the components cannot be turned around a point since the components of the particle velocity sensor are not located at the same position. This makes the orientation analysis of the particle velocity sensor more complicated than the analysis in

### 3. Calibration of particle velocity sensors

case of the acceleration sensor, since the amplitude as a function of the rotation angle is not a sine signal or an absolute value of a sine signal. In fig. 3.12 the velocity distribution in case of the amplitude of the relative velocity in front of the moving piston with radius 40 mm at 500 Hz is shown. It can be seen that the reference sound field near the moving piston is flat and it gets more and more spherical with growing distance to the surface of the piston. Furthermore, the amplitude of the relative velocity as a function of the rotation angle at a circle with center 4.5 mm and 2.25 cm above the center of the moving piston is shown. Since a single component of the particle velocity sensor will move on a circle, when the measurement system depicted in fig. 3.12 is turned in the reference sound field, the relative velocity on this circle is of interest. The more the distance to the surface of the moving piston, the more inhomogeneous is the reference sound field, which can be seen in fig. 3.12, where the amplitude of the relative velocity as a function of rotation angle is more constant for the circle being nearer to the surface. The analysis of the spatial orientation of the particle velocity sensor is performed as near as possible to the surface of the moving piston at a distance of 4.5 mm above the center. In fig. 3.13 a sketch of the three measurement scenarios is shown. In scenario 1 the components 2 and 3 move on a circle with the same radius but in different layers (component 3 moves on a circle behind 2). If the particle velocity sensor is placed above the center of the moving piston the velocity on component 2 and 3 is the same, because of the reference field's symmetry. There are two distinctive positions along the rotation process. The signal of component 2 is minimum, when component 3 is maximum and vice versa. To analyze the orientation of both components to each other, the signal's minimum of one component has to be compared with the signal's maximum of the other component. The angle between the distinctive positions is  $0^\circ$  if both components are orientated orthogonal to each other. In scenario 2, the components move on circles with different radius in different layers (component 3 moves on a circle on a layer behind component 1) of the reference field, so there is no distinctive position, where the same acoustic particle velocity acts on the components. The nearest combination of two distinctive positions is the signal's minimum of component 1 and the signal's maximum of component 3. The desired angle between the remarkable positions is  $0^\circ$ . Since component 1 and 2 move on the same circle in scenario 3, the angle, where both signals are minimum can be compared. In theory, the angle difference should be  $90^\circ$ . In the inhomogeneous reference field in fig. 3.12, a component of the sensor moves on a circle as can be seen in the figure. Moreover, in the plot, the velocity on the circle, on which the component 1 and 2 are moving when the particle velocity sensor is turned around component 3, can be seen. Hence, the amplitude of the sensor's signal is not a perfect absolute value of a sine signal, but weighted with a function similar to the one shown in fig. 3.12. In case of the rotation around the axis of component 3, there are no limitations, but the rotation around both other axes are limited to  $\approx 195^\circ$ . The start- and end-scenario of the rotation around these axes can be seen in fig. 3.14. There is no possibility to enlarge this limit, because of the sensor's dimension. As mentioned before, it has to be evaluated either the signal's minimum or maximum. The orientation analysis is performed with an angle resolution of  $0.5^\circ$ . To be able to find out the signals' minimum and not being restricted to the angle resolution of the measurement, the signal is locally interpolated with cubic splines. The

### 3. Calibration of particle velocity sensors

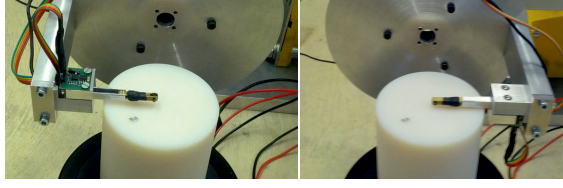


Figure 3.14.: Left: start-scenario. Right: end-scenario, when the USP and the ADXL330 are turned around the axes of component 2 and 3.

interpolation is performed only at a certain range of angles around the minimum of the signal. A signal's maximum can be found in between two signal's minima. Therefore, in a first step, both signal minima are identified in the approach described above. The signal between the two minima is now fitted with a polynomial function to estimate the angle, where the acoustic particle velocity is a maximum. The identified angles between the components of the USP are listed in tab. 3.3. The deviation from  $90^\circ$  is determined to be at the maximum  $1.107^\circ$ . It can be observed that the variance is larger, the greater the deviation is. In case of the determination of the angle between components 1 and 2 the conditions in the measurement setup are the best, since the components distinctive positions can be evaluated at exactly the same position. The analysis here gives the smallest deviation from orthogonality of both components with the smallest deviation in the ten measurements. However, the orthogonality of the USP is nearly given.

Table 3.3.: Angles between the components of the USP.

Angles between $\mathbf{n}_i^{\text{PV}}$ and $\mathbf{n}_j^{\text{PV}}$	Angle (deg)
$i = 1, j = 2$	$90.271 \pm 0.037$
$i = 2, j = 3$	$89.391 \pm 0.080$
$i = 3, j = 1$	$88.893 \pm 0.117$

**Spatial orientation between both sensors** The angles between the equally oriented assumed components, thus component 1 of the acceleration sensor and component 1 of the particle velocity sensor and also of components 2 and 3, are listed in tab. 3.4. The orientation indeed is nearly equally. The largest deviation can be found between the components 3 with an angle of  $1.2^\circ$ . Nevertheless, the deviation from an equally orientation are small and therefore negligible during the calibration process.

Table 3.4.: Angles between the equally orientated components of both sensors.

Angles between $\mathbf{n}_i^{\text{PV}}$ and $\mathbf{n}_i^{\text{ACC}}$	Angle (deg)
$i = 1$	$0.7921 \pm 0.067$
$i = 2$	$0.701 \pm 0.031$
$i = 3$	$1.207 \pm 0.076$

### 3.2. Calibration results

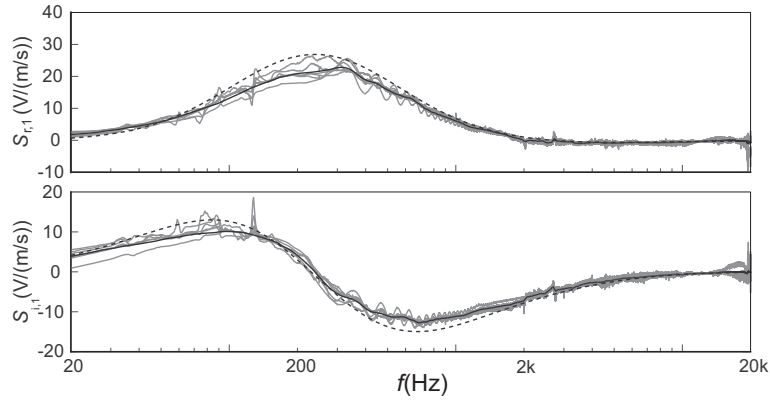


Figure 3.15.: Sensitivity of component 1. The averaged sensitivity of the ten calibration measurements obtained with the six measurement setups is shown as grey line, the overall averaged sensitivity in black and the nominal sensitivity curve (manufacturer) as a dashed line.

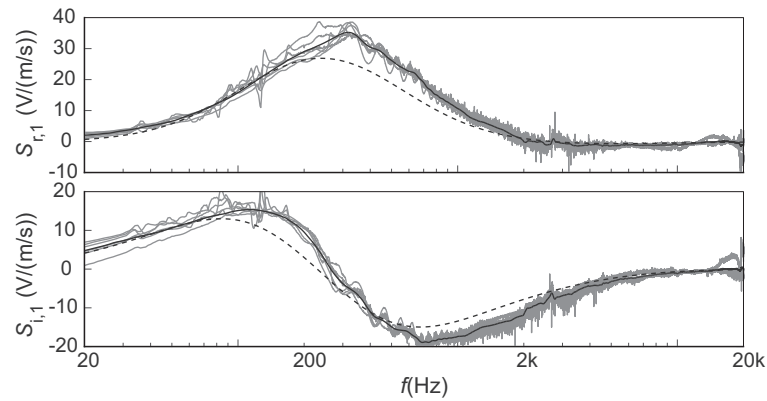


Figure 3.16.: Sensitivity of component 2. The averaged sensitivity of the ten calibration measurements obtained with the six measurement setups is shown as grey line, the overall averaged sensitivity in black and the nominal sensitivity curve (manufacturer) as a dashed line.

The calibration was done by exciting the shaker with a 1 s linear increasing sine-sweep between 20 Hz and 20 kHz. Furthermore, the pistons with three different radii made of aluminum and PLA-50 are used. In total, there are six different measurement setups for the calibration process available. The calibration was done ten times with each calibration setup, whereas the sensitivities of each measurement setup were linear averaged. In fig. 3.15 to 3.17 the calibration results in form of the sensor component's sensitivities (real and imaginary part) obtained by the simultaneous calibration method

### 3. Calibration of particle velocity sensors

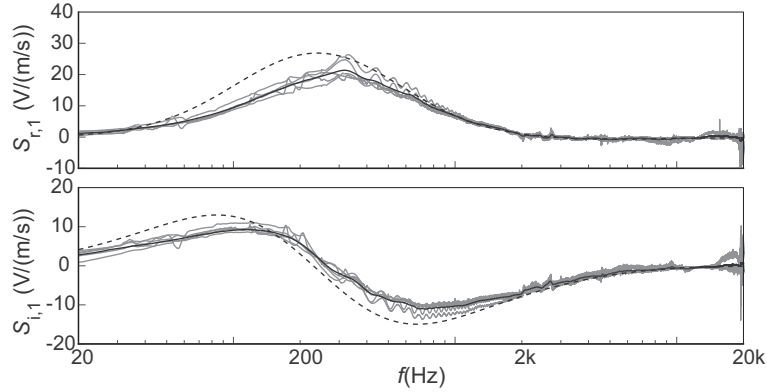


Figure 3.17.: Sensitivity of component 3. The averaged sensitivity of the ten calibration measurements obtained with the six measurement setups is shown as grey line, the overall averaged sensitivity in black and the nominal sensitivity curve (manufacturer) as a dashed line.

are shown. The averaged sensitivities can be seen as grey lines and the overall average of all six calibration setups are displayed as black curve. Moreover, the sensitivities of the particle velocity sensor given by the manufacturer in form of the sensitivity model can be seen as a dashed line. It can be stated that the obtained sensitivities differ from the ones given by the manufacturer in all components at frequencies below 2 kHz. At higher frequencies the sensitivities show good agreement to the sensitivities provided by the manufacturer. The particle velocity sensor can be a useful sensor in the mid frequency domain since the sensor shows an appropriate sensitivity between 100 Hz and 2 kHz. Below 100 Hz and above 2 kHz the sensitivity is very poor because of the reasons explained at the beginning of this chapter. In the sensitivity's real part of component 1 and 3, there can be seen that the sensitivity obtained by the simultaneous calibration method is lower than the nominal sensitivity curves in the mid frequency range. In contrast, the obtained sensitivity's real part of component 2 is found to be higher than the sensitivity given by the manufacturer. However, the calibration method produces reliable sensitivities for each component in a wide frequency range even up to 16 kHz. There are major deviations between each sensitivities found with the six measurement setups at frequencies above 16 kHz since the excitation amplitude and the sensitivity of each component gets very low and hence, the SNR of the calibration is very poor. Of course, there can be errors in placing the particle velocity sensor in the reference sound field. Since the three components of the sensor are not located at the same position, the position of each component is slightly outside the center of the vibrating piston. Particularly at high frequencies, those location errors can have an effect on the calibration result.

### 3.3. Validation of the calibration method

For validation purposes, a known acoustic particle velocity field is required, where the measured acoustic particle velocities on the one hand calculated with the sensitivities given by the manufacturer and on the other hand calculated by means of the sensitivities found out with the simultaneous approach can be compared to a reference acoustic particle velocity computed by means of a FE simulation. Furthermore, it seems to be reasonable, to validate the calibration in a frequency range, where the sensitivity is high, thus in the range between 100 Hz and 2 kHz. In the following, the acoustic particle velocity field in front of a moving plate is investigated.

#### 3.3.1. Measurement setup for validation measurements

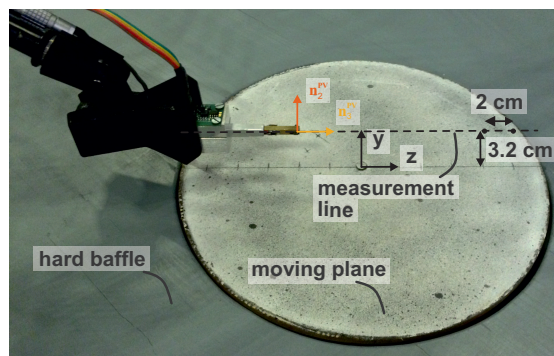


Figure 3.18.: Measurement setup for validation measurements.

The plate is made of acrylic glass with diameter 23.5 cm and thickness 4.7 mm. It is excited with an electrodynamic vibration exciter in the center. In fig. 3.18 the measurement setup for the validation of the calibration approach is shown. Thereby, the acoustic particle velocity is measured at 13 points (distance between each measurement point: 2 cm) on a measurement line 3.2 cm in front of the moving plate. The plate shows a mechanical bending mode at a frequency range around 300 Hz. The simulated and measured magnitude of the mechanical impedance (ratio of force and velocity) is shown in fig. 3.19. In the simulation, the mechanical properties of the plate have been tuned to fit the mechanical impedance at the excitation point in the center of the moving plate, whereas the properties were chosen that the impedance fits best at the two validation frequencies 300 Hz being in the resonance and 400 Hz above the first resonance frequency. In the following, the acoustic particle velocity in  $y$ - and  $z$ -direction is investigated and the  $x$ -component is omitted because this amplitude is very small. The acoustic particle velocity measured with component 2 is the out of plane and measured with component 3 is the in plane acoustic particle velocity.



### 3. Calibration of particle velocity sensors

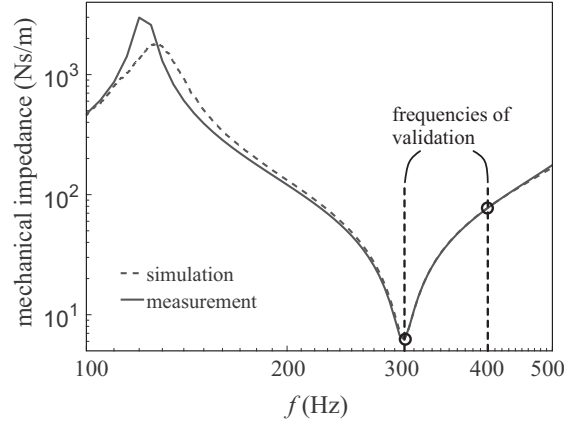


Figure 3.19.: Measured and simulated magnitude of the mechanical impedance on the excitation in the center of the moving acrylic plate.

#### 3.3.2. Acoustic particle velocity measurements above a vibrating plane

In fig. 3.20 the comparison of the measured and simulated acoustic particle velocity at 300 Hz nearby the first resonance and in fig. 3.21 those for 400 Hz is displayed. The acoustic particle velocities computed with the sensitivities determined by the simultaneous calibration method described in the previous section is shown as grey solid line. The mean value of these lines can be seen as black solid line. In comparison, the acoustic particle velocities calculated with the manufacturer sensitivities are displayed as dashed line, whereas the acoustic particle velocity calculated with the FE simulation is shown as reference in red. As expected, the acoustic particle velocities at 300 Hz nearby the eigen frequency are much higher than the ones at 400 Hz. Moreover, acoustic particle velocity out of plane (component 2) can be determined to be higher at 300 Hz than the acoustic particle velocity in plane (component 3). Near the resonance, the real part and at 400 Hz the imaginary part is dominant. However, the acoustic particle velocities computed with the sensitivities of the simultaneous calibration show better agreement to the simulated data compared to the acoustic particle velocities computed with the manufacturers sensitivities. Moreover, the determined acoustic particle velocity fits better, the higher the quantity is, since the SNR is assumed to be better and therefore, the measurement gives better results. The comparison of the sensitivities found out by means of the simultaneous calibration method and the manufacturer calibration data show that there is a significant difference between both in the mid frequency range. Taking into account that the particle velocity sensor is used to characterize absorbers for low frequencies this difference can make a great disparity in the determined properties.

### 3. Calibration of particle velocity sensors

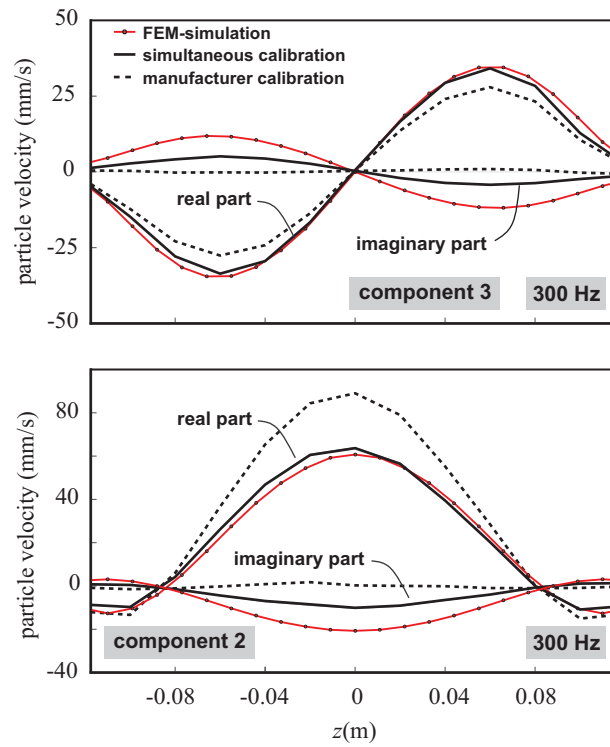


Figure 3.20.: Acoustic particle velocity at 300 Hz on the measurement line 3.2 cm in front of the moving plate. Measurement results using the sensitivities in comparison to the acoustic particle velocity data obtained by a FE simulation of the sound field.

### 3. Calibration of particle velocity sensors

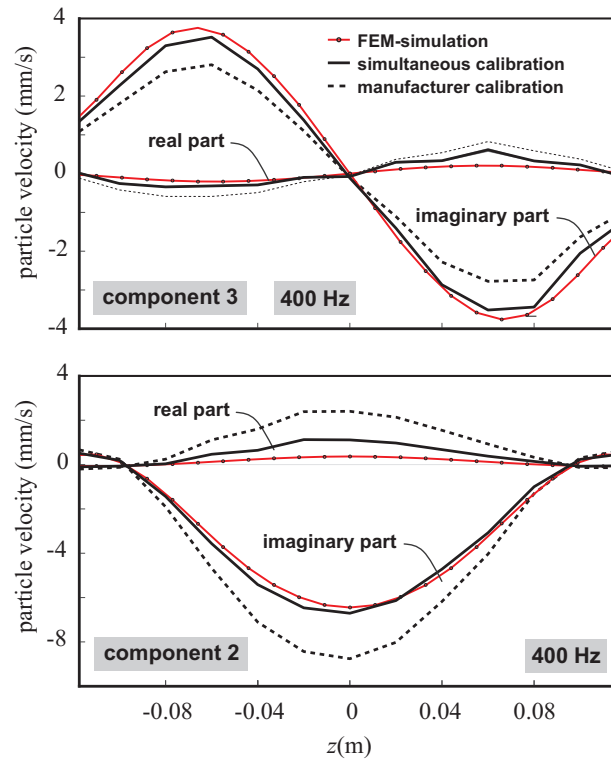


Figure 3.21.: Acoustic particle velocity at 400 Hz on the measurement line 3.2 cm in front of the moving plate. Measurement results using the sensitivities in comparison to the acoustic particle velocity data obtained by a FE simulation of the sound field.

## 4. Characterization of absorbers for high frequencies

In this chapter the characterization of materials absorbing acoustic energy at high frequencies is presented. For the two characterization methods used in this thesis only a single pressure microphone is used to determine the acoustic surface properties at an interface between the absorber and the surrounding air. The theory of the two methods is described in detail, the characterization of the implemented methods is shown and improvements on the implementation are reviewed. Measurement results at oblique angles of sound incidence in comparison to the theoretical values obtained by the models presented in Sec. 2.3.4 are discussed. Furthermore, the measurement results obtained at perpendicular sound incidence are compared with acoustic properties measured with the impedance tube following ISO 10534-2 [4].

### 4.1. Characterization of acoustic surface properties

In this section, two methods are presented to determine the acoustic properties on an interface by means of a single microphone and a sound source. The first method is a subtraction method in time domain, by which the properties can be calculated by means of a separation of an incoming and a reflecting impulse. The second method is based on a spatial Fourier transform. Here, the acoustic properties are calculated by a decomposition of a sound field into plane waves on several measurement planes.

#### 4.1.1. Subtraction method (Time domain)

The basic idea for the measurement of acoustic surface properties at an interface by means of a separation of an incoming and reflecting impulse can be found in [93] and [134]. This is the most common approach to separate direct and reflected sound to obtain reflection coefficients [34]. An application of the subtraction method can be found in [107] using a single microphone to record acoustic pressure data on two spheres. A further application of the subtraction method in combination with a microphone array can be found in [91], where the acoustic pressure is measured with 24 microphones arranged in two rotatable half circles providing measurement points at two hemispheres in order to measure the surface reflection properties for many angles of sound incidence with only using a single source position [92]. In [73] the performance of the subtraction technique using acoustic particle velocity measurements is investigated. It is shown to be more robust regarding disturbing reflections than the method using the acoustic pressure. The

#### 4. Characterization of absorbers for high frequencies

implementation of the subtraction method used in this thesis was developed during the work for a bachelor thesis [118] and is reported in [84].

##### Theory of the subtraction method

In fig. 4.1 the schematic of the subtraction method is shown. A loudspeaker is positioned at a certain distance  $h_y$  in front of a sample under consideration. Moreover a microphone is placed at  $r_y$  above the sample. The angle between the loudspeaker and the microphone in respect to the normal of the surface is  $\theta_i$ . Since the acoustic properties of the surface are different to the ones of the surrounding medium, there will be reflection at the interface at the point of reflection (POR). This is taken into account by introducing an image source. The loudspeaker is excited by an input signal  $x_{in}(t)$  and the pressure at a distance of  $r_d$  is recorded by means of a microphone. The measured acoustic pressure above the sample

$$p_m(t) = (x_{in} * h_m)(t) = p_{m,d}(t) + p_{m,r}(t) + p_{m,p}(t) \quad (4.1)$$

is a superposition of the direct  $p_{m,d}$ , reflected  $p_{m,r}$  and parasitic  $p_{m,p}$  components.

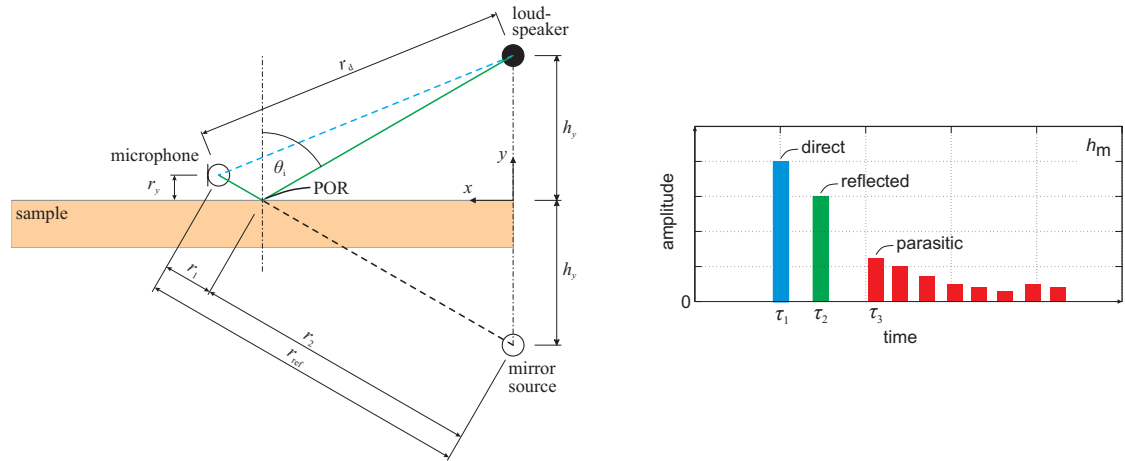


Figure 4.1.: Left: schematic of the measurement system with a sample under test. Right: expected signal of the IR measured with the microphone above the sample.

Removing the sample (see fig. 4.2) and recording the pressure in the same way, the measured pressure in the free field measurement

$$p_{ff}(t) = (x_{in} * h_{ff})(t) = p_{ff,d}(t) + p_{ff,p}(t) \quad (4.2)$$

only shows the direct and parasitic part. The acoustic pressure in (4.1) and (4.2) are a result of a convolution of the input signal and the IRs ( $h_m$  and  $h_{ff}$ , respectively) of

#### 4. Characterization of absorbers for high frequencies

the measurement systems with the sample. The IRs can be calculated using (2.66) and compute to

$$\begin{aligned}
 h_m(t) &= (p_m * x_{in}(\cdot))(t) \\
 &= ((h_{m,d} + h_{m,r} + h_{m,p}) * \delta)(t) \\
 &= C_{m,d}(s * \delta_{-\tau_1})(t) + C_{m,r}(s * h_r * \delta_{-\tau_2})(t) \\
 &\quad + C_{m,p}(s * f_p * \delta_{-\tau_3})(t)
 \end{aligned} \tag{4.3}$$

$$\begin{aligned}
 h_{ff}(t) &= (p_{ff} * x_{in}(\cdot))(t) \\
 &= ((h_{ff,d} + h_{ff,p}) * \delta)(t) \\
 &= C_{ff,d}(s * \delta_{-\tau_1})(t) + C_{ff,p}(s * f_p * \delta_{-\tau_3})(t),
 \end{aligned} \tag{4.4}$$

where  $f_p$  is the parasitic component of the IR,  $s$  is the IR of the measurement system and  $h_r$  the IR of the sample's surface. The coefficients  $C_{m,d}$ ,  $C_{m,r}$ ,  $C_{m,p}$ ,  $C_{ff,d}$  and  $C_{ff,p}$  compensate the amplitude and  $\tau_{1,2,3}$  the time shift of a traveling spherical wave. The IR of each measurement system is a superposition of the direct (d), reflected (r) and parasitic (p) part of the IR, which are excited at different times ( $\tau_1 < \tau_2 < \tau_3$ ). In the right part of fig. 4.1 and 4.2 the IRs can be seen. The direct and parasitic part can be seen in blue and red, whereas the green reflected part only appears in the IR of the measurement system above the sample.

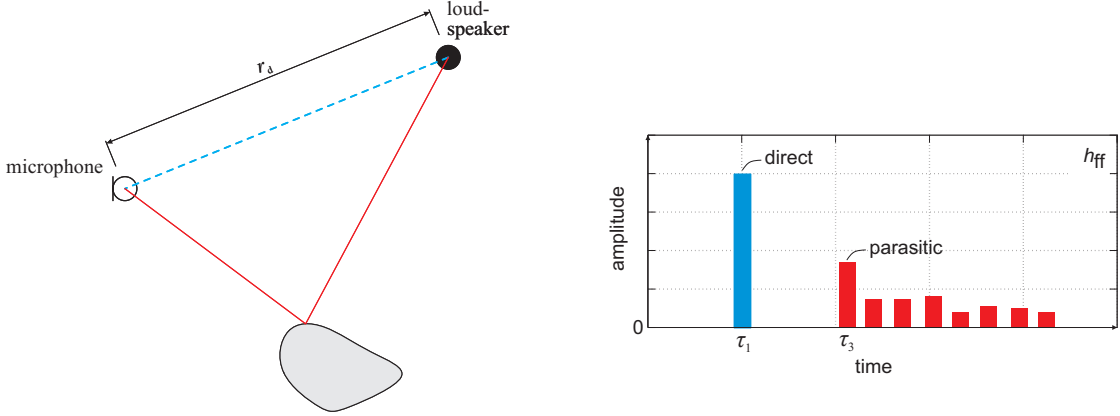


Figure 4.2.: Left: schematic of the measurement system in the free field with an obstacle. Right: expected signal of the IR measured with the microphone above the sample.

The parasitic part in (4.3) and (4.4) can be canceled out using a time window ( $h_{m,p} = h_{ff,p} = 0$ ). With a time window, the IRs can be weighted and damped to be zero at a time beginning with  $\tau_3$ , where only parasitic effects can be found in the IR. The IR of the sample is assumed to be decayed at this time. To separate the reflected impulse response, the time windowed IRs in (4.3) and (4.4) are subtracted in time domain. With the assumption that the direct IRs in both measurements are equal ( $h_{m,d} = h_{ff,d}$ ), the subtraction results in

#### 4. Characterization of absorbers for high frequencies

$$h_{\text{sub}}(t) = (h_m - h_{\text{ff}})(t) = C_{m,r}(s * h_r * \delta_{-\tau_2})(t). \quad (4.5)$$

In fig. 4.3 a sketch of the subtraction process is displayed including the time windows for canceling the parasitic components out of the IRs. Moreover, the influence of varying environmental conditions between the two measurements resulting in a time ( $\Delta\tau$ ) and amplitude ( $\Delta C$ ) shift is illustrated in fig. 4.3. In case of  $\Delta\tau = 0$  and  $\Delta C = 0$ , the subtraction result in (4.5) only consists of the reflected green peak. Since  $h_m$  includes the information of the incoming and reflecting wave, the separation of the reflecting part by a subtraction in (4.5) is not mandatory. It is also possible to only separate the direct and reflected part of  $h_m$  in (4.4) by a time window. This can only be done, if  $\tau_2$  is sufficiently larger than  $\tau_1$  and therefore the direct IR is decayed before the reflected IR starts. In case of a small distance between microphone and sample, a sufficiently large time interval between  $\tau_1$  and  $\tau_2$  is obviously not given.

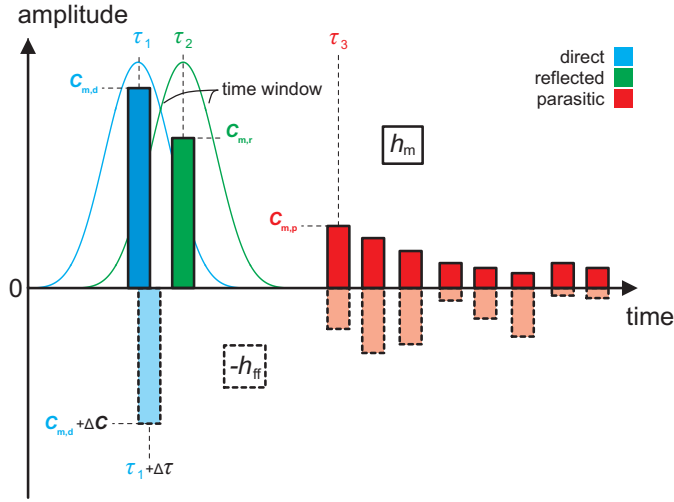


Figure 4.3.: Sketch of the subtraction used in (4.5) including the influence of varying environmental conditions between the two measurements and the time windows for canceling the parasitic components out of the IRs.

In frequency domain, the time windowed IR in (4.4) and (4.5) get the transfer functions and compute to

$$H_{\text{ff}}(\omega) = C_{\text{ff},d}S(\omega)e^{-j\omega\tau_1} \quad (4.6)$$

$$H_{\text{sub}}(\omega) = C_{m,r}S(\omega)R(\omega)e^{-j\omega\tau_2}. \quad (4.7)$$

Dividing (4.7) and (4.6), replacing the coefficients  $C_{\text{ff},d} = 1/r_d$  and  $C_{m,r} = 1/r_{\text{ref}}$  and the time delays  $\tau_1 = r_d/c$  and  $\tau_2 = r_{\text{ref}}/c$ , the sound pressure reflection coefficient computes

#### 4. Characterization of absorbers for high frequencies

to

$$R(\omega) = \frac{H_{\text{sub}}(\omega)}{H_{\text{ff}}(\omega)} \frac{r_{\text{ref}}}{r_{\text{d}}} e^{jk(r_{\text{ref}}-r_{\text{d}})}. \quad (4.8)$$

The distance  $r_{\text{ref}}$  can be computed with

$$r_{\text{ref}} = r_1 + r_2 \quad (4.9)$$

and results at perpendicular sound incidence in

$$r_{\text{ref}}|_{\theta_i=0^\circ} = r_{\text{d}} + 2r_y. \quad (4.10)$$

#### Improvements on the subtraction method

Since both IRs are not measured at the same time, the direct components of the IRs in the free field and above the sample can differ. This is taken into account by introducing a time delay  $\Delta\tau$  and an amplitude shift  $\Delta C$  in fig. 4.3. To quantify the effectiveness of the subtraction result, the reduction factor proposed in [109]

$$RF = 10 \log \left( \frac{\int_{\tau_1-\Delta t}^{\tau_1+\Delta t} h_{\text{ff}}^2 dt}{\int_{\tau_1-\Delta t}^{\tau_1+\Delta t} h_{\text{sub}}^2 dt} \right) \quad (4.11)$$

is used. In (4.11), the square of the impulse responses (and thus the sound energy) in case of the free field measurement and the subtraction result from  $\Delta t$  before and  $\Delta t$  after the time of the direct peak  $\tau_1$  are compared. In case of a perfect subtraction, the subtracted IR  $h_{\text{sub}}$  is zero and  $RF \rightarrow \infty$ . The signal, that is remaining in case of an incomplete subtraction can cause massive errors in the determination of the acoustic surface properties. Especially at high frequencies comb filter effects can occur [87].

**Time-windowing** For canceling out the parasitic part of the IRs  $h_{\text{sub}}$  and  $h_{\text{ff}}$  a time window is used. In [5] an Adrienne window is proposed. However, the Blackmann–Harris window is a symmetric time window and its peak is placed at the peak of the IR as can be seen in the right part of fig. 4.4. Furthermore, the Adrienne time window consists of a Blackmann–Harris time window on the left and on the right side (in the shown example the left part increases faster than the right part decreases, which means that on the left side an other Blackmann–Harris window is used than on the right side) and in between the window is of a constant value 1. The curve of the obtained sound absorption coefficient is shown in the left part of fig. 4.4. The curve determined with the Blackmann–Harris window seems to be more smooth, even though the frequency resolution using the Adrienne window is coarser. The most important information of



#### 4. Characterization of absorbers for high frequencies

the sample's IR is located in the peak of the IR and there are more and more disturbances like reflections at the time after this peak. Hence, in the following, all calculations are done using the Blackmann–Harris time window.

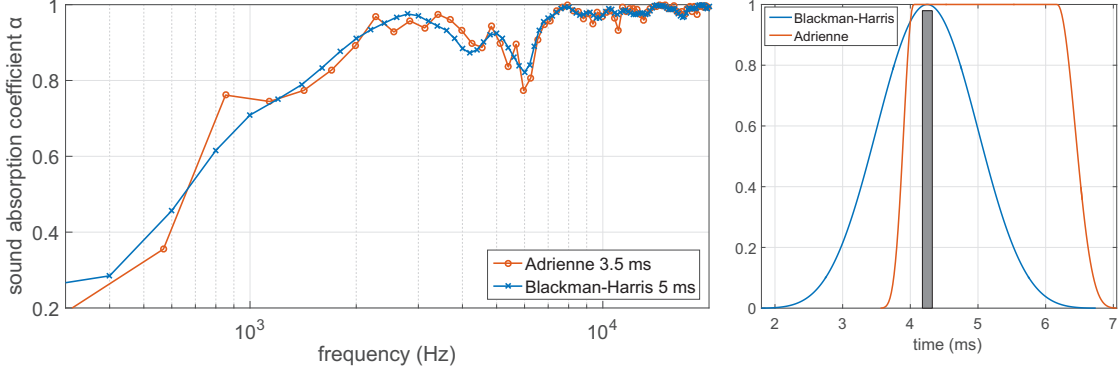


Figure 4.4.: Left: sound absorption coefficient of a 40 mm rock wool sample at perpendicular sound incidence using a Blackmann–Harris and an Adrienne time window. Right: Both windows along an impulse at 4.2 ms.

The length of the time window plays an important role in the subtraction method, since it influences the frequency resolution of the acoustic properties and additionally it has an effect on the quality of the measurement result. The length has to be chosen long enough to capture the whole IR of the material and has to be chosen short enough to cancel out the reflection caused by obstacles. The first obstacle beside the measurement setup is the edge of the sample, which has to be taken into account. The derivation of the geometric aspects can be found in [118]. The IR component carrying the information of the edge reflection will appear and therefore the maximum length of the time window at sound incidence of  $\theta_i$  is

$$t_{\text{win,max}} = \frac{1}{c} \sqrt{(r_1 \sin \theta_i + r_{e,\text{min}})^2 + (r_1 \cos \theta_i)^2} + \frac{1}{c} \sqrt{h_y^2 + \left( r_{e,\text{min}} - r_d \sin \left( \sin^{-1} \left( \frac{r_1}{r_d} \sin 2\theta_i \right) + \theta_i \right) + r_1 \sin \theta_i \right)^2}. \quad (4.12)$$

In (4.12)  $r_{e,\text{min}}$  is the distance from the POR (see fig. 4.1) to the nearest edge of the sample.

**Oversampling and time shifting** Due to a change of the environmental conditions, e.g. temperature, the speed of sound at the measurements can change, which results in a time shift  $\Delta\tau$  of the direct component (see fig. 4.3). Furthermore, an inaccurate determination of the source and receiver position and phase calibration errors can lead to a time shift of the direct component. To compensate these time shift, the free field measurement can be shifted in time by  $-\Delta\tau$ . Since the signal exist as time discrete

#### 4. Characterization of absorbers for high frequencies

values, one is limited to the sample time (inverse value of the sample rate  $f_s$ ) as the smallest value for a time shifting process. If  $\Delta\tau$  is smaller than the sample time, the time delay cannot be compensated. In [109] an oversampling by an oversampling factor  $n_{ov}$  of the IR is proposed to be able to shift the IR in time in a better way. In this paper, the oversampling factor is increased iteratively. In this thesis, the acoustic pressure is recorded with a sample rate  $n_{ov}$  times higher than the required one to increase the reduction factor. In this oversampling optimization, a set of  $n_{ov}$  IRs is available to apply (4.5), whereas the best result in respect to (4.11) is used.

**Phase shifting in frequency domain** Another possibility to shift the IRs in time by a delay  $n_{max}$  times smaller than the sample rate is proposed in [5]. The shifting delay can be computed in time domain with

$$\Delta T = \frac{1}{n_{max}f_s}. \quad (4.13)$$

The IR is transformed into the frequency domain ( $h_{ff}(t) \rightarrow H_{ff}(\omega)$ ) and a phase shift on the signal is applied. The new IR of the free field measurement computes by

$$H'_{n,ff}(\omega) = H_{ff}(\omega)e^{-j2\pi f \frac{n}{n_{max}f_s}}. \quad (4.14)$$

By using (4.14) and  $n = 1 \dots n_{max}$ ,  $n_{max}$  phase shifted transfer functions can be generated. Transforming back into time domain, the phase shift results in a time shift and the subtraction can be performed  $n_{max}$  times, whereas the best result regarding the reduction factor can be used for calculations.

**Combined optimization** In this thesis a combination of the oversampling in time domain and a phase shifting in frequency domain is used. Furthermore, the amplitudes of both IRs before subtracting are adjusted that the peaks of both IRs are equal. This covers the problem of an amplitude shift  $\Delta C$  as displayed in fig. 4.3. The pressure signal is sampled with an oversampling factor of 20, which means that there are ten sets of IR available, which can be combined. Furthermore, an additional phase shifting with  $n_{max} = 50$  is applied to reach a better reduction factor.

In the left part of fig. 4.5 the result of the subtraction using (4.5) can be seen for different optimized subtraction techniques. The IRs' amplitude are normalized to the peak of  $h_{ff}$ . Thereby,  $h_{sub,4}$ ,  $h_{sub,5}$  and  $h_{sub,6}$ , which do not differ much, show small values in comparison to the other curves and are displayed in a zoomed plot in the right part of the figure. The IRs to be subtracted are shown in black and for evaluating the reduction factor with (4.11)  $\Delta t$  of 0.3 ms is used. Here,  $h_{sub,1}$  is the subtraction result without using any optimization of the subtraction and results in a reduction factor of 10.73 dB. It can be seen that the peak of  $h_{ff}$  is higher than the one of  $h_m$ . Therefore a subtraction with an amplitude adjusted  $h_{ff}$  is done. This subtraction result can be seen as  $h_{sub,2}$  and gives a slightly smaller reduction factor of 10.37 dB. In the amplitude

#### 4. Characterization of absorbers for high frequencies

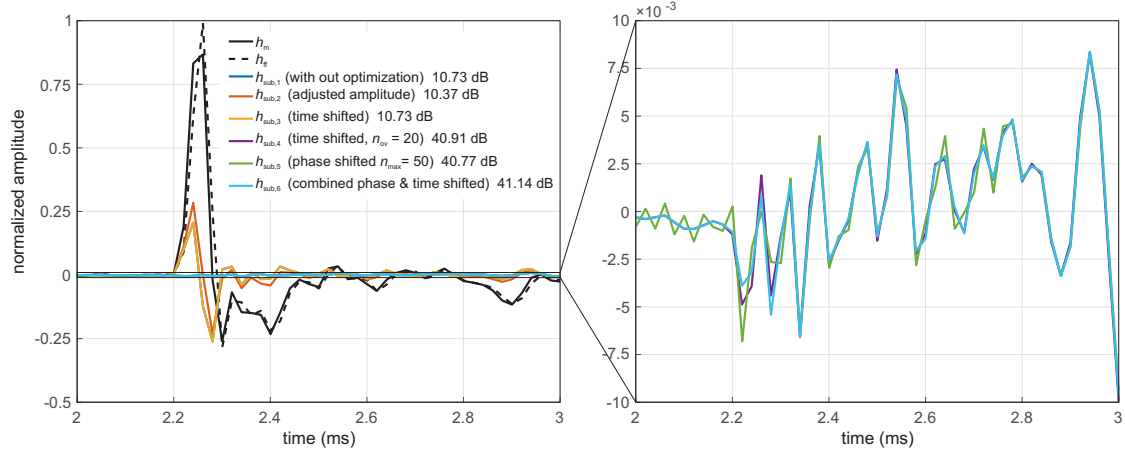


Figure 4.5.: The measured IRs and subtraction results using optimized subtraction technique.

adjustment only the peak of each IR is adjusted. If the peaks of the direct component occurs at different times, e.g. due to environmental influences, the amplitude adjustment can cause a worse subtraction result in terms of a smaller reduction factor. Furthermore,  $h_{sub,3}$  can be seen as the subtraction result after time-shifting  $h_{ff}$ , which doesn't make a difference here and results in the same reduction factor as  $h_{sub,1}$ , since no time shift of  $h_{ff}$  gives better results than the original subtraction. As can be seen in the plot, the subtraction result still leaves artifacts. This artifacts can be canceled, by using a time shift with an  $n_{ov}$  of 20 or a phase shift with  $n_{max}$  of 50. The subtraction results using both shift methods can be seen as  $h_{sub,4}$  and  $h_{sub,5}$ , whereas the reduction factor with both methods increases to 40.91 dB and 40.77 dB respectively. Combining both methods, applying an oversampling with  $n_{ov}$  of 20 and additionally a phase shifting with  $n_{max}$  of 50, the reduction factor can be further increased to 41.14 dB. The subtraction result is shown as  $h_{sub,6}$ . In tab. 4.1 the evaluated reduction factors by using the optimization techniques described above can be seen. The combined phase and time shift method seems to be the best regarding the reduction factor, but is of course the one with the most effort.

Table 4.1.: Reduction factor of the subtraction using optimized subtraction technique

Method	reduction factor (dB)
simple subtraction	10.73
adjusted amplitude	10.37
time shifted	10.73
time shifted + oversampling in time domain( $n_{ov} = 20$ )	40.91
phase shifted in frequency domain( $n_{max} = 50$ )	40.77
combined phase & time shift	41.14

### Implementation of the subtraction method

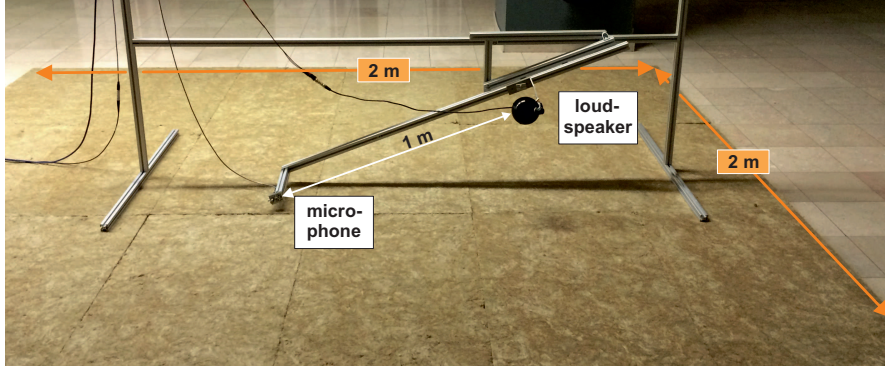


Figure 4.6.: Typical measurement setup in a stairwell at the TU Wien with a loudspeaker and microphone above a 4 m<sup>2</sup> rock wool sample.

The measurement setup for the subtraction method can be seen in fig. 4.6. The distance  $r_d$  between loudspeaker and microphone is chosen to be 1 m and the microphone is placed at  $r_y = 0.15$  m. Therefore, in case of perpendicular sound incidence, the direct and reflected peak in  $h_m$  will be at  $\tau_1 \approx 2.92$  ms and  $\tau_2 \approx 3.79$  ms. The distances are a trade-off between the time, the IR of the sample  $h_r$  can be evaluated before the first reflections are in  $h_{\text{sub}}$  (the evaluation time is between  $\tau_2$  and  $\tau_3$ ) and the fact that there is no overlapping of the direct and reflected part in this evaluated time slot. The measurements using the subtraction method are performed in a normal room with hard walls in distance of more than 2 m away from the measurement setup, so the first reflections in  $h_m$  caused by the walls will be expected at  $\tau_3 \approx 11.66$  ms. Hence, the measurements are performed without any special anechoic conditions. The acoustic pressure is recorded approximately 20 s with 500,000 samples/s and a MLS with length  $2^{20} + 1$  is used for excitation. The loudspeaker used for the measurements is mounted in a spherical enclosure to avoid diffraction at any edges of the boxing. The directivity of the loudspeaker is not taken into account and is assumed to be of spherical nature. This can cause measurement errors especially at higher frequencies, where the directional characteristic of the loudspeaker develops. Furthermore, the distance between microphone and loudspeaker is not calibrated, which also maybe induce deviations at higher frequencies.

#### 4.1.2. Spatial Fourier transform method (Wavenumber domain)

The idea, to obtain the acoustic surface properties at an interface by means of a spatial Fourier transform can be found in [43]. Here, the theory for measuring the sound pressure reflection coefficient at oblique angles of sound incidence is presented. Numerical investigations showed that the error due to the spatial sampling of the acoustic pressure field can be reduced by using a dipole sound source instead of a monopole [115]. The experimental verifications of the method using a single mobile microphone, to obtain the acoustic pressure at 200 measurement points along 1 m, presented in [116] show good

#### 4. Characterization of absorbers for high frequencies

agreement with the theoretical values. Several implementations of this method can be found [26] [133]. In [101] a linear microphone array with 28 microphones arranged in a total length of 1.08 m is used to speed up the measurement time. With this measurement setup the reflection coefficients can be retrieved up to an sound incidence angle of  $45^\circ$ . This setup was improved and presented in [100]. Here, 32 microphones are used and an edge diffraction correction is included in the post processing. In [103] a finite surface method, based on the spatial Fourier transform method, to improve the measurement results of small samples and large angles of sound incidence is presented. In [22] and [74] the performance of the method using particle velocity instead of the acoustic pressure is investigated. The usage of the particle velocity is more beneficial the larger the flow resistivity of the material under test and the higher the frequency is. The implementation of the spatial Fourier transform method used in this thesis was developed in a master thesis [119].

#### Theory of the spatial Fourier transform method

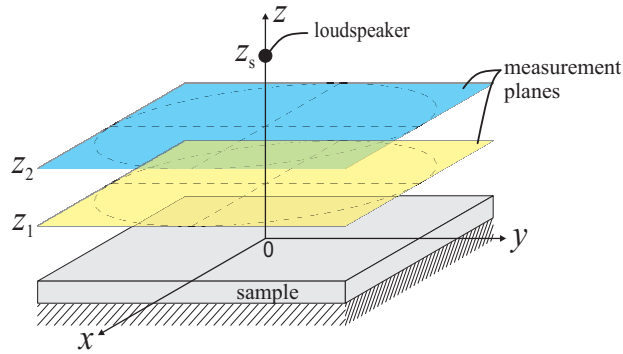


Figure 4.7.: Schematic of the measurement system for the spatial Fourier transform method with a loudspeaker at height  $z_s$  and two measurement planes  $z_1$  and  $z_2$ .

In fig. 4.7 the schematic of the spatial Fourier transform method is shown. A loudspeaker is positioned at a certain distance  $z_s$  in front of a sample. The pressure distribution on a plane in wave number domain using (2.44) computes to

$$\tilde{P}_a(k_x, k_y) = \int_{-\infty}^{\infty} \int_{-\infty}^{\infty} P_a(x, y) e^{-j(k_x x + k_y y)} dx dy. \quad (4.15)$$

In (4.15)  $P_a(x, y)$  is the time Fourier transformed pressure distribution on the plane and  $k_x$  and  $k_y$  are the components of the wave vector

$$\mathbf{k} = \begin{pmatrix} k_x \\ k_y \end{pmatrix} \quad (4.16)$$

#### 4. Characterization of absorbers for high frequencies

with  $k$ , the wave number in the propagation medium. The inverse Fourier transform

$$P_a(x, y) = \frac{1}{2\pi} \int_{-\infty}^{\infty} \int_{-\infty}^{\infty} \tilde{P}_a(k_x, k_y) e^{j(k_x x + k_y y)} dk_x dk_y \quad (4.17)$$

can be interpreted in such way that the pressure distribution on a plane can be represented by a sum of an infinite number of harmonic components. Any kind of wave can be decomposed into plane wave components by using the spatial Fourier transform [77]. In the following, we assume a spatial distribution on a  $xy$ -plane. We assume the sample to be homogeneous, which means the acoustic surface properties do not change with the coordinates  $x$  and  $y$  (non-locally reacting). In the planes under consideration, the acoustic pressure only is nonzero if  $x_{\min} \leq x \leq x_{\max}$  and  $y_{\min} \leq y \leq y_{\max}$ , so that (4.15) gets

$$\tilde{P}(k_x, k_y) = \int_{y_{\min}}^{y_{\max}} \int_{x_{\min}}^{x_{\max}} P e^{-j(k_x x + k_y y)} dx dy. \quad (4.18)$$

For a better readability, the dependency of the variables in the brackets and the subscript  $a$  for acoustic quantities is omitted partially. However, since the spatial distribution on the two measurement plane is a superposition of an incoming and a reflected wave, the spatial Fourier transform of the acoustic pressure on these planes can be decomposed

$$\tilde{P}(z_{1/2}) = \tilde{P}_i(z_{1/2}) + \tilde{P}_r(z_{1/2}) \quad (4.19)$$

into an incoming  $\tilde{P}_i(z_{1/2})$  and reflected part  $\tilde{P}_r(z_{1/2})$ . The same decomposition can be done with the spatial Fourier transform of the acoustic pressure at the interface between sample and surrounding air

$$\tilde{P}(0) = \tilde{P}_i(0) + \tilde{R}\tilde{P}_i(0) \quad (4.20)$$

with  $\tilde{R}$ , the spatial transform of the acoustic pressure reflection factor defined in (2.37). The incident and reflected component in (4.19) can be replaced as follows

$$\tilde{P}_i(z_{1/2}) = \tilde{P}_i(0) e^{jk_z z_{1/2}} \quad (4.21)$$

$$\tilde{P}_r(z_{1/2}) = \tilde{R}\tilde{P}_i(0) e^{-jk_z z_{1/2}}. \quad (4.22)$$

Hence, the spatial Fourier transform of the acoustic pressure on the two measurement planes computes to

$$\tilde{P}(z_{1/2}) = \tilde{P}_i(0) e^{jk_z z_{1/2}} + \tilde{R}\tilde{P}_i(0) e^{-jk_z z_{1/2}}. \quad (4.23)$$

#### 4. Characterization of absorbers for high frequencies

Now both equations for  $z = z_1$  and  $z = z_2$  in (4.23) may be written as a system of linear equations

$$\begin{bmatrix} e^{jk_z z_1} & e^{-jk_z z_1} \\ e^{jk_z z_2} & e^{-jk_z z_2} \end{bmatrix} \begin{bmatrix} \tilde{P}_1(0) \\ \tilde{R}\tilde{P}_1(0) \end{bmatrix} = \begin{bmatrix} \tilde{P}(z_1) \\ \tilde{P}(z_2) \end{bmatrix} \quad (4.24)$$

is obtained. Solving (4.24) the sound pressure reflection factor can be determined with

$$\tilde{R}(k_x, k_y) = \frac{\tilde{P}(z_2)e^{jk_z z_1} - \tilde{P}(z_1)e^{jk_z z_2}}{\tilde{P}(z_1)e^{-jk_z z_2} - \tilde{P}(z_2)e^{-jk_z z_1}}. \quad (4.25)$$

If a symmetry in the  $z$ -plane can be assumed it is not necessary to perform a 2D spatial Fourier transform. Instead a 1D transform introduced in (2.45) can be used. In analogy to (4.18), only the Fourier integral in (2.45) up to  $r_{\max}$  has to be computed

$$\tilde{P}(k_r) = 2\pi \int_0^{r_{\max}} P J_0(k_r r) dr, \quad (4.26)$$

if the acoustic pressure for  $r > r_{\max}$  is zero. The wave vector computes by

$$\mathbf{k} = \begin{pmatrix} k_r \\ k_z \end{pmatrix} = \begin{pmatrix} k \sin \theta_i \\ k \cos \theta_i \end{pmatrix}. \quad (4.27)$$

A schematic for such a measurement system can be seen in fig. 4.8. In this case, the measurement of the spatial distribution has to be conducted in two measurement lines. A homogeneous sample with no change of the acoustic properties with the  $r$ -coordinate is assumed.

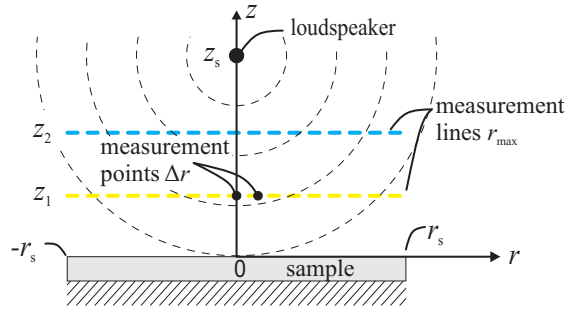


Figure 4.8.: Schematic of the measurement system for the spatial Fourier transform method in 2D.

The sound pressure reflection factor computes by

#### 4. Characterization of absorbers for high frequencies

$$\tilde{R}(k_r) = \frac{\tilde{P}(z_2)e^{j\sqrt{k^2-k_r^2}z_1} - \tilde{P}(z_1)e^{j\sqrt{k^2-k_r^2}z_2}}{\tilde{P}(z_1)e^{-j\sqrt{k^2-k_r^2}z_2} - \tilde{P}(z_2)e^{-j\sqrt{k^2-k_r^2}z_1}}. \quad (4.28)$$

The angle of sound incidence can be calculated by the radial wave number  $k_r = \sqrt{k_x^2 + k_y^2}$  using the relation

$$\theta_i = \arcsin\left(\frac{k_r}{k}\right). \quad (4.29)$$

#### Accuracy of the spatial Fourier transform method

In this section, a modification of measurement parameters is done to investigate the accuracy of the spatial Fourier transform method. Here, the acoustic pressure above an interface at  $z = 0$  is calculated using (2.54) and (2.59). The sound pressure reflection coefficient at the interface is calculated by using (2.36) and (2.37) applying the Komatsu model (see appendix A.1) to describe the sound absorbing material with  $\sigma = 9.5$  kPa and  $d = 41$  mm backed by a rigid baffle. Calculating the acoustic pressure field above an interface excited with a monopole (2.54) and a dipole (2.59) an integral has to be solved with the upper integration limit for  $k_r$  towards infinity. In general, the reflection coefficient is calculated and measured for real angles of sound incidence up to  $90^\circ$ , which corresponds to  $k_r = k$ . In case of a further integration towards infinity, the angle of sound incidence gets a complex number

$$\theta_i = \pi/2 - j\kappa, \quad (4.30)$$

with the imaginary part of the angle  $\kappa > 0$  [43]. The relation with  $k_r$  computes to

$$\kappa = \cosh^{-1}\left(\frac{k_r}{k}\right). \quad (4.31)$$

There can be found a condition for geometries of the setup in literature [43], where the integration up to  $k_r = k$  is sufficient. However, most modern numerical integration routines have an approximation for limits towards infinity, so the integration is evaluated nearly exact. The integration can be done by using the adaptive Gauß-Kronrod quadrature. In fig. 4.9, the acoustic pressure at a line 20 mm in front of a fully reflecting interface with a length of 1 m and 1000 subdivisions can be seen calculated for 1 kHz and 8 kHz. Here, the acoustic pressure is calculated in case of a monopole and a dipole excitation integrating to  $k_r = k$  ( $\kappa = 0$ ) and integrating towards infinity. The sound source is placed at  $z_s = 100$  mm above the interface and the curves are compared to the exact solution using a mirror source. A sketch of the test case used here is depicted in fig. 4.8. It can be observed that the exact solution does not differ from the calculations using the complex valued angles of sound incidence. Furthermore, the imaginary part is equal for any cases. It can be seen that the upper limit corresponding to the angle



#### 4. Characterization of absorbers for high frequencies

of sound incidence of  $90^\circ$  is not sufficient for the calculation, since there can be found main deviations from the exact solution. These deviations get smaller, the higher the frequency and the distance to the sound source are.

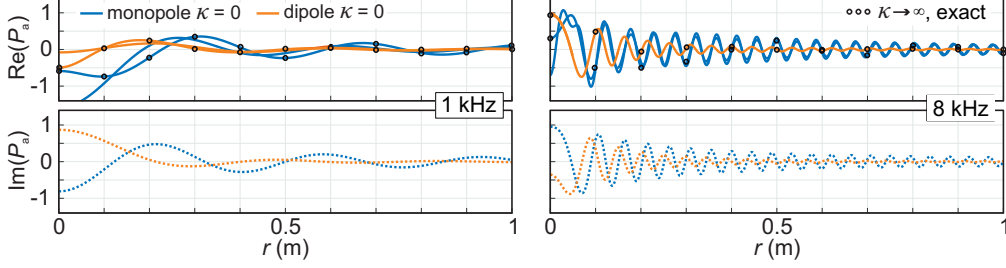


Figure 4.9.: Acoustic pressure relative to the maximum of the acoustic pressure of the direct wave calculated by using (2.54) and (2.59) for real and complex valued angles of sound incidence in comparison with the exact solution.

For a converged solution of the integral in (2.54) and (2.59), the sound pressure reflection coefficient has to converge with angles of sound incidence towards infinity. In fig. 4.10 the complex sound pressure reflection coefficient as a function of the complex angle of sound incidence is shown. For real valued angles of sound incidence, the real part as well as the imaginary part of the reflection coefficient are bounded by -1 and 1. For complex angles of sound incidence, both parts raise with higher angle of sound incidence above 1. Nonetheless, the sound pressure reflection coefficient shows convergence. The value of the converged reflection coefficient is higher, the higher the frequency of excitation is. The calculated acoustic pressure is used for obtaining the sound pressure reflection coefficient by using the spatial Fourier transform method (4.28) by evaluating the acoustic pressure on two lines. This calculated reflection coefficient  $R_{\text{SFT}}$  is compared to the one, used for the calculation of the sound field  $R_{\text{K}}$  by using the Komatsu model. That way, the inherent error of the method can be determined. The calculations are performed in a frequency range between 1 kHz and 10 kHz and in a range of angles of sound incidence between  $0^\circ$  and  $70^\circ$ .

To characterize the accuracy of the method, the overall absolute error relative to the frequency and angle range under consideration

$$E = \frac{1}{(70^\circ - 0^\circ)(10 \text{ kHz} - 1 \text{ kHz})} \int_{1 \text{ kHz}}^{10 \text{ kHz}} \int_{0^\circ}^{70^\circ} |R_{\text{SFT}} - R_{\text{K}}| d\theta_i df \quad (4.32)$$

is calculated. Furthermore, the error as a function of frequency

$$E_\theta = \frac{1}{(70^\circ - 0^\circ)} \int_{0^\circ}^{70^\circ} |R_{\text{SFT}} - R_{\text{K}}| d\theta_i \quad (4.33)$$

#### 4. Characterization of absorbers for high frequencies

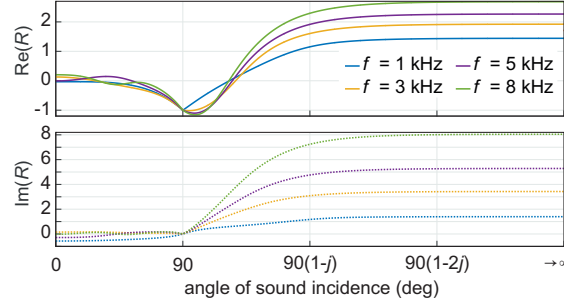


Figure 4.10.: Sound pressure reflection coefficient calculated with  $\sigma = 9.5$  kPa and  $d = 41$  mm backed by a rigid baffle as a function of the complex angle of sound incidence.

and as a function of angle of sound incidence

$$E_f = \frac{1}{(10 \text{ kHz} - 1 \text{ kHz})} \int_{1 \text{ kHz}}^{10 \text{ kHz}} |R_{\text{SFT}} - R_{\text{K}}| df \quad (4.34)$$

is calculated, to identify, at which frequencies and at which angles of sound incidence the parameter variation cause the largest error. If it is not mentioned otherwise, the parameters listed in tab. 4.2 are used.

Table 4.2.: Parameters to study the errors of the spatial Fourier transform method.

parameter(description)	value
sound source	dipole
height of sound source $z_s$	100 mm
height of measurement line at $z_1$	20 mm
distance between measurement lines $z_2 - z_1$	5 mm
radial discretization $\Delta r$	10 mm
length of measurement lines $z_{\text{max}}$	1 m

**Sound source** The spatial Fourier transform method does not need a special sound source. Even measurements by using ambient noise [114] are possible. It is obvious that the sound source used for the spatial Fourier transform method should have a large decay in  $r$ -direction to obtain a sufficient small  $r_{\text{max}}$  in (4.26). In fig. 4.9, the acoustic pressure along a measurement line is displayed. The decay of the dipole can be found to be larger than the one of the monopole. Hence, the usage of a dipole sound source in the measurement will reduce errors due to the finite length of the measurement line. In fig. 4.11, the calculated sound pressure reflection coefficient using a monopole and a dipole in comparison to the reference values are shown. In the upper plot, the sound pressure

#### 4. Characterization of absorbers for high frequencies

Table 4.3.: Errors of the calculated sound pressure reflection coefficient (4.32) using a monopole and dipole sound source.

Sound source	monopole	dipole
$E$	4.19%	0.76%

reflection coefficient is shown as a function of the angle of sound incidence. The sound pressure reflection coefficients in case of an excitation by means of a monopole sound source show ripples caused by the spatial Fourier transform of the finite measurement lines. These deviations depend on the frequency of excitation. The higher the frequency, the smaller the period of the ripples. However, the ripples can be reduced by using the dipole sound source. In the lower plot, the reflection coefficient can be seen as a function of frequency at perpendicular sound incidence. There can be observed main deviations inherent in the method from the reference values, when using a monopole sound source. The error calculated using (4.32) can be found in tab. 4.3. Here, the mean error by using a dipole sound source appears to be more than five times lower than the error by using the monopole sound source. Hence, the usage of a loudspeaker with a dipole polar pattern is essential in the implementation of the method.

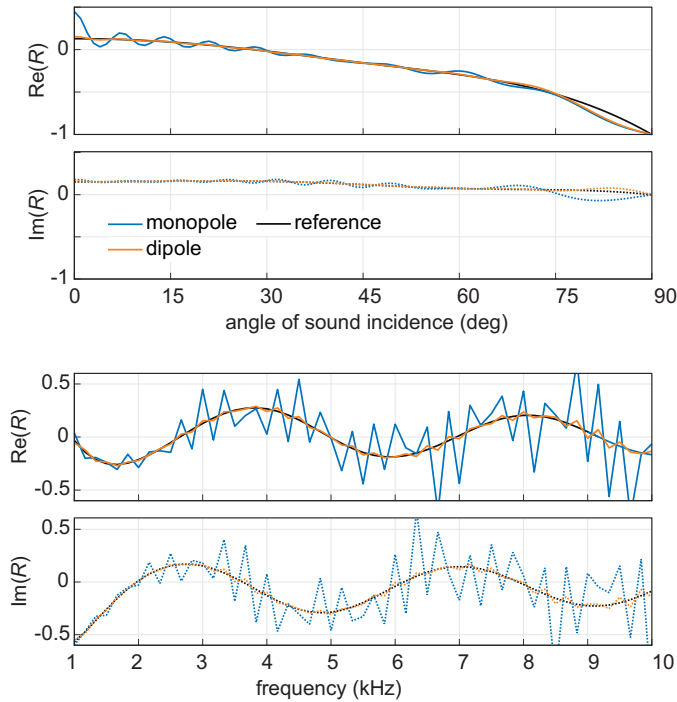


Figure 4.11.: Calculated sound pressure reflection coefficient at 3 kHz  $R_{\text{SFT}}$  as a function of the angle of sound incidence and as a function of frequency for perpendicular sound incidence using different sound sources in comparison to the reference value  $R_{\text{K}}$ .

#### 4. Characterization of absorbers for high frequencies

**Length of measurement lines** Since the length of the measurement line cannot be infinite, the influence of the length of the measurement line on the result of the sound pressure reflection coefficient has to be clarified. Especially, if a sound source with a low decay of acoustic pressure in  $r$ -direction is used, this is crucial, since the energy of the acoustic wave has to be fully recorded. The smaller the length of the measurement line, the more energy cannot be recorded in the measurement and the higher should be the error by using the spatial Fourier transform. The error as a function of angle of sound incidence and as a function of frequency can be seen in fig. 4.12. Here, the previous described phenomena can be observed. The shorter the measurement line, the higher is the error. The error seems to converge in some kind since the difference in the error by using 1 m and 1.5 m length of the measurement line is small. This is obvious, if the total error by using the different length of the measurement lines is compared, see tab. 4.4. Here, the overall error is reduced by a factor of three if the length is increased from 0.5 m to 1 m but only by 1.3, if the length is enlarged one more half of a meter. Moreover in fig. 4.12 one can see that the error inherent in the measurement method increases in all cases at the angle of sound incidence towards  $0^\circ$  and from  $75^\circ$  to  $90^\circ$ . Consequential, a length of the measurement of 1 m should be sufficient in the implementation of the method.

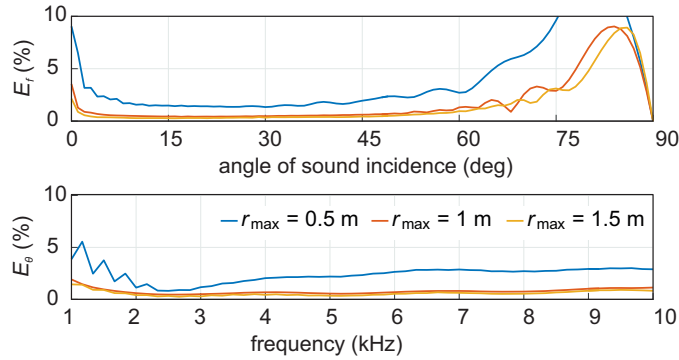


Figure 4.12.: Error  $E_f$  as a function of the angle of sound incidence and  $E_\theta$  as a function of frequency when using different length of measurement lines.

Table 4.4.: Error of the calculated reflection coefficient (4.32) using different length of the measurement line.

$r_{\max}$	0.5 m	1 m	1.5 m
$E$	2.39%	0.76%	0.57%

**Distance between sound source and sample** To use the directivity pattern of the dipole sound source efficiently in terms of amplitude decay, it is intuitive to place the sound source as near as possible in front of the sample. In the implementation of the method, the distance has to be large enough for two measurement lines between the

#### 4. Characterization of absorbers for high frequencies

sample and the sound source. Furthermore, the microphone will have a certain diameter, thus, the sound source has to be placed at a certain distance in front of the sample. In fig. 4.13 the influence of different distances between sound source and sample can be seen. The larger the distance, the larger the error gets. The overall error decreases with smaller distance, which can be seen in tab. 4.5. The decrease of the distance from 300 mm to 200 mm gives a benefit of 63% whereas a further decrease to 100 mm gives 72% better results. In conclusion, the distance between loudspeaker and sample has to be chosen as small as possible.

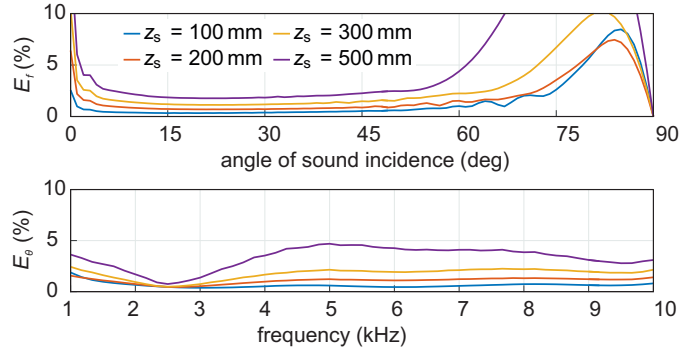


Figure 4.13.: Error  $E_f$  as a function of the angle of sound incidence and  $E_\theta$  as a function of frequency when using different distances between sound source and sample.

Table 4.5.: Error of the calculated reflection coefficient (4.32) using different distances between sound source and sample.

$z_s$	0.1 m	0.2 m	0.3 m	0.5 m
$E$	0.62%	1.07%	1.74%	3.29%

**Distance between the measurement lines and the sample** In fig. 4.14 the error as a function of frequency and angle of sound incidence for different distances between the measurement lines and the sample is shown. It roughly can be seen that the error can be reduced with smaller distances between the sample and the measurement lines. Especially at higher angles of sound incidence from  $75^\circ$  to  $90^\circ$  the error increases strongly with higher distances. The overall error also shows that a smaller error will occur, the smaller the distance is, see tab. 4.6. In the implementation of the measurement method, the distance cannot be chosen infinite small due to the diameter of the microphone. Hence, for the implementation of the method it is recommended that the measurement lines will be placed as near as possible to the sample.

**Radial discretization** The influence of the distance between the measurement lines and the radial discretization is of similar character. Increasing both parameters will result

#### 4. Characterization of absorbers for high frequencies

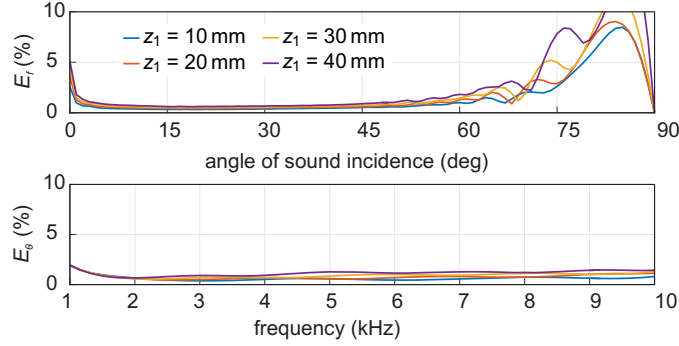


Figure 4.14.: Error  $E_f$  as a function of the angle of sound incidence and  $E_\theta$  as a function of frequency when using different distances between the measurement lines and sample.

Table 4.6.: Error of the calculated reflection coefficient (4.32) using different distances between the measurement lines and sample.

$z_1$	10 mm	20 mm	30 mm	40 mm
$E$	0.62%	0.76%	0.92%	1.13%

in errors due to spatial aliasing, if the acoustic wavelength cannot be resolved for higher frequencies. In fig. 4.15 the errors as a function of angle of sound incidence and frequency using different radial discretization increments are displayed. The error is significant at large angles of sound incidence from  $45^\circ$ . At lower angles of sound incidence, the error is smaller, the smaller the discretization is. In the error as a function of frequency the influence of spatial aliasing can be seen, since the error rises at the radial discretization of 20 mm at frequencies above 8.8 kHz. However, the error is lower at all frequencies when the discretization is chosen smaller. The influence of the radial discretization can also be observed in the overall error, see tab. 4.7. The smaller the  $\Delta r$ , the smaller the error. Changing the radial distance between two measurement points from 15 mm to 10 mm gives a benefit of 56% in error. A further reduction of the  $\Delta r$  to 5 mm doubles the measurement time but only decreases the error with 15%. Thus, a radial discretization of 10 mm should be sufficient.

Table 4.7.: Error of the calculated reflection coefficient (4.32) using different radial discretization.

$\Delta r$	5 mm	10 mm	15 mm	20 mm
$E$	0.66%	0.76%	1.19%	2.76%

**Distance between the measurement lines** In fig. 4.16, the error as function of angles of sound incidence using different distances between the measurement lines can be seen. The error is always higher with increasing distance between the measurement lines except

#### 4. Characterization of absorbers for high frequencies

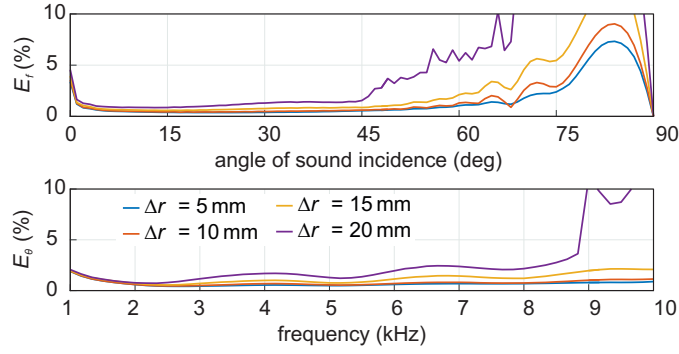


Figure 4.15.: Error  $E_f$  as a function of the angle of sound incidence and  $E_\theta$  as a function of frequency when using different radial discretization.

at certain angles at  $68^\circ$ ,  $75^\circ$  and above  $85^\circ$ . It has to be remarked that the main influence of a larger distance between the measurement lines can be detected at small angles of sound incidence and at higher frequencies. Here it is assumed that spatial aliasing occurs. The overall error (tab. 4.8) shows that the smaller the distance between the measurement lines is, the smaller is the expected error. A small distance between the two measurement lines can be disadvantageous due to a smaller gradient of the acoustic pressure between two measurement points. This can lead to errors especially at low frequencies and corresponding long acoustic wave lengths, since the resolution of the measurement system to record the acoustic pressure is finite.

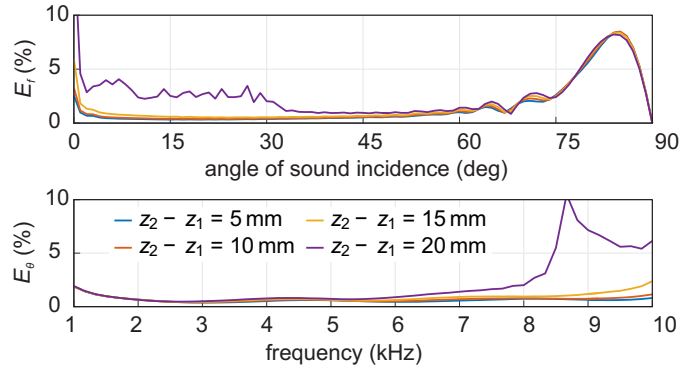


Figure 4.16.: Error  $E_f$  as a function of the angle of sound incidence and  $E_\theta$  as a function of frequency when using different distances between the measurement lines.

Table 4.8.: Error of the calculated reflection coefficient (4.32) using different distances between the measurement lines.

$z_2 - z_1$	5 mm	10 mm	15 mm	20 mm
$E$	0.62%	0.68%	0.86%	2.03%

### Implementation of the spatial Fourier transform method

For a homogeneous sample, it is sufficient to perform a 1D spatial Fourier transform. Therefore, the BK 4187 1/4" microphone in the measurement is mounted on a 2D gantry by means of a tube with length 105 cm. The gantry allows to scan the sound field above the sample produced with a sound source in a range of 195 cm x 20 cm. The sound source shows a dipole like polar pattern, whereas the axis of the sound source is arranged perpendicular to the surface of the planar sample. In the left part of fig. 4.17 the measurement setup can be seen. Here, the setup is shown during measurements above a rock wool sample. Furthermore, in the right part of fig. 4.17, the schematic of the measurement setup is displayed. Here, the power amplifier for the excitation of the loudspeaker and the data acquisition along with the PC are shown. The evaluation of the recorded acoustic pressure is done by means of the calculation of the impulse response, similar to the procedure described in Sec. 2.6 using a time window with a constant length. This can result in errors at low frequencies due to a slower decay of the impulse response. The measurements are performed in an ordinary room, where the nearest object is more than 1.05 m away. Thus, the first parasitic part of the impulse response can be expected at 6.12 ms, which justifies the chosen time window with length of 6 ms. The excitation signal is a MLS-signal with length  $2^{19} + 1$  and the measurement time will be approximately 10 s with 50,000 samples/s.

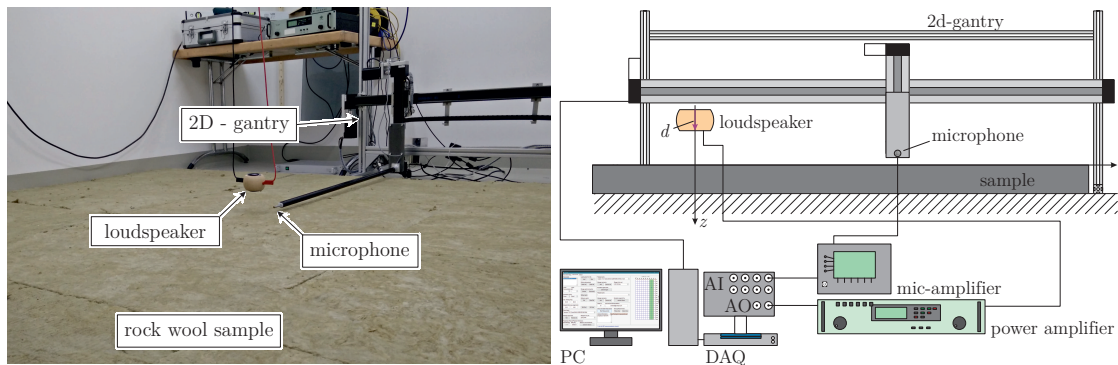


Figure 4.17.: Measurement setup. Left: 2D-gantry with mounted microphone arranged with a sound source above a 4 m<sup>2</sup> rock wool sample. Right: Schematic of the measurement setup.

### Characterization of the measurement setup

The characterization of the measurement setup is done in a similar way as the previous characterization of the method's accuracy presented in Sec. 4.1.2. The determination of the sound pressure reflection coefficient is on the one hand conducted using a perfect absorber plane. This means, the measurements were done on an air-air interface with no absorption, where the sound pressure reflection coefficient is zero. On the other hand, the measurement setup is characterized by the determination of the sound pressure reflection



#### 4. Characterization of absorbers for high frequencies

coefficient of an air–absorber interface, whereas the absorber consists of a rock wool sample with thickness of 40 mm. The determined sound pressure reflection coefficient in both test cases is compared to the reference, in case of a perfect absorber plane with zero and in case of the rock wool sample with the calculated sound pressure reflection coefficient by using the Komatsu model. Furthermore, the overall errors  $E_{\text{perf}}$  in case of a perfect absorbing plane and  $E_{\text{rock}}$  in case of the rock wool sample are computed by using (4.32).

**Sound source** The first parameter under investigation is the sound source used in the measurement setup. The sound source consists of two Visaton BF45 in a spherical containment made of wood. These two loudspeakers are driven inverse to each other and the resulting polar pattern at different frequencies can be seen in the left part of fig. 4.18. The sound pressure level is shown relative to the maximum of each frequency. It can be observed that the polar pattern shows a figure of eight up to 5 kHz. The higher the frequency of excitation, the more side loops can be detected. However, the sound pressure level is minimum at  $90^\circ$  and  $270^\circ$  in all frequencies of excitation. Additionally, at 5 kHz, the sound pressure level at  $0^\circ$  is lower than the one at  $180^\circ$ . Nevertheless, the sound source can be assumed to show a dipole behavior at low frequencies. Moreover, the sound pressure level as a function of frequency at the angles  $0^\circ$ ,  $90^\circ$ ,  $180^\circ$  and  $270^\circ$  is shown in the right part of fig. 4.18. Due to the difference in level at the four angles, the sound pressure level is shown relative to the highest level along the rotation angle at  $0^\circ$  and 2.3 kHz. It can be seen that the difference between maximum and minimum at nearly all frequencies is higher than 20 dB. This difference is a measure for the dipole behavior of the sound source and crucial for a proper determination of the sound pressure reflection coefficient by means of the spatial Fourier transform method.

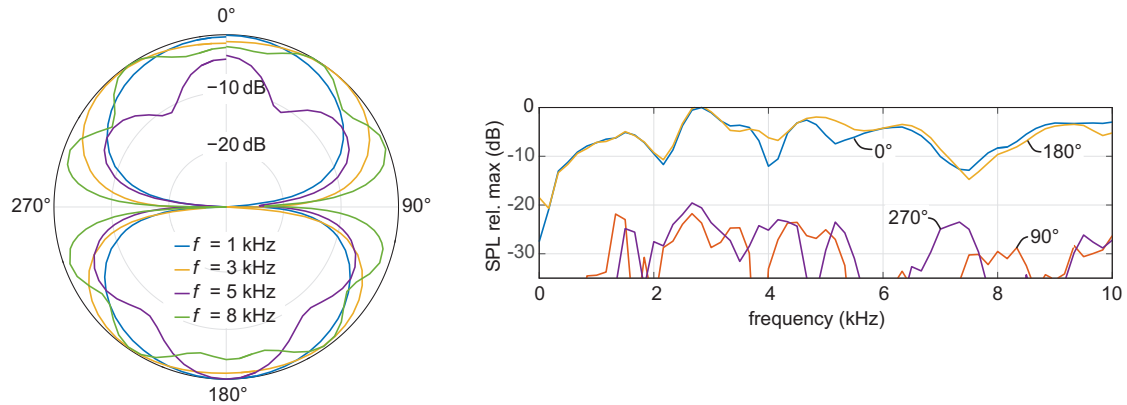


Figure 4.18.: Characterization of the sound source. Left: polar pattern at different frequencies. Right: sound pressure level as a function of frequency at various angles.

In fig. 4.19 the absolute error in the obtained sound pressure reflection coefficient of measurements on a perfect absorber plane (free field measurement) is displayed. In this

#### 4. Characterization of absorbers for high frequencies

test case, the sound pressure reflection coefficient should be zero for all angles of sound incidence and all frequencies. It can be seen that in particular at perpendicular sound incidence ( $0^\circ$  angle of sound incidence), the method produces errors in determining the sound pressure reflection coefficient. Furthermore, a major error can be found at higher angles of sound incidence due to the limited length of the measurement lines with 1 m. Moreover, a number of peaks in the error in a small frequency range around 5.2 kHz at angles of sound incidence between  $15^\circ$  and  $45^\circ$  and between 7 kHz and 8 kHz at small angles of sound incidence below  $15^\circ$  can be observed. In the frequency range around 5.2 kHz, the first side lobes occur in the polar pattern of the sound source, which can cause the error due to a small signal amplitude between the main lobe and a side lobe. In the frequency range between 7 kHz and 8 kHz the problem is of same nature, since at 8 kHz the level of the first side lobe is higher than the main lobe, which can be seen in the left part of fig. 4.18. However, the error in the frequency range of 1 kHz to 10 kHz and at the angles of sound incidence between  $1^\circ$  and  $70^\circ$  can be found to be below 10 % and with an average of 3.18 %.

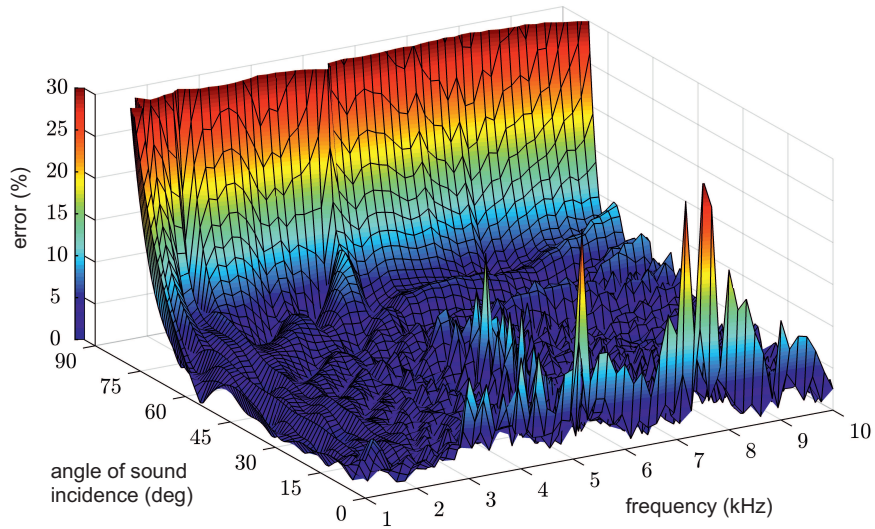


Figure 4.19.: Absolute values of the error in the sound pressure reflection coefficient of measurements ( $z_1 = 35$  mm and  $z_2 = 40$  mm) on a perfectly absorbing plane  $|R_{\text{SFT}} - 0|$  as a function of angle of sound incidence and excitation frequency.

**Length of measurement lines** As can be seen in the previous numerical investigation, the length of the measurement lines has an influence on the upper bound of the angle of sound incidence. In fig. 4.20 the error in the measurements with different lengths of measurement lines using a perfect absorber plane and a rock wool absorber can be seen. In good agreement to tab. 4.4, a convergence of the error can be found. In tab.

#### 4. Characterization of absorbers for high frequencies

4.9 the overall errors in both test cases are displayed, whereby the stronger convergence of the error in case of a measurement of a rock wool absorber is obvious. Whereas the increasing of the length from 0.3 m to 0.5 m reduces the total error with 39%, a further increasing is scarce. Thus, for the characterization of absorbers for high frequencies a length of the measurement lines of 1 m is used.

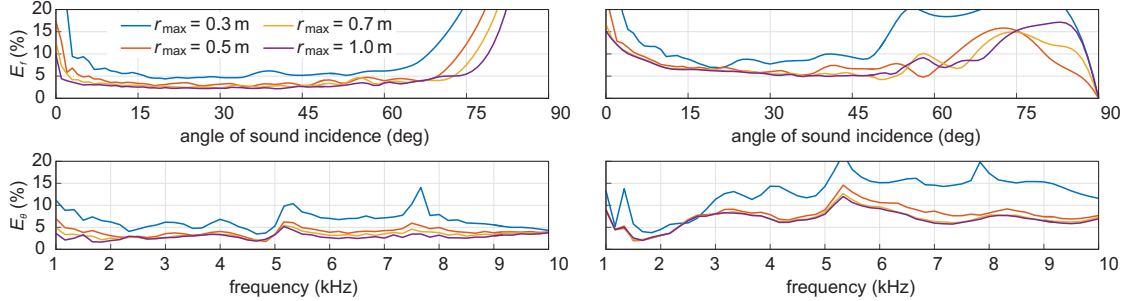


Figure 4.20.: Error  $E_f$  as a function of the angle of sound incidence and  $E_\theta$  as a function of frequency when using different length of measurement lines. Left: Measurement using a perfectly absorbing plane. Right: Measurement of a rock wool absorber.

Table 4.9.: Error of the calculated reflection coefficient using different length of the measurement lines.

$r_{\max}$	0.3 m	0.5 m	0.7 mm	1.0 m
$E_{\text{perf}}$	6.58%	3.95%	3.31%	2.89%
$E_{\text{rock}}$	13.0%	7.90%	7.05%	6.87%

**Distance between sound source and sample** The numerical characterization of the spatial Fourier transform method suggests the assumption to place the sound source as near as possible to the sample under test for the whole frequency range of interest. In fig. 4.21 the error in case of a perfect absorber plane and in a measurement at an absorber using different distances between the sound source and sample can be seen. In exactly the same way as in fig. 4.13, the measurements using larger distance between sound source and sample shows higher errors except at angles of sound incidence above  $75^\circ$  in case of a perfect absorber plane. In tab. 4.10 the overall error in both test cases is listed. Here, the error in case of the perfect absorber plane is smaller than the one in case of measurements at the rock wool sample, too. Furthermore, here the overall error supports the assumption that the nearer the sound source is placed to the sample, the smaller gets the inherent error of the measurement method. Placing the sound source 200 mm instead of 100 mm above the sample will increase the overall error by 48% (perfect absorber plane) and 30% (rock wool absorber). Additionally in both cases the weakness of the sound source in the frequency range around 5.2 kHz can be noticed.

#### 4. Characterization of absorbers for high frequencies

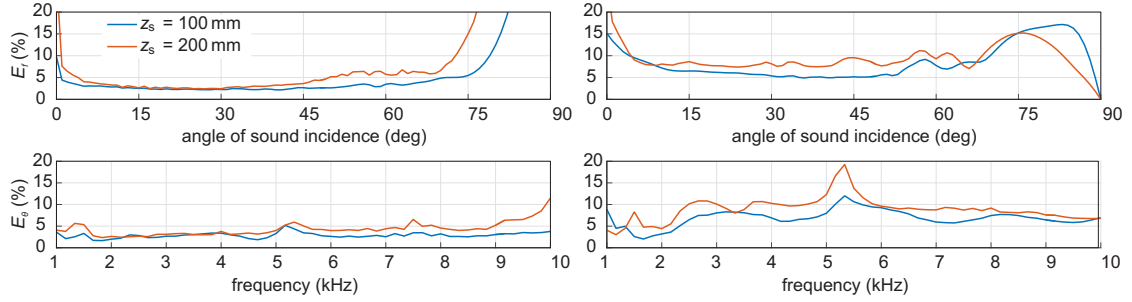


Figure 4.21.: Error  $E_f$  as a function of the angle of sound incidence and  $E_\theta$  as a function of frequency when using different distances between sound source and sample. Left: Measurement using a perfectly absorbing plane. Right: Measurement of a rock wool absorber.

Table 4.10.: Error of the calculated reflection coefficient using different distances between sound source and sample.

$z_s$	100 mm	200 mm
$E_{\text{perf}}$	2.89%	4.29%
$E_{\text{rock}}$	6.87%	8.96%

The previous statements are valid in a frequency range above 1.5 kHz. At lower frequencies in case of measurements at the absorber (see right part of fig. 4.21), the error by using a larger distance between the sound source and the sample is lower than by using a smaller distance. This is obvious, since the decay of acoustic pressure along the measurement lines gets larger the lower the frequency of excitation is. This means that the sample is excited in a smaller region, which will cause errors especially at higher angles of sound incidence. If the angles of interest are large and the frequency under investigation is low, the sound source has to be placed at a larger distance to the sample, than in a case, were the frequencies of interest are higher than 1.5 kHz. However, in the following measurements, a distance between the sample and the sound source is chosen with 100 mm to obtain small errors in the determination of the sound pressure reflection coefficient at frequencies above 1.5 kHz.

**Distance between the measurement lines and the sample** By means of tab. 4.6, the recommendation has been derived, to place the measurement lines as near as possible to the sample. Nevertheless the influence of the distance between the measurement lines and the sample has found to be less important than the other parameter variations. In fig. 4.22 the errors as a function of angle of sound incidence and frequency by using different distances between the measurement lines and the sample are displayed. In case of the measurements of the rock wool sample, the errors show similar behavior as can be observed in fig. 4.14. The main influence of the distance between the measurement lines and the sample can be observed at angles of sound incidence above  $60^\circ$ . At angles of

#### 4. Characterization of absorbers for high frequencies

sound incidence larger than  $60^\circ$  the error is smaller, the smaller the distance between the measurement lines and the sample is. The overall error in case of the measurements of the rock wool sample, listed in tab. 4.11 support this suggestion. In case of measurements of a perfect absorber this considerations cannot be confirmed. Basically, a smaller error with smaller distances between measurement lines and sample can be expected due to the amplitude decay of the reflected wave. However, the measurements of a perfect absorbing plane are not obvious concerning this matter. However, the distance between the measurement lines and the sample is chosen to be 20 mm in the further measurements.

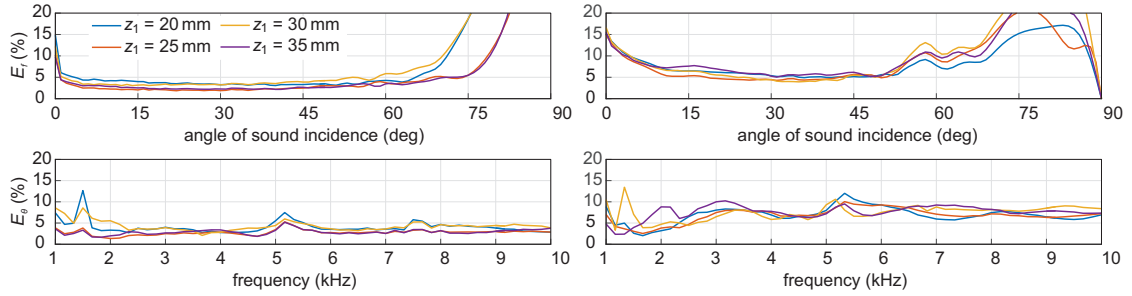


Figure 4.22.: Error  $E_f$  as a function of the angle of sound incidence and  $E_\theta$  as a function of frequency when using different distances between the measurement lines and the sample. Left: Measurement using a perfectly absorbing plane. Right: Measurement of a rock wool absorber.

Table 4.11.: Error of the calculated reflection coefficient using different distances between the measurement lines and the sample.

$z_1$	20 mm	25 mm	30 mm	35 mm
$E_{\text{perf}}$	4.04%	2.77%	4.28%	2.89%
$E_{\text{rock}}$	6.87%	6.78%	7.42%	7.62%

**Radial discretization** In fig. 4.15 errors due to spatial aliasing caused by a large radial discretization increment and a large distance between the measurement lines has been observed. In fig. 4.23 the errors as a function of angle of sound incidence and frequency using different radial discretization of the measurement lines can be seen. The error rises at larger angles of sound incidence and higher frequencies with coarser radial discretization. It can be observed that the spatial aliasing in case of a perfect absorber occurs at frequencies above 7 kHz and in case of measurements of an absorber at frequencies higher than 9 kHz. Furthermore, in case of a perfect absorber the effect occurs at lower angles of sound incidence. Here, the error rises at angles larger than  $34^\circ$  whereas the error rises in case of an absorber at angles above  $46^\circ$  due to a coarse radial discretization. It can be ascertained that in measurements in a frequency range up to 10 kHz a spatial discretization of 10 mm is sufficient. The influence of the radial discretization also can

#### 4. Characterization of absorbers for high frequencies

be noticed in the overall error, listed in tab. 4.12. Here, it is obvious that the reduction of a radial increment from 20 mm to 15 mm or 10 mm gives much better results. A further reduction is not useful since the measurement effort rises and the error converges. Therefore, the radial discretization increment used in the measurements is chosen to be 10 mm.

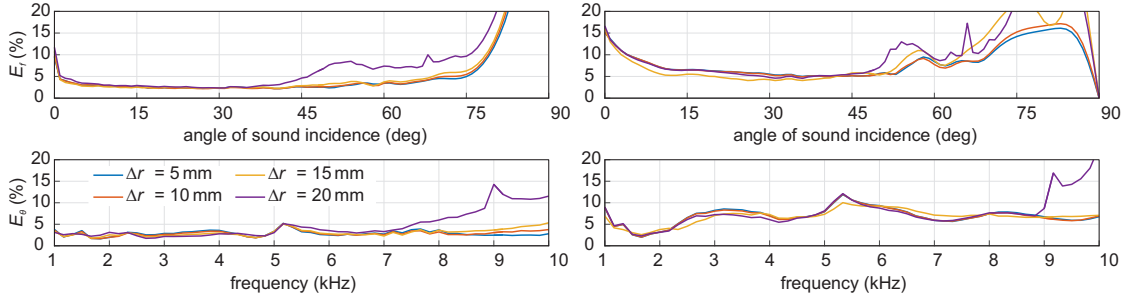


Figure 4.23.: Error  $E_f$  as a function of the angle of sound incidence and  $E_\theta$  as a function of frequency when using different radial discretization. Left: Measurement using a perfectly absorbing plane. Right: Measurement of a rock wool absorber.

Table 4.12.: Error of the calculated reflection coefficient using different radial discretization.

$\Delta r$	5 mm	10 mm	15 mm	20 mm
$E_{\text{perf}}$	2.87%	2.89%	3.03%	4.61%
$E_{\text{rock}}$	6.94%	6.87%	6.77%	7.76%

**Distance between the measurement lines** The error as a function of the angle of sound incidence and frequency of both test cases using different distances between the measurement lines can be seen in fig. 4.24. Here, the spatial aliasing can be observed at small angles of incidence and high frequencies with coincidence to the findings in the numerical investigation. However, the error rises for a distance between the measurement lines of 25 mm for angles of sound incidence smaller than  $45^\circ$  and frequencies higher than 6.8 kHz for both cases. Furthermore, the spatial aliasing effect can be seen in the measurement of the rock wool sample using a distance between the measurement lines of 15 mm at frequencies higher than 8.7 kHz. In tab. 4.13 the overall errors are listed. Here, the assumption can be derived that for measurements in a frequency range up to 10 kHz the distance between the measurement lines should be 10 mm. Larger distances will effect spatial aliasing at high frequencies but a smaller distance will reduce the quality of the measurement result due to a smaller pressure gradient between the two measurement lines. Hence, in the following measurements a distance between both measurement lines of 10 mm is used.

#### 4. Characterization of absorbers for high frequencies

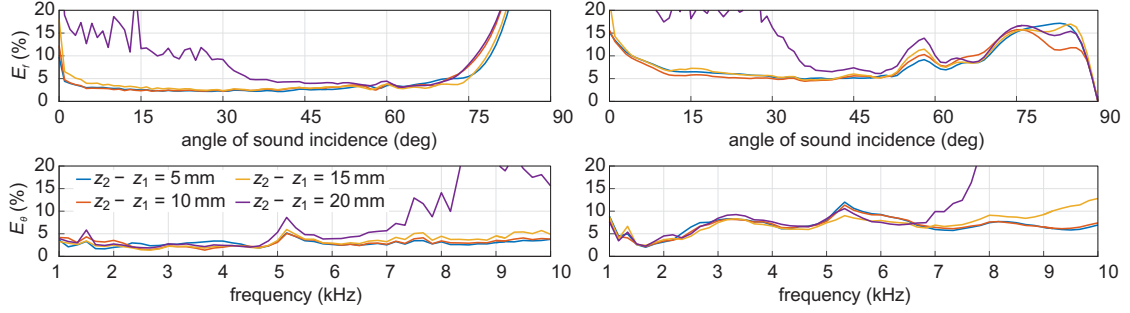


Figure 4.24.: Error  $E_f$  as a function of the angle of sound incidence and  $E_\theta$  as a function of frequency when using different distances between the measurement lines. Left: Measurement using a perfectly absorbing plane. Right: Measurement of a rock wool absorber.

Table 4.13.: Error of the calculated reflection coefficient using different distances between the measurement lines.

$z_2 - z_1$	5 mm	10 mm	15 mm	20 mm
$E_{\text{perf}}$	2.89%	2.96%	3.25%	8.28%
$E_{\text{rock}}$	6.87%	6.82%	7.29%	15.0%

**Conclusion/Recommendations** In the previous characterization presented in Sec. 4.1.2 it is shown that the arrangement of the measurement setup can have a major influence on the errors caused by the method itself. Applying a sound source with dipole like directivity pattern is essential particularly in connection with a finite length of the sample under test and finite lengths of the measurement lines  $r_{\text{max}}$ . A larger  $r_{\text{max}}$  implicates more accurate results but also increases the measurement time. For measurements using the sound source consisting of two Visaton BF45, a length of the measurement lines of 1 m seems to be sufficient. The error inherent in the method appears to be sensitive to the distance between sample and sound source  $z_s$ . It has been shown that a small  $z_s$  is beneficial. Hence, the loudspeaker will be placed 100 mm in front of the sample to utilize the directivity pattern of the sound source. Furthermore, the distance of the measurement lines and the sample  $z_1$  is important for accurate determining the acoustic surface properties. A smaller distance  $z_1$  ensures a better measurement result. Since the distance is limited by the dimensions of the microphone,  $z_1$  is chosen to be 20 mm in the following measurements. A coarse radial discretization can cause errors at higher frequencies. Thus, a smaller discretization increment  $\Delta r$  gains a benefit in terms of small errors but increases the measurement time. Hence, for a frequency range up to 10 kHz a  $\Delta r$  of 10 mm is adequate. Additionally, the distance between the measurement lines can lead to inaccurate results at high frequencies due to spatial aliasing, if the distance is chosen too large. For a precise identification of the acoustic surface properties at high frequencies, a small distance is advantageous. Nevertheless, with small distances between the measurement lines the pressure gradient at low frequencies cannot be re-

solved, which yields to inexact measurement results. A reasonable compromise can be a distance between the measurement lines of 10 mm.

## 4.2. Acoustic surface properties of absorbers for high frequencies

In this section the measurement results obtained by the optimized implementations of the subtraction method (Sec. 4.1.1) and the spatial Fourier transform method (Sec. 4.1.2) are presented. The measurement setup for the subtraction method can be found in Sec. 4.1.1. For the spatial Fourier transform method the sound source showing dipole polar pattern is used and placed 100 mm in front of the sample. Furthermore, the measurement lines are placed 20 mm in front of the sample with a distance of 10 mm to each other. The measurement lines are recorded at a total length of 1 m with a radial discretization increment of 10 mm. The samples under test consist of Sonorock rock wool samples with different thicknesses. The samples are hard backed, in case of the in situ measurements by a rigid concrete floor. During the tube measurement following ISO 10534-2, the samples are backed by means of a rigid steel panel, whereas the measurements with the transfer matrix method (ASTM E2611-09) are conducted without backing. Here, the influence of a hard backing can be added in the post processing. The characterization of the air-absorber interface is done at perpendicular and at oblique angles of sound incidence. In both measurements, in case of the subtraction method and the spatial Fourier transform method, the result is the angle- and frequency dependent sound pressure reflection coefficient of the interface. These measurement results are compared with the theoretical values calculated by means of the Komatsu model using an equivalent fluid with a flow resistivity of  $9.5 \text{ kPa/m}^2$ .

### 4.2.1. Perpendicular sound incidence

The results of the determined sound pressure reflection coefficients at perpendicular sound incidence by means of the methods described in Sec. 4.1 can be compared with the standardized measurement methods following ISO 10534-2 [4] and ASTM E2611-09 [9]. In fig. 4.25, the absolute value of the sound pressure reflection coefficient at an air-absorber interface for a 40 mm rock wool sample as a function of the excitation frequency is displayed. It has to be mentioned that the standardized measurement methods give unreliable results for frequencies above 6.4 kHz, the frequency of the first transverse mode of the tube. Hence, this measurement results are just shown up to 6.4 kHz. In the following, the absolute value of the sound pressure reflection coefficient is investigated, since the physical interpretation of the complex value in case of the real and imaginary part is difficult and not intuitive. It is obvious that the absolute values of the sound pressure reflection coefficient decrease with higher frequency of excitation, since more acoustic energy is absorbed by friction in the absorber material. The results of the two standard measurement methods differ from each other and furthermore, both differ from the sound pressure reflection coefficient calculated by means of the Komatsu



#### 4. Characterization of absorbers for high frequencies

model. The result of the ISO seems to be shifted to higher frequencies in comparison to the theoretical value using the Komatsu model. Furthermore, the measurement result by using the transfer matrix method shows more ripples. The reduction factor in the subtraction method can be determined with 33.07 dB. According to [5], a reduction factor more than 10 dB is sufficient. However, the result of the subtraction method seems to match the theoretical values in the mid frequency range between 2.5 kHz and 5 kHz quite well and shows main deviations above 5 kHz. The results using the spatial Fourier transform methods shows a large error, which suggests the assumption, that this method is not suitable for the characterization under perpendicular angle of sound incidence.

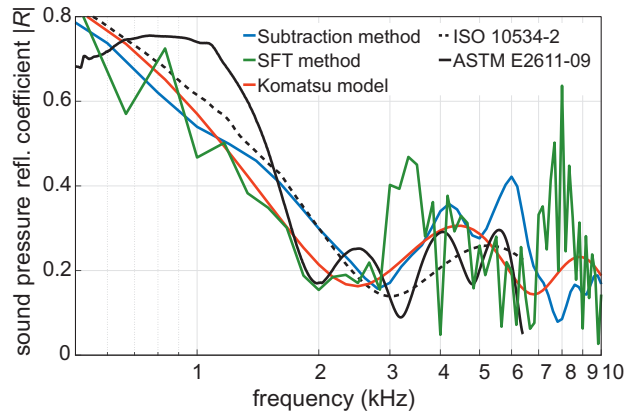


Figure 4.25.: Absolute value of the sound pressure reflection coefficient of a 40 mm rock wool sample measured with the spatial Fourier transform (SFT) method, the subtraction method and the two standard techniques by means of the absorption tube (ISO 10534-2) and the transmission loss tube (AST E2611-09) in comparison to the theoretical values calculated by means of the Komatsu model as a function of frequency and perpendicular angle of sound incidence.

#### 4.2.2. Oblique angles of sound incidence

On the other hand the characterization of the air-absorber interface under oblique angle of sound incidence is object of interest. In fig. 4.26, the absolute value of the sound pressure reflection coefficients as a function of frequency of a 40 mm rock wool sample measured with the subtraction method and spatial Fourier transform method at the angles of sound incidence  $15^\circ$ ,  $30^\circ$ ,  $45^\circ$  and  $60^\circ$  are shown. The reduction factor of the subtraction process can be determined at each angle of sound incidence with approximately 30 dB. The absorption in the material increases with higher angles of sound incidence since the path of the traveling wave raises. Especially in the frequency range between 5 kHz and 10 kHz and below 2 kHz this increase is evident. Below the excitation frequency of 3 kHz it is clearly recognizable that the results of the spatial

#### 4. Characterization of absorbers for high frequencies

Fourier transform method matches better to the reference than the one of the subtraction method. The results of the subtraction method furthermore shows an unreliable peak at 6 kHz probably caused by resonance effects in the rock wool sample.

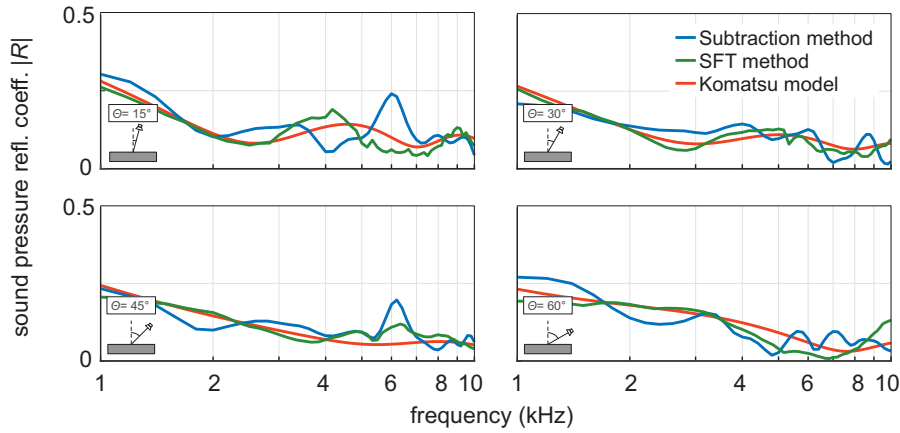


Figure 4.26.: Absolute value of the sound pressure reflection coefficient of a 40 mm rock wool sample measured with the spatial Fourier transform (SFT) method and the subtraction method in comparison to the theoretical values calculated by means of the Komatsu model as a function of frequency at different angle of sound incidence.

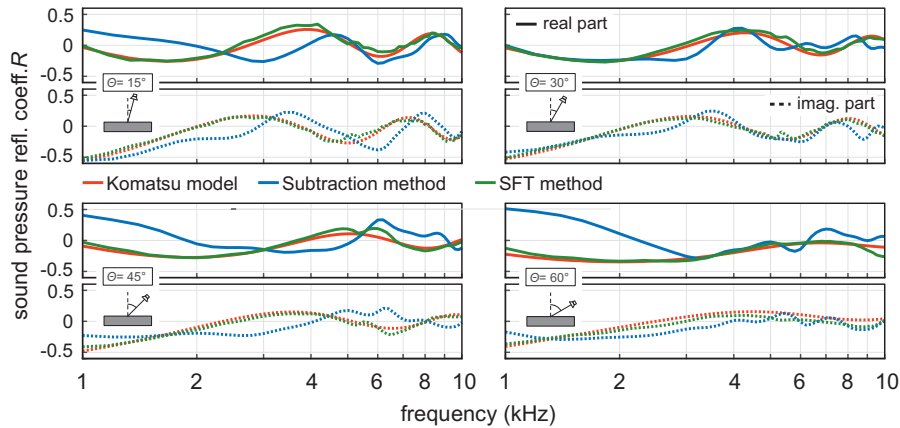


Figure 4.27.: Sound pressure reflection coefficient of a 40 mm rock wool sample measured with the spatial Fourier transform (SFT) method and the subtraction method in comparison to the theoretical values calculated by means of the Komatsu model as a function of frequency at different angles of sound incidence.

However, for an efficient evaluation of a complex value like the sound pressure reflection coefficient, the investigation of the absolute value is not sufficient. Therefore, the real and

#### 4. Characterization of absorbers for high frequencies

imaginary part of the sound pressure reflection coefficient measured with both methods in comparison to the reference values calculated by means of the Komatsu model as a function of frequency are displayed in fig. 4.27. Here, again the characterization is done under several angles of sound incidence. Moreover, the same values are shown as a function of angles of sound incidence at the frequencies 1 kHz, 3 kHz, 5 kHz and 8 kHz in fig. 4.28. In both representations of the measurement results the advantage of the spatial Fourier transform method is evident. In general, the results of the spatial Fourier transform method seems to match much more better with the theoretical values. Moreover, the measurement by using the subtraction method only can determine the acoustic properties at one angle of incidence at once, which makes the measurement process very time costly and demanding, since, the implementation in this thesis is not automated. Of course, a motion unit for a data set for a large range of angles of sound incidence would be useful in this case, but is not considered in the implementation of the method in this thesis. However, in fig. 4.27 it can be observed that the main deviations of the subtraction method from the theoretical values of the sound pressure reflection coefficient can be found at frequencies smaller than 3 kHz. The deviation seems to get smaller the higher the frequency of excitation is. Furthermore, the results matches the reference better, the smaller the angle of sound incidence is. This is obvious, since in this method the assumption on the interface under investigation is done that the incoming and the outgoing acoustic pressure wave is of spherical nature. Hence, for a perpendicular angle of sound incidence, this assumption can be done without limitation, but the larger the angle of sound incidence, the more the assumption is inaccurate. Nevertheless, in the measurement results using the spatial Fourier transform method some deviations from the reference can be seen. Especially at 5.2 kHz, where the sound source show large side lobes in the polar pattern, particularly in the imaginary part at the angle of sound incidence of  $15^\circ$ ,  $30^\circ$  and  $45^\circ$  main deviations can be noticed. In addition, the real part in case of small angles of sound incidence at higher frequencies from 4 kHz shows a rough curve whereas the reference is smooth. On top of this, the deviation in case of the spatial Fourier transform method are larger, the higher the frequency of excitation is. At frequencies smaller than 2.5 kHz almost no difference to the reference values can be detected.

In fig. 4.28, the sound pressure reflection coefficient of the 40 mm rock wool sample represented as real and imaginary part as a function of angle of sound incidence can be seen for four frequencies of excitation. Here, the measurement results of both methods in comparison to the reference values are displayed. Moreover, the theoretical values, calculated by means of an ideal dipole for excitation are shown. It can clearly been seen that the real part of the sound pressure reflection coefficient decreases with higher angles of sound incidence and gets -1 towards  $90^\circ$ . Here again, it can be seen that the deviations from the reference values in case of the spatial Fourier transform method are much smaller than the one of the subtraction result. The deviations using the subtraction method can found to be smaller, for smaller angles of sound incidence and higher frequencies of excitation. At the excitation frequency of 1 kHz, the imaginary part and at 3 kHz the real part of the spatial Fourier transform results show smaller deviations from the reference values than the calculated theoretical result. Additionally,

#### 4. Characterization of absorbers for high frequencies

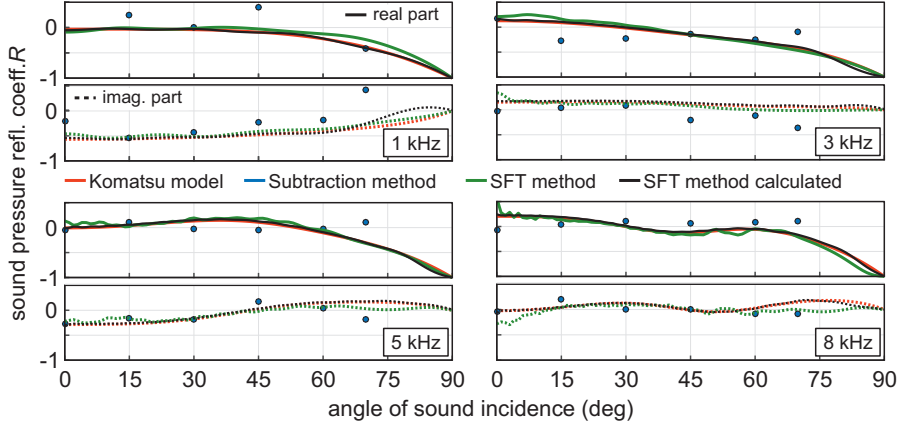


Figure 4.28.: Sound pressure reflection coefficient of a 40 mm rock wool sample measured with the spatial Fourier transform (SFT) method and the subtraction method in comparison to the theoretical values calculated by means of the Komatsu model as a function of the angle of sound incidence at different frequencies of excitation.

it can be observed that the deviation from the reference can be mainly found at high angles of sound incidence above  $75^\circ$ . Furthermore, the weakness of the spatial Fourier transform method for very small angles of sound incidence towards  $0^\circ$  can be seen. This disadvantage emerges, the higher the excitation frequency is. Nevertheless, the measurement results of the spatial Fourier transform method can be evaluated to be within an outstanding congruence with the reference values provided by the Komatsu model in a wide frequency spectrum between 1 kHz and 9 kHz and a large range of angles of sound incidence up to  $75^\circ$  with a weakness at perpendicular sound incidence and in a small frequency range around 5.2 kHz.

As a last point, the absorption coefficient of rock wool samples with different thicknesses between 50 mm and 100 mm as a function of frequency at an angle of sound incidence of  $15^\circ$  is shown in fig. 4.29. Here, the measurement results obtained by the spatial Fourier transform in comparison to the reference values can be seen. The absorption coefficient is the higher, the higher the frequency of excitation is. Furthermore, the absorption in the material increases with a larger thickness of the absorber especially at lower frequencies. Moreover, the measurement results show less deviations from the reference value obtained by the Komatsu model, the higher the absorption coefficient is. This circumstance suggests the assumption that a measurement of an high reflecting interface such as a rigid wall lead to unavoidable measurement uncertainties. Problems like these are also reported in literature [87].

#### 4. Characterization of absorbers for high frequencies

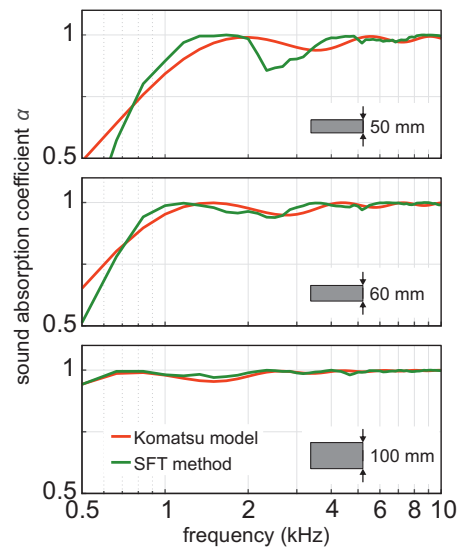


Figure 4.29.: Absorption coefficient of rock wool samples with different thicknesses measured with the spatial Fourier transform method in comparison to the theoretical values calculated by means of the Komatsu model as a function of frequency at an angle of sound incidence of  $15^\circ$ .

## 5. Absorbers for low frequencies

Porous absorbers have a major disadvantage at low frequencies, because there is a drop down in the absorption coefficient. In fig. 5.1, the sound absorption coefficient of such a traditional hard backed layer of absorber can be seen. It is obvious that the frequency, where the absorption coefficient drops down can be shifted to lower frequencies by increasing the thickness of the absorber. The decrease can be found, where the thickness is about a quarter of the acoustic wavelength in air. This means that an acoustic absorber has to be designed with a depth of nearly one meter to absorb efficiently at e.g. 100 Hz and thus is not feasible in practice.

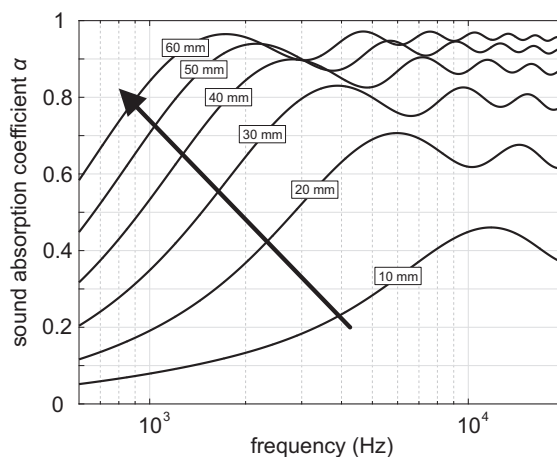


Figure 5.1.: Sound absorption coefficient at perpendicular sound incidence of a hard backed porous absorber with different thicknesses calculated by using (A.3) and (A.4) with  $\sigma = 6 \text{ kPas/m}^2$  in combination with (2.36), (2.37) and (2.38).

The mass law [23] [124]

$$STL_{\max} = 20 \log \left( \frac{\pi f \rho_w d}{\rho_0 c} \right) - 10 \log \left( 0.23 \cdot 20 \log \left( \frac{\pi f \rho_w d}{\rho_0 c} \right) \right) \quad (5.1)$$

calculates the highest achievable  $STL$  at a special frequency  $f$  of an infinite wall with thickness  $d$  and density  $\rho_w$  surrounded by air and excited by a diffuse sound field. It can be seen that  $STL_{\max}$  increases with higher frequency of excitation, thickness and density of the wall. This means that an efficient sound insulation at low frequencies only can be achieved with a very thick and/or heavy wall. Figure 5.2 displays the calculated  $STL_{\max}$  at an exemplary chosen frequency below 300 Hz by using (5.1) as a function of the wall's

## 5. Absorbers for low frequencies

density. The upper limit of the sound transmission loss increases with increasing density and thickness.

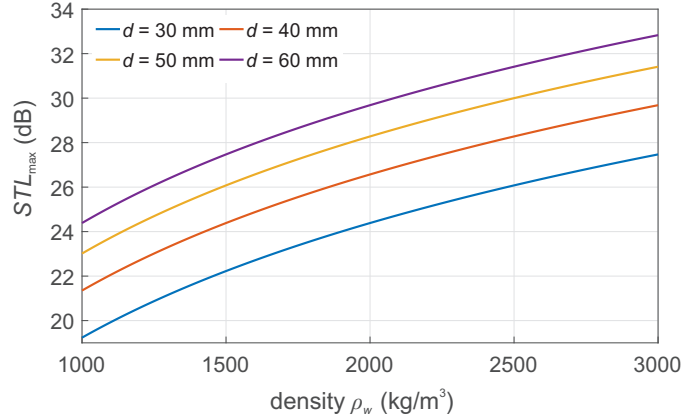


Figure 5.2.:  $STL_{\max}$  at an exemplary chosen frequency below 300 Hz calculated with (5.1) using different thicknesses of the wall as a function of its density.

However, it is well known that the encapsulation of a sound source emitting at low frequencies cannot be done in a traditional way by a light weight approach. In this chapter a mechanical narrow band acoustic absorber is introduced and the working principle is discussed. Furthermore, a characterization of a unit cell absorber is done including the characterization of an absorber array equipped with 120 absorber unit cells.

### 5.1. Working principle of the mechanical absorber

The mechanical absorber presented in this thesis is a passive absorber, which is independent of an external energy source and therefore very robust. In this section the working principle of the mechanical absorber is explained.

#### 5.1.1. Theory of a mass loaded plate

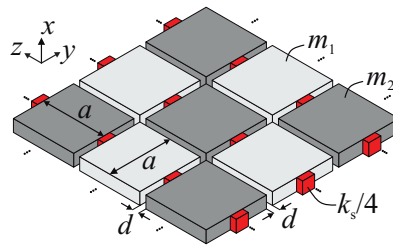


Figure 5.3.: Sketch of a mass loaded plate.

## 5. Absorbers for low frequencies

The idea is based on a mass loaded plate, which can be found in [64]. Here, the *STL* is increased above the mass law limit given by (5.1) at a narrow frequency range around a design frequency. In the following theoretical study, the mass loaded plate is assumed to be a checkerboard like array of two types of elements with equal size and top surface  $A = a^2$  but different masses per unit area  $m_1$  and  $m_2$  ( $m_1 > m_2$ ). A sketch of this mass loaded plate can be seen in fig. 5.3. The elements are coupled in  $z$ -direction to each other with springs of thickness  $d = 0$  and stiffness per unit area  $k_s/4$  only acting in  $x$ -direction perpendicular to the surface of the plates. The acoustic impedance (per Area  $A$ ) of the mass loaded plate can be calculated with [64]

$$Z = \frac{\frac{k_s}{j\omega} + j\omega m}{1 - \frac{k_s}{\omega^2 M}}. \quad (5.2)$$

In (5.2)

$$m = \frac{2m_1 m_2}{m_1 + m_2} \quad (5.3)$$

is the advanced mass ratio calculated by means of the masses  $m_1$  and  $m_2$ . Furthermore,

$$M = \frac{1}{2} (m_1 + m_2) \quad (5.4)$$

denotes the average mass per unit area  $A$ . The angular eigen frequency of the resulting system computes by

$$\omega_0 = \sqrt{k_s/M}. \quad (5.5)$$

An additionally damping can be introduced via a complex stiffness of the springs (damping parameter  $\eta$ ). The resulting increase of *STL* over the one given by the mass law can be determined with

$$\Delta STL = 20 \log \left| \frac{Z}{j\omega M} \right| = 10 \log \left( \frac{\left( \frac{m}{M} \frac{\omega^2}{\omega_0^2} - 1 \right)^2 + \eta^2}{\left( \frac{\omega^2}{\omega_0^2} - 1 \right)^2 + \eta^2} \right). \quad (5.6)$$

A detailed derivation of (5.6) can be found in [64]. In fig. 5.4 the additional *STL* gained by means of the mass loaded plate is shown as a function of frequency by using different mass ratios with and without damping. A maximum can be found in the undamped case at the eigen frequency  $\omega = \omega_0$ . In case of damping, the maximum is lower than in the undamped case and the maxima and minima are shifted in frequency. It can be seen that the frequency of the maximum is independent of the ratio  $m/M$ . It only depends on the stiffness and total mass of the plate as can be easily seen in (5.5). Moreover, a minimum can be found at frequencies  $\omega > \omega_0$ . The frequency, where the minimum can be found in the undamped case is  $\omega_0 \sqrt{M/m}$ . This minimum occurs at lower frequencies, the higher



## 5. Absorbers for low frequencies

$m/M$  is and therefore, the lower  $m_1/m_2$  is. At frequencies higher than  $\omega_0\sqrt{2/(\frac{m}{M} + 1)}$ , the  $\Delta STL$  can be found to be smaller than zero and therefore, the mass loaded plate works worse than a normal plate with the same mass. It can be observed that the peak of  $\Delta STL$  at the eigen frequency can be found lower, the lower the mass ratio  $m_1/m_2$  is. Furthermore, a lower ratio of masses  $m_1/m_2$  results in a higher  $\Delta STL$  at frequencies larger than  $\omega_0\sqrt{2/(\frac{m}{M} + 1)}$ . In consequence, the higher the peak of  $\Delta STL$  at the eigen frequency, the lower the  $\Delta STL$  at higher frequencies.

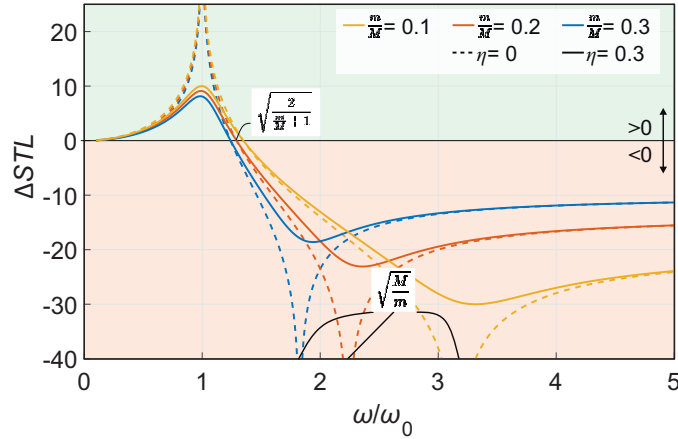


Figure 5.4.: Additional  $STL$  over  $STL_{\max}$  given by the mass law with and without damping and different mass ratios  $m/M = 0.1(m_1/m_2 \approx 38)$ ,  $m/M = 0.2(m_1/m_2 \approx 13.44)$ ,  $m/M = 0.3(m_1/m_2 \approx 11.2)$ .

From this simple model of the mass loaded plate, some design rules for a mechanical absorber can be derived. The peak of  $\Delta STL$  can be tuned by varying the stiffness and the total mass of the plate. In the implementation of the theory, a membrane is used as a stiffness and a steel plate is applied. Hence, the membrane represents  $k_s$ ,  $m_2$  and  $\eta$  whereas the steel plate can be modeled with  $m_1$ . The peak can be shifted in frequency without changing the zero crossing and the minimum of the curve by the application of an additional tension on the membrane. In many applications it is preferable to obtain a wide frequency range with a high  $STL$ . The zero crossing, where (5.6) gets negative, can be shifted to higher frequencies by decreasing the mass ratio  $m/M$ . In fig. 5.5 the frequency of the zero crossing as a function of the ratio  $m_1/m_2$  is shown. It can be seen that the frequency of zero crossing increases with higher ratio of masses  $m_1/m_2$ . The frequency of zero crossing is bounded by the minimum, when  $m_1 = m_2$  and by the maximum of  $\sqrt{2}\omega_0$ . Hence, for a broad increasing of the  $STL$  over the mass law, a large  $m_1$  and a small  $m_2$  is necessary. The reverse of the medal is that a large  $m_1$  and a small  $m_2$  will result in a small peak in  $\Delta STL$  and furthermore will cause a lower  $\Delta STL$  at higher frequencies.

## 5. Absorbers for low frequencies

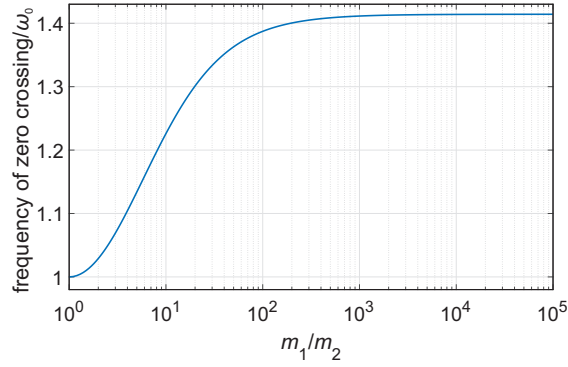


Figure 5.5.: The frequency of the zero crossing  $\sqrt{2/(\frac{m}{M} + 1)}/\omega_0$  as a function of the ratio  $m_1/m_2$ .

### 5.2. Unit cell absorber

As shown in the previous section, an additional *STL* can be gained in a frequency range around a design frequency  $f_0$  by applying the theory of the mass loaded plate. The mechanical absorber used in this thesis consists of a membrane and a steel plate with rectangular surface.

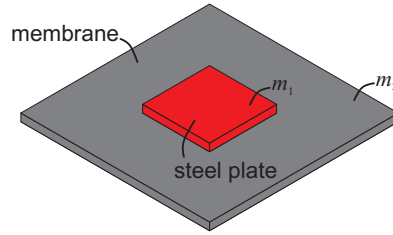


Figure 5.6.: Sketch of the mass loaded membrane made of a membrane and a steel plate with mass  $m_1$  and  $m_2$ .

In fig. 5.6 a sketch of the mechanical absorber is displayed. It consists of a rectangular membrane and a steel plate. Therefore, the absorber consists of two masses ( $m_1$ ,  $m_2$ ) connected by an stiffness provided by the membrane. Hence, it can roughly be modeled with a two degree of freedom (DOF) system. This is a major difference to the model of the mass loaded plate, since the characteristic frequency (peak of additional *STL*) is modeled with the stiffness and the total mass of the mechanical system. Furthermore, the model of the mass loaded plate only represents the opposite displacement of the membrane and the mass at a certain frequency. In 2 DOF systems, two resonance frequencies can be found, where the amplitudes of one DOF are maximal. Between the two resonance frequencies, there occurs an anti resonance along with a minimum of amplitude of one degree of freedom and a large phase shift between the two degree of freedoms. In acoustics, small amplitudes result in a small sound radiation and additionally a phase

## 5. Absorbers for low frequencies

shift will produce an acoustic short circuit with minimal acoustic energy radiation. Thus, the concept of a mass loaded membrane appears to be suitable to be a good absorber. In fig. 5.7 different designs of such previously described mass loaded membranes can be seen. The steel frame is 4 mm thick and 10 mm deep. The thickness of the steel plate and the ethylene propylene diene monomer (EPDM) membrane is 4 mm, whereas the dimensions of the membranes, attached on the steel frames, are 108 mm x 108 mm (I and II) and 100 mm x 100 mm (III). The steel plate is 35.5 mm x 35.5 mm. In I and II the membrane is fixed on top of the steel frame, while the membrane in III is mounted in the steel frame. In all cases the free oscillating membrane is 100 mm x 100 mm, whereas III should show a higher resonance frequency since the mechanical fixation is stiffer.

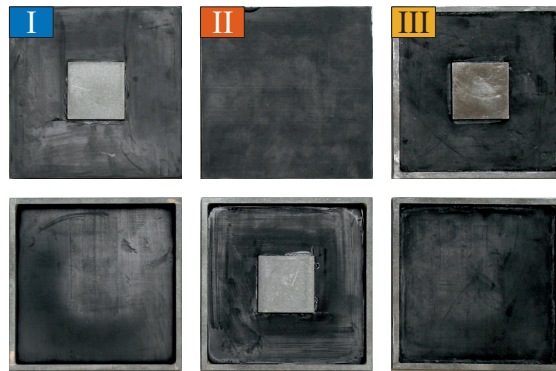


Figure 5.7.: Front and back side of different mass loaded membranes designs. I: Membrane mounted on the steel frame, steel plate on front side. II: Membrane mounted on the steel frame, steel plate on backside. III: Membrane mounted in the steel frame, steel plate on front side.

### 5.2.1. Measurement setups for characterization

In the following section the measurement setups for the characterization of the mass loaded membrane are described. The measurement setups are discussed for studying the working principle by means of an acoustic tube characterization and by investigation of the surface displacement using a laser scanning vibrometer.

#### Transmission loss tube

For the characterization of the mass loaded membrane, a transmission loss tube for square samples is developed. The measurement setup is based on the transfer matrix method described in [9]. With this method the transfer matrix and thus several acoustic properties, e.g. the  $STL$  of a sample can be determined. In fig. 5.8 the measurement setup can be seen. The transmission loss tube is a set of two tubes that can be connected to either end of a sample. The tubes are made of aluminum with a cross section of 100 mm x 100 mm. A loudspeaker is mounted on the one end of a tube. In this measurement setup, a Visaton FX10 is used as a sound source and excited by a broadband

## 5. Absorbers for low frequencies

acoustic signal, e.g. white noise, whereas the acoustic pressure is recorded by using 1/4" condenser microphones BK 4187. The measurement tube allows plane wave propagation up to the tube's cut off frequency of 1725 Hz.

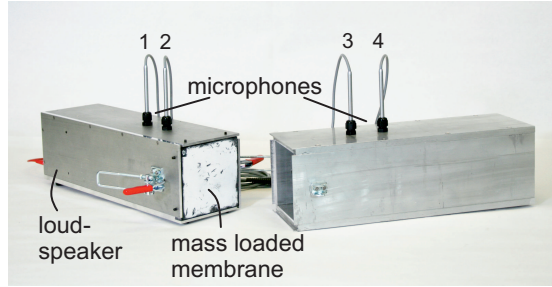


Figure 5.8.: Transmission loss tube for rectangular samples.

The acoustic pressure inside the tube is measured at four positions, as can be seen in fig. 5.9. Two microphones (1,2) are placed at  $x_1$  and  $x_2$  between the sound source and the sample. The sample with thickness  $d$  is located in the origin. Downstream the sample, there are two further microphones (3,4) at  $x_3$  and  $x_4$ . The acoustic pressure upstream and downstream of the sample is a superposition of a positive- and negative-directed plane wave  $A, B$  and  $C, D$ , respectively.

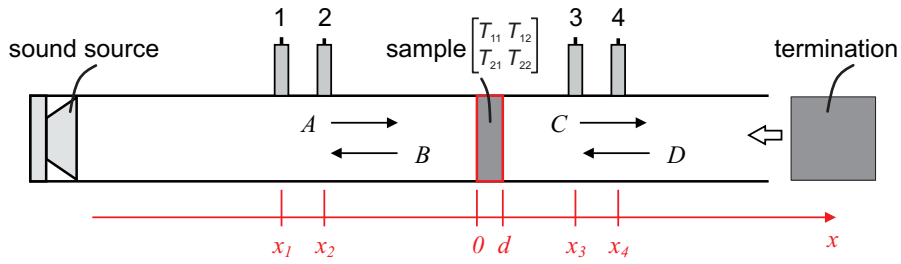


Figure 5.9.: Schematic of the transmission loss tube.

If two measurements (superscript  $(a)$  and  $(b)$ ) with two acoustic terminations are performed, the system of equations

$$\begin{bmatrix} p^{(a)} & p^{(b)} \\ v^{(a)} & v^{(b)} \end{bmatrix}_{x=0} = \begin{bmatrix} T_{11} & T_{12} \\ T_{21} & T_{22} \end{bmatrix} \begin{bmatrix} p^{(a)} & p^{(b)} \\ v^{(a)} & v^{(b)} \end{bmatrix}_{x=d} \quad (5.7)$$

can be solved for the transfer matrix

$$\begin{bmatrix} T_{11} & T_{12} \\ T_{21} & T_{22} \end{bmatrix} = \frac{1}{p_{x=d}^{(a)} v_{x=d}^{(b)} - p_{x=d}^{(b)} v_{x=d}^{(a)}} \begin{bmatrix} p_{x=0}^{(a)} v_{x=d}^{(b)} - p_{x=0}^{(b)} v_{x=d}^{(a)} & -p_{x=0}^{(a)} p_{x=d}^{(b)} + p_{x=0}^{(b)} p_{x=d}^{(a)} \\ v_{x=0}^{(a)} v_{x=d}^{(b)} - v_{x=0}^{(b)} v_{x=d}^{(a)} & -p_{x=d}^{(b)} v_{x=0}^{(a)} + p_{x=d}^{(a)} v_{x=0}^{(b)} \end{bmatrix}. \quad (5.8)$$

## 5. Absorbers for low frequencies

In (5.7) and (5.8)  $p^{(a/b)}$  is the acoustic pressure and  $v^{(a/b)}$  is the particle velocity from both measurements. Since the acoustic pressure and acoustic particle velocity are only measured at  $x_{1...4}$ , the quantities at  $x = d$  and in the origin has to be computed by using the plane wave theory. For a detailed derivation, the reader is referred to [9]. The sound transmission loss computes from the four entries of the transfer matrix by

$$STL = 10 \log \left( \frac{1}{4} |T_{11} + T_{12}/(\rho c) + \rho c T_{21} T_{22}|^2 \right). \quad (5.9)$$

### Surface displacement measurement setup

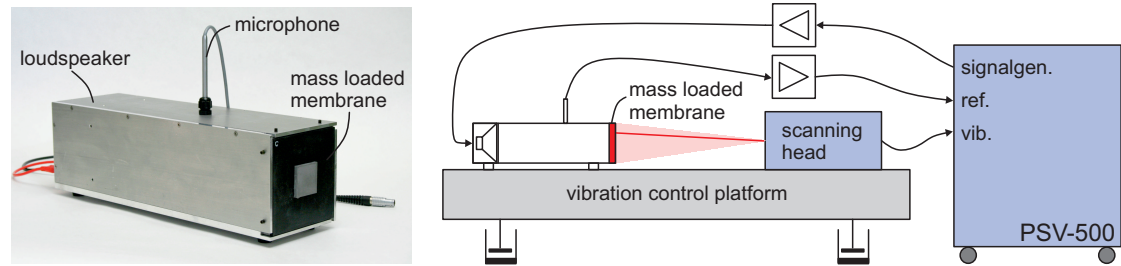


Figure 5.10.: Measurement setup to identify the surface displacement of the mass loaded membrane. Left: Tube consisting of a loudspeaker, a sound pressure microphone with an exemplary mass loaded membrane. Right: Schematic of the measurement setup.

For studying the working principle, additionally the surface displacement of the membrane is measured with a laser scanning vibrometer Polytec PSV-500. For this purpose, the measurement setup depicted in fig. 5.10 is used and the surface velocity measured by means of the vibrometer is integrated over time to obtain the displacement. In this measurement setup the mass loaded membrane is excited by plane waves produced by a Visaton FX10 using the sweep function of the signal generator. The measurement setup is mounted on top of a vibration controlled platform to avoid disturbances due to environmental vibrations. The acoustic pressure inside the tube is measured by means of a BK 4187 as can be seen in fig. 5.11 and is used as a reference signal. Up to 300 Hz, there can be noticed a nearly constant behavior of the sound pressure level as a function of frequency and a sound pressure level between 67 dB and 72 dB. The acoustic pressure is minimum, when the first longitudinal mode occurs in the tube. This can be observed at frequencies around 600 Hz, whereby the curve is shifted to higher frequencies the less the distance between loudspeaker and membrane is. However, this acoustic pressure is used as a reference and is in the same order of magnitude in the frequency of interest below 300 Hz, since the mechanical absorber is designed to absorb acoustic energy in a narrow band frequency range below 300 Hz.

## 5. Absorbers for low frequencies

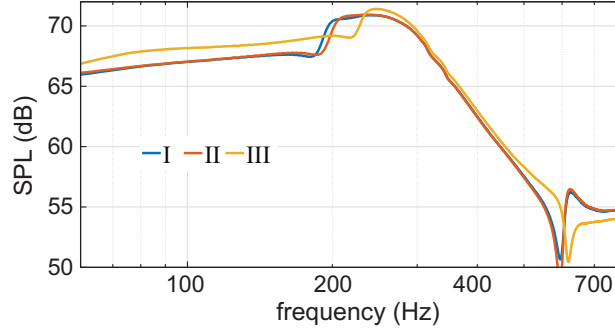


Figure 5.11.: Measured sound pressure level (rel. to  $20 \mu\text{Pa}$ ) in the tube depicted in the left part of fig. 5.10 equipped with different samples shown in fig. 5.7.

### 5.2.2. Characterization of the unit cell absorber

In this section, the mechanical absorber is characterized. Hereby, the characterization is done regarding the application source emitting a mono frequent noise by means of the measurement setups presented in the previous section.

The determination of the surface displacement distribution of the membranes mounted in the tube is realized at 441 measurement points on a regular grid with a 4.8 mm discretization increment. In fig. 5.12 the averaged amplitudes of the displacement relative to the pressure amplitude in the tube is shown. The curves all show a peak at  $f_0 + 500 \text{ Hz}$  due to the longitudinal mode in the tube and the associated minimum in the pressure amplitude. Furthermore, two peaks in the curves can be observed at nearly  $f_0 - 60 \text{ Hz}$  and  $f_0 + 100 \text{ Hz}$ . This indicates resonant behavior. Between the two maxima, there can be found a frequency range with minimum of amplitude, which suggests an anti resonance here.

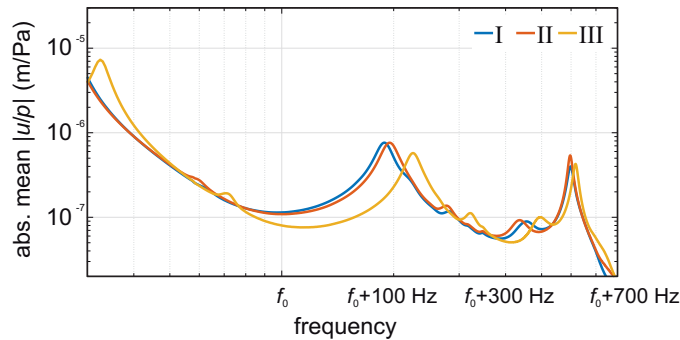


Figure 5.12.: Average of the amplitudes of the displacement at the 441 measurement points relative to the sound pressure in the tube  $1/441 \sum_{i=1}^{441} |u_i| / |p|$ .

The displaced volume of air above the mass loaded membrane's surface  $\Gamma$  computes to

## 5. Absorbers for low frequencies

$$V_{\text{dis}} = \int \mathbf{u} \cdot \boldsymbol{\Gamma}. \quad (5.10)$$

In (5.10)  $\mathbf{u}$  is the displacement vector. In case of an acoustic short circuit, the displaced volume is minimum. The complex average of the displacement is a measure for the displaced volume of air above the membrane. In fig. 5.13 the complex average of the displacement relative to the excitation pressure is shown. Again, the peak at  $f_0 + 500$  Hz due to the longitudinal mode in the tube can be observed. Moreover, the curve shows maximums again at  $f_0 - 60$  Hz and  $f_0 + 500$  Hz. An obvious minimum can be found at the frequency of anti resonance. In this frequency range the displacement of the membrane and additional weight is phase shifted. This means that the mass loaded membrane produces an acoustic short circuit in front of the absorber.

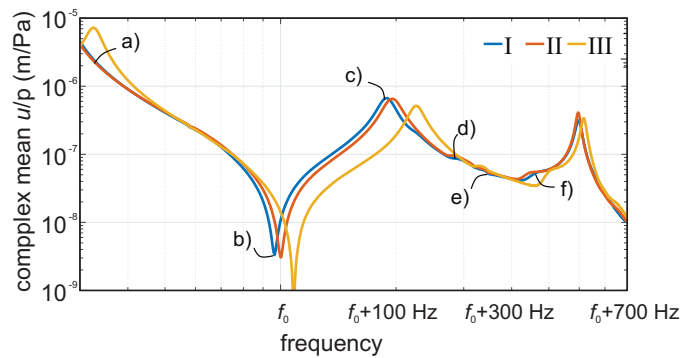


Figure 5.13.: Complex average of the displacement at the 441 measurement points relative to the sound pressure in the tube  $1/441 \left| \sum_{i=1}^{441} u_i/p \right|$ . The letters denote distinctive frequencies. a)  $f_0 - 60$  Hz, b)  $f_0$ , c)  $f_0 + 89$  Hz, d)  $f_0 + 185$  Hz, e)  $f_0 + 242$  Hz, f)  $f_0 + 382$  Hz.

In fig. 5.14, the displacement distribution of the surface of mass loaded membrane II relative to the sound pressure in the tube can be seen. In the top row, the amplitude normalized by the maximum of the surface's displacement amplitude at the six distinctive frequencies, shown in fig. 5.13 a) – f), can be seen. The bottom row shows the phase of the displacement. It can be observed that the displacement distribution at  $f_0 - 60$  Hz and  $f_0$  is dominated by displacement of the steel plate, whereas the mass nearly does not move at higher frequencies. At  $f_0 - 60$  Hz, the mass loaded membrane is in phase across the cross surface. At  $f_0$  and  $f_0 + 89$  Hz, the steel plate and the surrounding membrane are out of phase, whereby the phase shift is  $180^\circ$  ( $f_0$ ) and  $160^\circ$  ( $f_0 + 89$  Hz). In case of this both distinctive frequencies, the amplitude in the corner of the membrane is dominant. At higher frequencies higher order of vibration modes can be found. At  $f_0 + 185$  Hz and  $f_0 + 382$  Hz the membrane shows eight peaks across the surface, whereas the displacement peaks at  $f_0 + 382$  Hz are in phase and at  $f_0 + 185$  Hz there can be found

## 5. Absorbers for low frequencies

a phase shift of  $90^\circ$ . Finally a loop structure of the vibration mode can be found at  $f_0 + 242$  Hz.

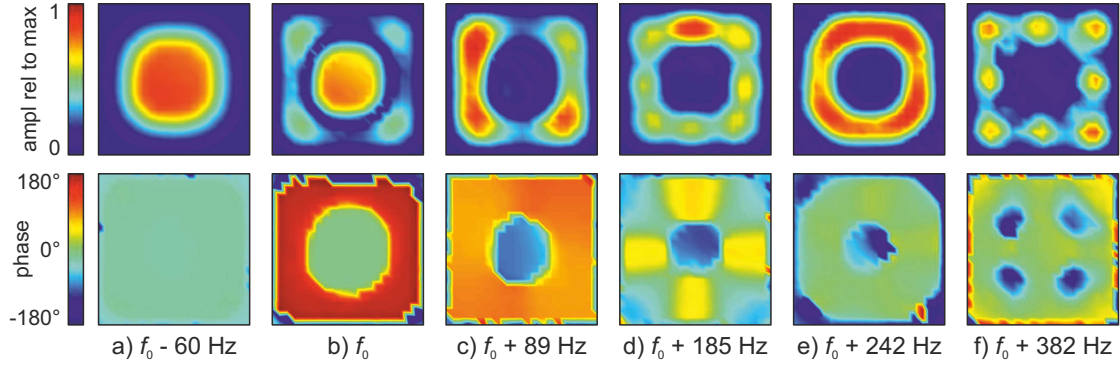


Figure 5.14.: Distribution of the displacement amplitude and phase of mass loaded membrane II relative to the pressure in the tube at distinctive frequencies shown in fig. 5.13. The amplitude is shown relative to the maximum on the surface.

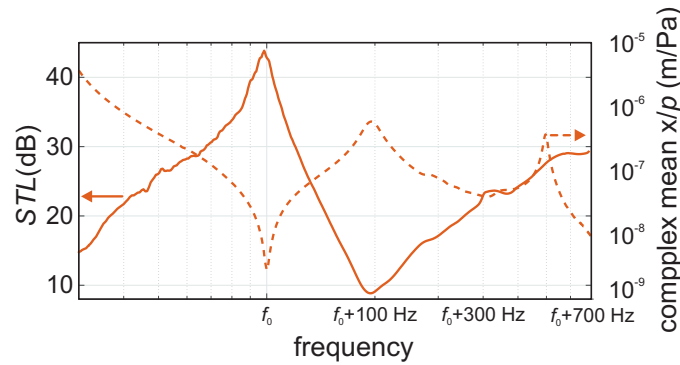


Figure 5.15.: Complex average of the displacement according to fig. 5.13 and sound transmission loss of the mass loaded membrane II measured with the transmission loss tube as a function of frequency.

The resulting sound transmission loss of mass loaded membrane II measured by means of the transmission loss tube can be seen in fig. 5.15. The curve of  $STL$  is compared to the complex averaged displacement amplitude from the previous plots. It can be observed that the  $STL$  increases with larger frequencies and reaches the maximum value at  $f_0 - 0.5$  Hz with 43.84 dB. With further increase of frequency, the  $STL$  drops and shows a minimum at  $f_0 + 88.5$  Hz. As predicted, the peak in  $STL$  corresponds to the dip in the complex average of the displacement amplitude. This means that the mass loaded membrane produces an acoustic short circuit, which results in a minimal acoustic energy radiation. Moreover, the dip in  $STL$  can be found, where the complex averaged displacement amplitude shows a maximum and the membrane moves like a loudspeaker



## 5. Absorbers for low frequencies

with a displacement over the cross section in phase, see fig. 5.14. A small peak in *STL* can be found at frequencies around  $f_0 + 185$  Hz, where the steel plate is at rest, but the membrane shows eight displacement hot spots, whereby the neighbor hot spots are out of phase with a phase shift of approximately  $90^\circ$ . In the frequency range about  $f_0 + 382$  Hz an additional minor drop in the *STL* can be observed due to the displacement of the membrane, showing eight in phase hot spots of displacement.

### 5.3. Array absorber

The absorber array is composed of 120 mass loaded membranes. These are arranged in 20 rows consisting of six mass loaded membranes mounted on a rigid steel frame. The steel frame with dimensions 648 mm x 2104 mm is 4 mm thick and 80 mm deep. The difference in the structure in comparison to the mass loaded membrane described in Sec. 5.2 is only the depth of the steel frame. In fig. 5.16 the absorber array can be seen. The array is clamped into the measurement setup at 20 locations, four in every edge of the array and two in the center of the long sides each. Moreover, the 10 mm wide gap between the array and the measurement setup can be sealed with silicone. If so, it was made sure that the depth of the sealing is approximately 10 mm.



Figure 5.16.: Absorber array consisting of 120 mass loaded membranes on a 80 mm deep rigid steel frame.

### 5.3.1. Measurement setup for array characterization

To characterize an array of mass loaded membranes, a special measurement setup is needed. Hence, for the identification of the  $IL$  of an array of mass loaded membranes, the substitution principle is applied. This means, the acoustic power is determined in a measurement setup with and without the array by using (2.23). With the assumption that the acoustic energy emitted by the source is the same in both configurations, the difference in acoustic power can be identified as the  $IL$  of the array.

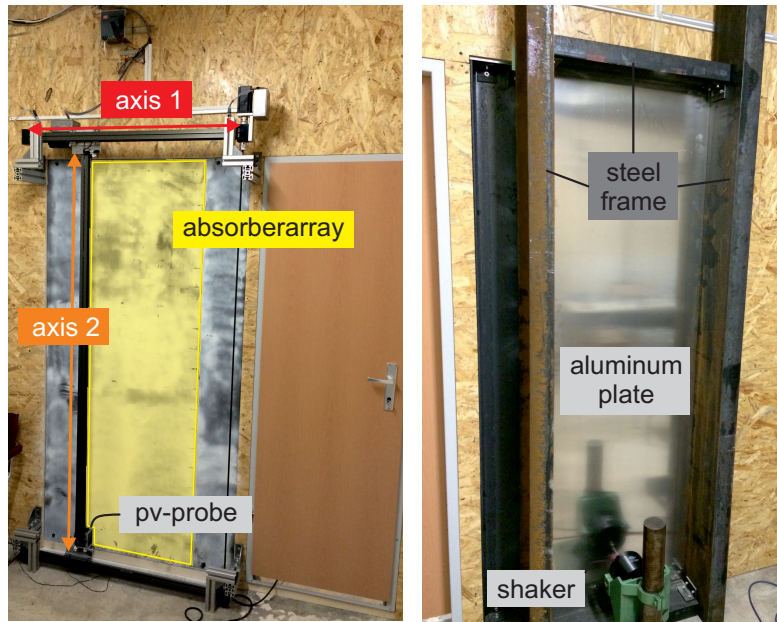


Figure 5.17.: Measurement setup for the characterization of the array of mass loaded membranes. Left: Frontside with 2D scanning gantry and a pv-probe. Right: Backside with excitation plate made of aluminum in a steel frame driven by an electrodynamic vibration exciter.

In fig. 5.17 the measurement setup to characterize the array of mass loaded membranes is shown. The measurement setup is excited by means of a vibrating aluminum plate with thickness 4 mm and dimensions 654 mm x 2112 mm. The plate again is excited at a chosen frequency  $f_0$  by an external mechanical source (electrodynamic shaker BK 4809) on an antinode of vibration at a position 216.4 mm from the lower edge. In a possible application of the array, we assume a mono frequent noise source with an excitation being not homogeneous across the profile, but is dominated by the mode of oscillation showing 5 vertical antinodes. Thus, the aluminum plate for the excitation of the measurement setup is adjusted to show the 1–5 mode nearby the excitation frequency  $f_0$ . This adjustment is done via FEM-modal analysis and can be found at  $f_0 + 3.73\text{ Hz}$  in the simulation and at  $f_0 + 0.5\text{ Hz}$  in the experimental modal analysis. However, the aluminum plate is excited in an antinode, whereas the mechanical energy flow is measured by means

## 5. Absorbers for low frequencies

of an impedance head BK 8001. The resulting surface displacement distribution of the vibrating plate, measured with the laser scanning vibrometer PSV-500, can be seen in fig. 5.18. Here, the real part of the surface displacement is shown qualitatively in the left part. Furthermore, the displacement amplitude and phase relative to the excitation force is displayed in the right part. It clearly can be detected that the vibration shape is dominated by the 1–5 mode with five antinodes having the same amplitude and a phase shift of  $180^\circ$ . Additionally, the six nodes can be observed.

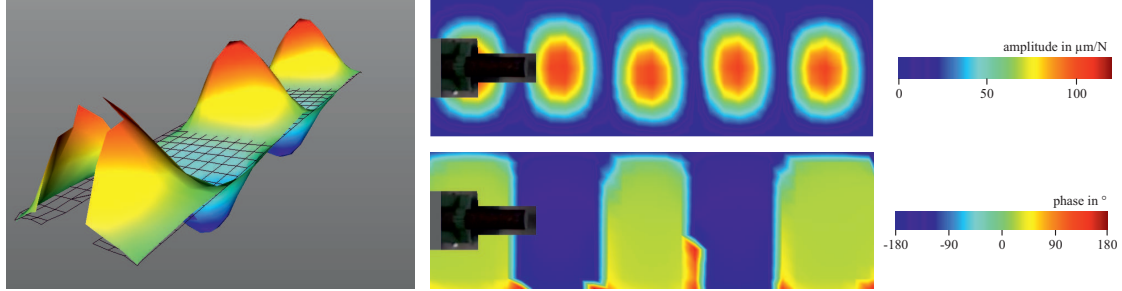


Figure 5.18.: Displacement distribution of the aluminum plate by means of an excitation at a chosen frequency. Left: real part of the surface displacement. Right: amplitude and phase relative to the excitation force.

In the measurement setup, there is the possibility to mount a sample with dimensions up to 648 mm x 2104 mm. On the front side of the measurement setup, where the absorber array is mounted, a pv-probe Microflown USP is installed on a 2D scanning gantry. In this way, the acoustic power can be determined on a reference plane by using (2.19) and (2.20). In the following, the reference plane will be located 27 mm in front of the array or 142 mm in front of the excitation plate, respectively. Assuming that the acoustic power emitted from the excitation plate is always constant, no matter, if a device under test is mounted in the measurement setup, the insertion loss of the array can be derived. Furthermore, we assume the acoustic energy leaving the measurement setup through the lateral gap of 27 mm to be the same in both measurements and additionally small enough to be neglected.

### 5.3.2. Characterization of the absorber array

In the following, the results of the intensity measurements on the reference plane 27 mm in front of the array are presented. The determination of the acoustic sound power was done with a spatial resolution of 6.5 mm in each of the two directions by means of nearly 30,000 measurement points employing the Microflown USP. The pv-probe is calibrated by applying the calibration method described in Sec. 3 to avoid errors obtaining the acoustic intensity due to phase mismatch according to (3.1). The identified acoustic intensity at each of the measurement points is recorded in relation to the square of the acceleration amplitude at the excitation to take a possible fluctuation in the excitation amplitude into account. In tab. 5.1 the determined acoustic power in relation to the

## 5. Absorbers for low frequencies

Table 5.1.: Acoustic power at 100 Hz measured at the reference plane relative to the excitation acceleration in  $\text{nW}/(\text{m}^2/\text{s}^4)$  with the confidence limits of 95%.

Measurement	Reference (without array)	Array with air gap	Array with silicone
1	1187.27	193.21	-1.02
2	1185.55	184.72	1.19
3	1236.41	191.89	-0.34
Average	$1203,08 \pm 58.48$	$189.97 \pm 9.25$	$-0.06 \pm 2.29$

excitation acceleration amplitude is listed. Here, the mean value of the measurement results with the confidence limits of 95% show that the acoustic power can be reduced due to the application of the absorber array. By means of the array with a surrounding air gap of 10 mm the  $IL$  can be identified to be 8.02 dB. Obviously, the acoustic energy flows in the air gap and results in an  $IL$  of the array, which does not exploit the full potential of the mass loaded membrane. In case of a sealed air gap, the acoustic power on the measurement plane is so small that the confidence level is larger than the measured value, since the acoustic energy transmitted through the array is tiny. However, taking the lower and upper confidence bounds of the measurement with the array sealed with silicone for the calculation of the  $IL$  with (2.23), the  $IL$  of the sealed array of absorber can be determined with at least 27.24 dB.

In fig. 5.19, the surface velocity distribution of the array of the 120 mass loaded membranes is shown. It can be seen that the array is only excited efficiently at eleven rows out of 20. The highest amplitude of surface velocity can be observed in the four top lines, two in the center and five on the bottom. The surface velocity of one mass loaded membrane was cutted out, since there the steel plate disappeared, which causes high amplitudes in this region of the array. However, nine out of 20 rows of mass loaded membranes show a very low velocity amplitude. Hence, the difference between a single mass loaded membrane with almost 45 dB and an array with 27.24 dB in terms of  $STL$  and  $IL$ , respectively, can be explained.

5. Absorbers for low frequencies

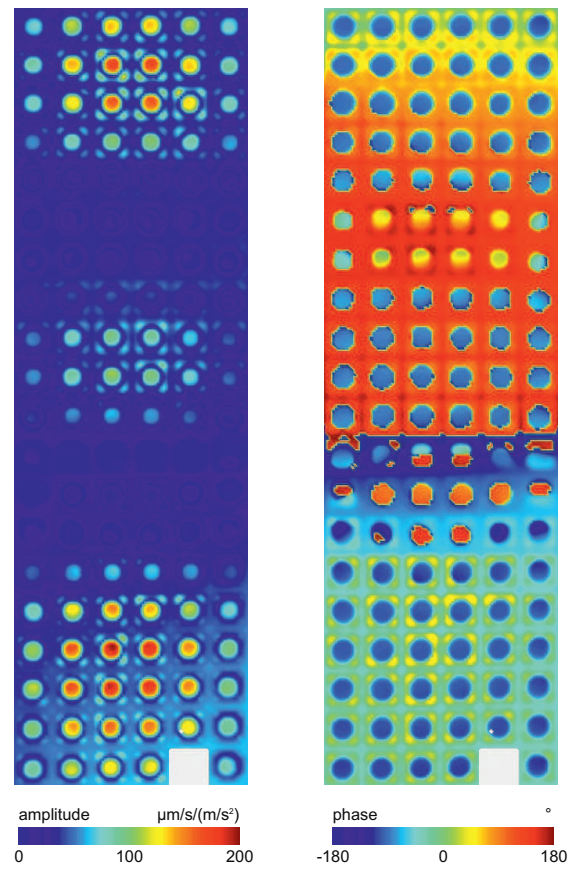


Figure 5.19.: Surface velocity (amplitude and phase) of the array of mass loaded membranes sealed with silicone relative to the excitation acceleration.

## 6. Conclusion

The objective of this thesis is the characterization of acoustic absorbers to provide realistic boundary conditions for the simulation of a real sound field. If the surface under investigation is locally reactive, the measurement of the acoustic surface properties is an easy task since the quantities do not depend on the angle of sound incidence. Thus, at perpendicular sound incidence these acoustic surface properties can be obtained by applying standard methods. The characterization of the acoustic properties in case of a non-locally reactive surface requires more effort during the measurement process. Here, the acoustic surface properties have to be determined not only as a function of the frequency of excitation but also as a function of the angle of sound incidence. In this thesis two measurement methods to obtain the acoustic surface properties at oblique angles of sound incidence are implemented and characterized. Through accurate identification and characterization of advantages and disadvantages of both methods, the measuring of the acoustic surface properties was profoundly improved. For validation purposes, the measurement results in terms of the sound pressure reflection coefficient are compared with two different methods. On the one side, results were compared by means of standard test methods for perpendicular sound incidence and on the other side by means of theoretical values. The reference values are calculated by modeling the acoustic absorbers with a fluid by using effective material parameters. In particular the implemented spatial Fourier transform method, using a sound source showing a directional polar pattern, turned out to be a very robust tool for the characterization of a surface in terms of its acoustic properties at oblique angles of incidence. An inherent weakness of this method can be noticed at perpendicular sound incidence. This weakness can either be overcome by using the standard test methods for perpendicular angle of sound incidence or by applying a method based on an equivalent source [135] that can be derived by utilizing the recorded data at the two measurement lines. In conclusion it can be said that while the subtraction method also allows for the precise investigation of the acoustic properties of a surface, it remains the inferior method in the implemented state. Further improvements regarding an automated measurement process for a great number of angles of sound incidence are recommended here. However, the measurement results of both implementations overall match the reference values, if the properties are compared in terms of absolute values. Only the result obtained by the spatial Fourier transform method shows prominent congruence to the reference. The results coincide in terms of the real and imaginary part of the sound pressure reflection coefficient over a wide frequency bandwidth and a large range of angles of sound incidence. However, these obtained acoustic surface properties can now be used as realistic boundary conditions in the simulation of real sound fields.

Traditional absorber materials such as porous or fibrous materials show a drop in the

## 6. Conclusion

absorption capability towards low frequencies. To address this shortcoming, a mechanical absorber for low frequencies below 300 Hz, using a mass attached on a membrane, was developed and fully characterized in this thesis. The mass loaded membrane can be applied to efficiently absorb acoustic energy in a narrow frequency band and does so significantly better than predicted by the mass law. In the characterization it has been shown that the developed mechanical absorber produces an acoustic short circuit which results in a high sound transmission loss of the mass loaded membrane. Hence, by using this kind of absorber at the low frequency range, where traditional absorber materials do not absorb acoustic energy efficiently, a robust and passive approach has been found. Even the application of the mass loaded membrane in an absorber array has been shown to provide an insertion loss higher than the conventional method of insulating sound sources emitting noise at low frequencies with a heavy mass. The developed absorber array provides not only a higher insertion loss but is also better in terms of lightweight design.

For the characterization of the mass loaded membrane, a particle velocity sensor was used during acoustic intensity measurements. Since the sound field produced by the developed absorber is dominated by a reactive part of the intensity in the near field, the calibration of the intensity probe and thus of the particle velocity sensor is of great importance. In this thesis a direct calibration method is developed by employing a reference sound field produced with a vibrating piston and fully characterized by calculating the acoustic field using the finite element method. Since the orientation of the sensor can be determined by means of the local gravity field, the three components of the 3D particle velocity sensor can be calibrated simultaneously. The novel calibration method is implemented and fully characterized by measurements and simulations. Furthermore, the calibration of the 3D particle velocity sensor was conducted, in order to reduce the error due to phase mismatch during the intensity measurements in the characterization of the mass loaded membrane. The obtained sensitivities show a clear discrepancy in comparison to the sensitivities given by the manufacturer, in particular in the frequency range between 100 Hz and 1 kHz. The identified results of the calibration were confirmed by a validation measurement setup to represent the real sensitivities of the particle velocity sensor.

# A. Appendix

## A.1. Modeling of the characteristic field impedance

The characteristic field impedance of a fluid with a flow resistivity  $\sigma$

$$Z'_C = Z_0 [1 + a_1(f/\sigma)^{a_2} - ja_3(f/\sigma)^{a_4}] \quad (\text{A.1})$$

and the wave number

$$k' = \frac{\omega}{c} [1 + a_7(f/\sigma)^{a_8} - ja_5(f/\sigma)^{a_6}] \quad (\text{A.2})$$

can be modeled by using the Delany–Bazley model [39] or the Miki model [85]. The coefficients in the different models can be found in tab. A.1.

Table A.1.: Coefficients in the empirical models [61].

Coefficient	Delany–Bazley	Miki
$a_1$	0.0497	0.0699
$a_2$	-0.754	-0.632
$a_3$	0.0758	0.107
$a_4$	-0.732	-0.632
$a_5$	0.169	0.160
$a_6$	-0.595	-0.618
$a_7$	0.0858	0.109
$a_8$	-0.700	-0.618

Employing the Komatsu–model, the characteristic field impedance is obtained with

$$Z'_C = Z_0 \left[ 1 + 0.00027(2 - \log(f/\sigma))^{6.2} - j0.0047(2 - \log(f/\sigma))^{4.1} \right], \quad (\text{A.3})$$

whereas the wave number is calculated with

$$k' = \frac{\omega}{c} \left[ 1 + 0.0004(2 - \log(f/\sigma))^{6.2} - j0.0069(2 - \log(f/\sigma))^{4.1} \right]. \quad (\text{A.4})$$

## A.2. Derivation of Spatial Fourier transform formulations

### A.2.1. Monopole

In [104], the free field Green's function of a monopole is given by

$$H_{\text{MP}}^+ = \frac{1}{4\pi r_d} e^{jkr_d} = \frac{j}{4\pi} \int_0^\infty J_0(r\mu) e^{j\sqrt{k^2 - \mu^2}|z_o - z_s|} \frac{\mu}{\sqrt{k^2 - \mu^2}} d\mu, \quad (\text{A.5})$$



## A. Appendix

with an arbitrary variable  $\mu$  and  $r_d = \sqrt{r^2 + (z_o - z_s)^2}$ . Using

$$\begin{aligned}\mu &= k_r, \\ \sqrt{k^2 - k_r^2} &= k_z,\end{aligned}$$

yields

$$\frac{1}{4\pi r_d} e^{jk r_d} = \frac{j}{4\pi} \int_0^\infty J_0(r k_r) e^{jk_z |z_o - z_s|} \frac{k_r}{k_z} dk_r. \quad (\text{A.6})$$

In comparison to the inverse Fourier transform in (2.46), the spatial Fourier transformed Green's function computes by

$$\tilde{H}_{\text{MP}}^+(k_r) = \frac{j}{2k_z} e^{jk_z |z_o - z_s|}. \quad (\text{A.7})$$

The conjugate complex of (A.6) can be rewritten with

$$\begin{aligned}(H_{\text{MP}}^+)^* &= H_{\text{MP}}^- = \frac{1}{4\pi r_d} e^{-jk r_d} \\ &= \left( \frac{j}{4\pi} \int_0^\infty J_0(r k_r) e^{jk_z |z_o - z_s|} \frac{k_r}{k_z} dk_r \right)^*\end{aligned} \quad (\text{A.8})$$

and therefore the spatial Fourier transformed Green's function of  $H_{\text{MP}}^-$  can be calculated by

$$\tilde{H}_{\text{MP}}^-(k_r) = \left( \frac{j}{2k_z} e^{jk_z |z_o - z_s|} \right)^*. \quad (\text{A.9})$$

It is obvious that the derivation of (A.9) requires a real-valued  $J_0(r k_r)$ . This is ensured, since the argument  $r k_r$  of the Bessel function is real-valued.

### A.2.2. Dipole

The acoustic pressure field excited by a dipole sound source can be calculated by [104]

$$P_a = j\omega\rho_0\hat{Q}d\frac{\partial}{\partial z_s} \left( \frac{1}{4\pi r_d} e^{-jk r_d} \right) = j\omega\rho_0\hat{Q}d\frac{\partial}{\partial z_s} (H_{\text{MP}}^-). \quad (\text{A.10})$$

Applying a derivative in respect to  $z_s$  to (A.8), the spatial Fourier transform of the acoustic pressure field excited by a dipole computes to

$$\tilde{P}_a = j\omega\rho_0\hat{Q}d\frac{\partial}{\partial z_s} \left[ \left( \frac{j}{2k_z} e^{jk_z |z_o - z_s|} \right)^* \right]. \quad (\text{A.11})$$

With an observer satisfying  $z_o \leq z_s$ , the pressure field in (A.11) can be expressed with

$$\tilde{P}_a = \frac{j\omega\rho_0\hat{Q}d}{2} [j \sin(k_z(z_s - z_o)) - \cos(k_z(z_s - z_o))]. \quad (\text{A.12})$$

### A.3. Derivation of the sound field above an acoustic interface

The acoustic pressure at an observer  $\mathbf{x}_0$  in a sound field excited by a sound source placed at  $\mathbf{x}_s$  can be split up into a direct and a reflected part

$$P_a(z_o) = P_{a,\text{dir}}(z_o) + P_{a,\text{r}}(z_o) \quad (\text{A.13})$$

$$= P_{a,\text{dir}}(z_o) + \frac{1}{2\pi} \int_0^\infty \tilde{P}_{a,\text{r}}(z_o) J_0(rk_r) k_r dk_r, \quad (\text{A.14})$$

whereas the reflected part can be calculated via the inverse spatial Fourier transform. The spatial Fourier transformed reflected part in (A.14) can be expressed by

$$\begin{aligned} \tilde{P}_{a,\text{r}}(z_o) &= \tilde{P}_{a,\text{r}}(0) e^{-jk_z z_o} \\ &= \tilde{P}_{a,\text{dir}}(0) \tilde{R} e^{-jk_z z_o} \\ &= \tilde{P}_{a,\text{dir}}(z_s) \tilde{R} e^{-jk_z z_o} e^{-jk_z z_s} \\ &= \tilde{P}_{a,\text{dir}}(z_s) \tilde{R} e^{-jk_z(z_s+z_o)}. \end{aligned} \quad (\text{A.15})$$

Inserting (A.15) into (A.14) yields

$$P_a(z_o) = P_{a,\text{dir}}(z_o) + \frac{1}{2\pi} \int_0^\infty \tilde{P}_{a,\text{dir}}(z_s) \tilde{R} e^{-jk_z(z_s+z_o)} J_0(rk_r) k_r dk_r \quad (\text{A.16})$$

## Bibliography

- [1] Iso 9614-1: Acoustics - determination of sound power levels of noise sources using sound intensity - part 1: Measurement at discrete points. ISO, 1993.
- [2] Iso 9614-2: Acoustics - determination of sound power levels of noise sources using sound intensity - part 2: Measurement by scanning. ISO, 1996.
- [3] Iso 10534-1: Acoustics - determination of sound absorption coefficient and impedance in impedance tubes - part 1: Method using standing wave ratio. ISO, 2001.
- [4] Iso 10534-2: Acoustics - determination of sound absorption coefficient and impedance in impedance tubes - part 2: Transfer-function method. ISO, 2001.
- [5] Iso 1793-5: Road traffic noise reducing devices - test method for determining the acoustic performance - part 5: Intrinsic characteristics - in situ values of sound reflection under direct sound field conditions. ISO, 2002.
- [6] Iso 354: Acoustics - measurement of sound absorption in a reverberation room. ISO, 2003.
- [7] Iso 17497-1: Acoustics - sound-scattering properties of surface - part 1: Measurement of the random-incidence scattering coefficient in a reverberation room. ISO, 2004.
- [8] Astm c423: Acoustics - standard test method for sound absorption and sound absorption coefficient by the reverberation room method. ASTM, 2009.
- [9] Astm e2611-09: Standard test method for measurement of normal incidence sound transmission of acoustical materials based on the transfer matrix method. ASTM, 2009.
- [10] Iso 1320: Acoustics - terminology. ISO, 2009.
- [11] Iso 3744: Acoustics - determination of sound power levels and sound energy levels of noise sources using sound pressure - engineering method for an essentially free field over a reflecting plane. ISO, 2010.
- [12] Iso 3746: Acoustics - determination of sound power levels and sound energy levels of noise sources using sound pressure - survey method using an enveloping measurement surface over a reflecting plane. ISO, 2010.

## Bibliography

- [13] Iso 3747: Acoustics - determination of sound power levels and sound energy levels of noise sources using sound pressure - engineering/survey method for use in situ in a reverberant environment. ISO, 2010.
- [14] Iso 3745: Acoustics - determination of sound power levels and sound energy levels of noise sources using sound pressure - precision method for anechoic room and hemi-anechoic rooms. ISO, 2012.
- [15] Jean F. Allard and N. Atalla. *Propagation of Sound in Porous Media: Modelling Sound Absorbing Materials*. Wiley, 2009.
- [16] Jean F. Allard, R. Bourdier, and A.M. Bruneau. The measurement of acoustic impedance at oblique incidence with two microphones. *Journal of Sound and Vibration*, 101(1):130 – 132, 1985.
- [17] Jean F. Allard and Yvan Champoux. In situ technique for the measurement of acoustic surface impedance. In *Audio Engineering Society Convention 86*, 1989.
- [18] Jean F. Allard, Yvan Champoux, and Jean Nicolas. Pressure variation above a layer of absorbing material and impedance measurement at oblique incidence and low frequencies. *The Journal of the Acoustical Society of America*, 86(2):766–770, 1989.
- [19] Jean F. Allard and B. Sieben. Measurements of acoustic impedance in a free field with two microphones and a spectrum analyzer. *Journal of the Acoustical Society of America*, 77(4):1617–1618, 1985.
- [20] Marc Aretz and Michael Vorländer. Efficient modelling of absorbing boundaries in room acoustic FE simulations. *Acta Acustica united with Acustica*, 96(6):1042–1050, 2010.
- [21] Tom G. H. Basten and Hans-Elias de Bree. Full bandwidth calibration procedure for acoustic probes containing a pressure and particle velocity sensor. *The Journal of the Acoustical Society of America*, 127(1):264–270, 2010.
- [22] Chuan-Xing Bi, Wang-Lin Lin, and Young-Bin Zhang. Determination of plane-wave reflection coefficients from particle velocity measurements. In *Proceedings of Internoise*, 2015.
- [23] Karlheinz Biehn, Werner Frommhold, Siegbert Gruhl, Ulrich Kurze, Eberhard Lotze, Gottfried Meltzer, Roman Melzig-Thiel, Wolfgang Parthey, Werner Schirmer, Lothar Schmidt, and Erhard Seidel. *Technischer Lärmschutz*. Springer Science Business Media, 1996.
- [24] D.A. Bies and C.H. Hansen. *Engineering Noise Control: Theory and Practice, Fourth Edition*. Taylor & Francis, 2009.
- [25] Matthew G. Blevins. *Design and Optimization of Membrane-Type Acoustic Metamaterials*. PhD thesis, University of Nebraska-Lincoln, 2016.

## Bibliography

- [26] Laurens Boeckx, Gert Jansens, Walter Lauriks, and Gerrit Vermeir. The tamura method, a free field technique for scanning surfaces. *Proceedings Institute of Acoustics*, 25(5):123–129, 2003.
- [27] J Stuart Bolton, Srinivas Varanasi, Thomas Siegmund, and Ray Cipra. The low frequency performance of metamaterial barriers based on cellular structures. Technical Report 51, Publications of the Ray W. Herrick Laboratories, 2012.
- [28] Jeffrey Borish and James B. Angell. An efficient algorithm for measuring the impulse response using pseudorandom noise. *J. Audio Eng. Soc.*, 31(7/8):478–488, 1983.
- [29] Eric Brandão, Arcanjo Lenzi, and Stephan Paul. A review of the in situ impedance and sound absorption measurement techniques. *Acta Acustica united with Acustica*, 101(3):443–463, 2015.
- [30] Yangyang Chen, Guoliang Huang, Xiaoming Zhou, Gengkai Hu, and Chin-Teh Sun. Analytical coupled vibroacoustic modeling of membrane-type acoustic meta-materials: Membrane model. *The Journal of the Acoustical Society of America*, 136(3):969–979, 2014.
- [31] Daniel Fernandez Comesana, Ben Piper Triantafillos Koukoulas, and Erik-Jan Jongh. Calibration of a acoustic particle velocity sensors using a laser based method. In *23rd International Congress on Sound and Vibration*, pages 1–8, 2016.
- [32] Daniel Fernandez Comesana, Emiel Tijs, Martijn Janszen, and Graciano Carrillo Pousa. A novel in-situ calibration method for acoustic particle velocity sensors based on a surface velocity. 2015.
- [33] TJ Cox and P D’Antonio. *Acoustic absorbers and diffusers: theory, design and application*, volume 12. Routledge Taylor & Francis, 2009.
- [34] J.C. Davies and K.A. Mulholland. An impulse method of measuring normal impedance at oblique incidence. *Journal of Sound and Vibration*, 67(1):135 – 149, 1979.
- [35] H.-E. De Bree. The microflow: An acoustic particle velocity sensor. *Acoustics Australia*, 31(3):91–94, 2003.
- [36] H.-E. De Bree. An overview of microflow technologies. *Acta Acustica (Stuttgart)*, 89(1):163–172, 2003.
- [37] Hans-Elias de Bree, Erik Druyvesteyn, and Ron Raangs. A low cost intensity probe. In *Audio Engineering Society Convention 110*, 2001.
- [38] Lieven de Geetere. *Analysis and improvement of the experimental techniques to assess the acoustical reflection properties of boundary surfaces*. Phd thesis, KU Leuven, 2004.

## Bibliography

- [39] M.E. Delany and E.N. Bazley. Acoustical properties of fibrous absorbent materials. *Applied Acoustics*, 3(2):105 – 116, 1970.
- [40] Thomas D. Rossing (eds.). *Springer Handbook of Acoustics*. Springer-Verlag New York, 2nd edition, 2014.
- [41] S.J. Elliott. Errors in acoustic intensity measurements. *Journal of Sound and Vibration*, 78(3):439 – 443, 1981.
- [42] F. Fahy. *Sound intensity*. Elsevier Applied Science, 1989.
- [43] George V. Frisk, Alan V. Oppenheim, and David R. Martinez. A technique for measuring the plane-wave reflection coefficient of the ocean bottom. *The Journal of the Acoustical Society of America*, 68(2):602–612, 1980.
- [44] Joseph W. Goodman. *Introduction to Fourier optics*. Roberts and Co., 3rd edition, 2005.
- [45] Jürgen Hald. Basic theory and properties of statistically optimized near-field acoustical holography. *The Journal of the Acoustical Society of America*, 125(4):2105–2120, 2009.
- [46] N. Hashimoto, M. Katsura, Y. Nishikawa, K. Katagihara, T. Torii, and M. Nakata. Experimental study on sound insulation of membranes with small weights for application to membrane structures. *Applied Acoustics*, 48(1):71 – 84, 1996.
- [47] Norihisa Hashimoto, Mitsuhiro Katsura, Masahito Yasuoka, and Hiroyosi Fujii. Sound insulation of a rectangular thin membrane with additional weights. *Applied Acoustics*, 33(1):21 – 43, 1991.
- [48] David Havelock, Sonoko Kuwano, and Michael Vorländer, editors. *Handbook of Signal Processing in Acoustics*. Springer Science Business Media, 2008.
- [49] B.P. Hildebrand and B.B. Brenden. *An introduction to acoustical holography*. Plenum Press, 1972.
- [50] Tai-Yun Huang, Chen Shen, and Yun Jing. Membrane- and plate-type acoustic metamaterials. *The Journal of the Acoustical Society of America*, 139(6):3240–3250, 2016.
- [51] F. Jacobsen. A note on instantaneous and time-averaged active and reactive sound intensity. *Journal of Sound and Vibration*, 147(3):489 – 496, 1991.
- [52] Finn Jacobsen, Vicente Cutanda, and Peter M. Juhl. A numerical and experimental investigation of the performance of sound intensity probes at high frequencies. *The Journal of the Acoustical Society of America*, 103(2):953–961, 1998.
- [53] Finn Jacobsen and Hans-Elias de Bree. A comparison of two different sound intensity measurement principles. *The Journal of the Acoustical Society of America*, 118(3):1510–1517, 2005.

## Bibliography

- [54] Finn Jacobsen and Virginie Jaud. A note on the calibration of pressure-velocity sound intensity probes. *The Journal of the Acoustical Society of America*, 120(2):830–837, 2006.
- [55] Dominik Jacquelin. Messtechnische Charakterisierung einer akustischen p–v–Sonde. Bachelor thesis, TU Wien, March 2015.
- [56] Wen-Qian Jing, Yong-Bin Zhang, and Chuan-Xing Bi. A nearfield acoustic holography-based method for measuring the sensitivity of a particle velocity sensor. *Acta Acustica united with Acustica*, 101(4):855–858, 2015.
- [57] Barbara Kaltenbacher, Manfred Kaltenbacher, and Imbo Sim. A modified and stable version of a perfectly matched layer technique for the 3-d second order wave equation in time domain with an application to aeroacoustics. *Journal of Computational Physics*, 235:407 – 422, 2013.
- [58] M. Kaltenbacher. *Numerical Simulation of Mechatronic Sensors and Actuators*. Springer, Berlin, 3. edition, 2015.
- [59] L.E. Kinsler and A.R. Frey. *Fundamentals of Acoustics*, volume 16. Wiley, 1962.
- [60] C. Klein and A. Cops. Angle dependence of the impedance of a porous layer. *Acta Acustica united with Acustica*, 44(4):258–264, 1980.
- [61] Takeshi Komatsu. Improvement of the delany-bazley and miki models for fibrous sound-absorbing materials. *Acoustical Science and Technology*, 29(2):121–129, 2008.
- [62] E.R. Kuipers. *Measuring Sound Absorption Using Local Field Assumptions*. Phd thesis, 2013.
- [63] E.R. Kuipers, Y.H. Wijnant, and A. de Boer. Measuring oblique incidence sound absorption using a local plane wave assumption. *Acta acustica united with Acustica*, 100:205 – 214, 2014.
- [64] G. Kurtze. Light-weight walls with high transmission loss. *Acta Acustica united with Acustica*, 9(6):441–445, 1959.
- [65] H. Kuttruff. *Acoustics: An Introduction*. Taylor & Francis, 2007.
- [66] F. Langfeldt, W. Gleine, and O. von Estorff. Analytical model for low-frequency transmission loss calculation of membranes loaded with arbitrarily shaped masses. *Journal of Sound and Vibration*, 349:315 – 329, 2015.
- [67] F. Langfeldt, J. Riecken, W. Gleine, and O. von Estorff. A membrane-type acoustic metamaterial with adjustable acoustic properties. *Journal of Sound and Vibration*, 373:1 – 18, 2016.

## Bibliography

- [68] R. Lanoye, H.-E. De Bree, W. Lauriks, and G. Vermeir. A practical device to determine the reflection coefficient of acoustic materials in-situ based on a microflow and microphone sensor. pages 2665–2675, 2004.
- [69] R. Lanoye, G. Vermeir, W. Lauriks, R. Kruse, and V. Mellert. Measuring the free field acoustic impedance and absorption coefficient of sound absorbing materials with a combined particle velocity-pressure sensor. *The Journal of the Acoustical Society of America*, 119(5):2826–2831, 2006.
- [70] R. Lerch, G.M. Sessler, and D. Wolf. *Technische Akustik: Grundlagen und Anwendungen*. Springer, 2009.
- [71] Jing-Fang Li and Murray Hodgson. Use of pseudo-random sequences and a single microphone to measure surface impedance at oblique incidence. *The Journal of the Acoustical Society of America*, 102(4):2200–2210, 1997.
- [72] Junfei Li, Xiaoming Zhou, Guoliang Huang, and Gengkai Hu. Acoustic metamaterials capable of both sound insulation and energy harvesting. *Smart Materials and Structures*, 25(4):045013, 2016.
- [73] Wang-Lin Lin, Chuan-Xing Bi, Michael Vorländer, Yong-Bin Zhang, and Robertus Opdam. In situ measurement of the absorption coefficient based on a time-domain subtraction technique with a particle velocity transducer. *Acta Acustica united with Acustica*, 102(5):945–954, 2016.
- [74] Wang-Lin Lin, Chuan-Xing Bi, and Yong-Bin Zhang. Measurement of reflection factor at oblique incidence with pressure-velocity transducers. *Noise Control Engineering Journal*, 64(3):379–387, 2016.
- [75] Guancong Ma, Min Yang, Songwen Xiao, Zhiyu Yang, and Ping Sheng. Acoustic metasurface with hybrid resonances. *Nat Mater*, 13(9):873–878, 2014.
- [76] F. J. MacWilliams and N. J. A. Sloane. Pseudo-random sequences and arrays. *Proceedings of the IEEE*, 64(12):1715–1729, 1976.
- [77] J. D. Maynard, E. G. Williams, and Y. Lee. Nearfield acoustic holography: I. theory of generalized holography and the development of nah. *The Journal of the Acoustical Society of America*, 78(4):1395–1413, 1985.
- [78] F. P. Mechel, M.L. Munjal, M. Vorländer, P. Költzsch, M. Ochmann, A. Cummings, W. Maysenhölder, and W. Arnold. *Formulas of Acoustics*. Springer Berlin Heidelberg, 2013.
- [79] Jun Mei, Guancong Ma, Min Yang, Zhiyu Yang, Weijia Wen, and Ping Sheng. Dark acoustic metamaterials as super absorbers for low-frequency sound. *Nature Communications*, 3:756, 2012.



## Bibliography

- [80] Jochen Metzger, Hendrik Husstedt, and Manfred Kaltenbacher. Characterization of the accmf-system for a simultaneous calibration technique. In *Proceedings of the 6th Congress of the Alps Adria Association*, October 2014.
- [81] Jochen Metzger and Manfred Kaltenbacher. Simultaneous calibration of all three acoustic particle velocity components of a pressure-velocity probe. In *Proceedings of Internoise*, September 2013.
- [82] Jochen Metzger and Manfred Kaltenbacher. Simultane Kalibrierung der drei Komponenten des Schnellesensors einer pv-Sonde mit Hilfe eines schwingenden Kolbens. In *Fortschritte der Akustik - DAGA 2014*, pages 638–639, 2014.
- [83] Jochen Metzger and Manfred Kaltenbacher. Simultaneous calibration method for a 3d particle velocity sensor. *Acta Acustica united with Acustica*, accepted for publication, 2017.
- [84] Jochen Metzger, Stefan Tschallener, and Manfred Kaltenbacher. Separation of an incoming and reflecting impulse for determining angle-dependent acoustic properties. In *Fortschritte der Akustik - DAGA 2016*, pages 802–805, 2016.
- [85] Yasushi Miki. Acoustical properties of porous materials-modifications of delany-bazley models-. *Journal of the Acoustical Society of Japan (E)*, 11(1):19–24, 1990.
- [86] M. Minten, A. Cops, and W. Lauriks. Absorption characteristics of an acoustic material at oblique incidence measured with the two-microphone technique. *Journal of Sound and Vibration*, 120(3):499 – 510, 1988.
- [87] Markus Müller-Trapet. *Measurement of surface reflection properties : concepts and uncertainties*. Phd thesis, RWTH Aachen, Dissertation, Berlin, 2015.
- [88] Markus Müller-Trapet, Pascal Dietrich, Marc Aretz, Jan van Gemmeren, and Michael Vorländer. On the in situ impedance measurement with pu-probes-simulation of the measurement setup. *The Journal of the Acoustical Society of America*, 134(2):1082–1089, 2013.
- [89] Markus Müller-Trapet, Martin Pollow, and Michael Vorländer. Spherical harmonics as a basis for quantifying scattering and diffusing objects. In T, editor, *Proceedings to Forum Acusticum 2001, Aalborg*, volume 97, pages 117–117, Stuttgart, 2011. Hirzel.
- [90] Markus Müller-Trapet and Michael Vorländer. Signal processing for hemispherical measurement data. *Proceedings of Meetings on Acoustics*, 19(1), 2013.
- [91] Markus Müller-Trapet and Michael Vorländer. In-situ measurements of surface reflection properties. *Building Acoustics*, 21(2):167–174, 2014.
- [92] Markus Müller-Trapet and Michael Vorländer. Array processing methods for the determination of reflection properties of architectural surfaces. *The Journal of the Acoustical Society of America*, 137(4):2195–2195, 2015.

## Bibliography

- [93] E. Mommertz. Angle-dependent in-situ measurements of reflection coefficients using a subtraction technique. *Applied Acoustics*, 46(3):251 – 263, 1995.
- [94] Michael Möser, editor. *Messtechnik der Akustik*. Springer Science Business Media, 2010.
- [95] Christina J. Naify, Chia-Ming Chang, Geoffrey McKnight, and Steven Nutt. Transmission loss and dynamic response of membrane-type locally resonant acoustic metamaterials. *Journal of Applied Physics*, 108(11):114905, 2010.
- [96] Christina J. Naify, Chia-Ming Chang, Geoffrey McKnight, and Steven Nutt. Transmission loss of membrane-type acoustic metamaterials with coaxial ring masses. *Journal of Applied Physics*, 110(12):124903, 2011.
- [97] Christina J. Naify, Chia-Ming Chang, Geoffrey McKnight, and Steven R. Nutt. Scaling of membrane-type locally resonant acoustic metamaterial arrays. *The Journal of the Acoustical Society of America*, 132(4):2784–2792, 2012.
- [98] Christina J. Naify, Chia-Ming Chang, Geoffrey McKnight, Florian Scheulen, and Steven Nutt. Membrane-type metamaterials: Transmission loss of multi-celled arrays. *Journal of Applied Physics*, 109(10):104902, 2011.
- [99] Matthew A. Nobile and Sabih I. Hayek. Acoustic propagation over an impedance plane. *The Journal of the Acoustical Society of America*, 78(4):1325–1336, 1985.
- [100] Rob Opdam, Diemer de Vries, and Michael Vorländer. Angle-dependent reflection factor measurements of finite samples with an edge diffraction correction. In *Proceedings of Inter-Noise 2015 : the 2015 International Congress and Exposition on Noise Control Engineering, 9 - 12 August 2015, San Francisco, California, USA / [proc.ed.:] Courtney Burroughs*, pages 3387–3392, Springfield, Aug 2015. 44th International Congress and Exposition on Noise Control Engineering, San Francisco, Calif. (USA), 9 Aug 2015 - 12 Aug 2015, INCE-USA Business Office.
- [101] Rob Opdam, Sander Hoen, Diemar de Vries, and Michael Vorländer. Measurement of angle-dependent reflection coefficients with a microphone array and spatial fourier transform post-processing. In *AIA-DAGA 2013*, 2013.
- [102] World Health Organization. *Burden of Disease from Environmental Noise: Quantification of Healthy Life Years Lost in Europe*. WHO Europe, 2011.
- [103] Marco Ottink, Jonas Brunskog, Cheol-Ho Jeong, Efren Fernandez-Grande, Per Trojgaard, and Elisabet Tiana-Roig. In situ measurements of the oblique incidence sound absorption coefficient for finite sized absorbers. *The Journal of the Acoustical Society of America*, 139(1):41–52, 2016.
- [104] K. Uno Ingard Philip M. Morse. *Theoretical Acoustics*. McGraw Hill Book Company, 1968.

## Bibliography

- [105] Graciano Carrillo Pousa, Daniel Fernandez Comesana, David Perez Cabo, and Andres Priesto. Numerical study of an in-situ technique for measuring surface impedance and reflection coefficient of a locally reacting material with pressure-velocity probes. pages 1–9, 2016.
- [106] Shuibao Qi, Mourad Oudich, Yong Li, and Badreddine Assouar. Acoustic energy harvesting based on a planar acoustic metamaterial. *Applied Physics Letters*, 108(26):263501, 2016.
- [107] J. Rathsam and B. Rafaely. Analysis of absorption in situ with a spherical microphone array. *Applied Acoustics*, 89:273 – 280, 2015.
- [108] M. Ren and F. Jacobsen. Phase mismatch errors and related indicators in sound intensity measurement. *Journal of Sound and Vibration*, 149(2):341 – 347, 1991.
- [109] Philip Robinson and Ning Xiang. On the subtraction method for in-situ reflection and diffusion coefficient measurements. *The Journal of the Acoustical Society of America*, 127(3):EL99–EL104, 2010.
- [110] W. C. Sabine. *Collected Papers on Acoustics*, volume 34. Peninsula, 1992.
- [111] U. S. Shirahatti and Malcolm J. Crocker. Two microphone finite difference approximation errors in the interference fields of point dipole sources. *The Journal of the Acoustical Society of America*, 92(1):258–267, 1992.
- [112] Domenico Stanzial, Giorgio Sacchi, and Giuliano Schiffrer. Calibration of pressure-velocity probes using a progressive plane wave reference field and comparison with nominal calibration filters. *The Journal of the Acoustical Society of America*, 129(6):3745–3755, 2011.
- [113] V.B Svetovoy and I.A Winter. Model of the  $\mu$ -flown microphone. *Sensors and Actuators A: Physical*, 86(3):171 – 181, 2000.
- [114] Y. Takahashi, T. Otsuru, and R. Tomiku. In situ measurements of surface impedance and absorption coefficients of porous materials using two microphones and ambient noise. *Applied Acoustics*, 66(7):845 – 865, 2005.
- [115] Masayuki Tamura. Spatial fourier transform method of measuring reflection coefficients at oblique incidence. i: Theory and numerical examples. *The Journal of the Acoustical Society of America*, 88(5):2259–2264, 1990.
- [116] Masayuki Tamura, Jean F. Allard, and Denis Lafarge. Spatial fourier–transform method for measuring reflection coefficients at oblique incidence. ii. experimental results. *The Journal of the Acoustical Society of America*, 97(4):2255–2262, 1995.
- [117] Hongyan Tian, Xingzhe Wang, and You-he Zhou. Theoretical model and analytical approach for a circular membrane–ring structure of locally resonant acoustic metamaterial. *Applied Physics A*, 114(3):985–990, 2014.

## Bibliography

- [118] Stefan Tschallener. Aufbau eines Messplatzes zur In-situ Messung von akustischen Materialeigenschaften unter beliebigen Schalleinfallswinkeln. Bachelor thesis, TU Wien, July 2015.
- [119] Stefan Tschallener. Aufbau und Charakterisierung eines Messsystems nach der Tamura-Methode zur Ermittlung akustischer Materialeigenschaften unter beliebigen Schalleinfallswinkeln. Master thesis, TU Wien, February 2017.
- [120] CFS Userguide. web page — cfs userguide,, 2016. [Online; accessed 24-August-2016].
- [121] J.W. van Honschoten, V.B. Svetovoy, T.S.J. Lammerink, G.J.M. Krijnen, and M.C. Elwenspoek. Determination of the sensitivity behavior of an acoustic, thermal flow sensor by electronic characterization. *Sensors and Actuators A: Physical*, 112(1):1 – 9, 2004.
- [122] Srinivas Varanasi, J. Stuart Bolton, Thomas H. Siegmund, and Raymond J. Cipra. The low frequency performance of metamaterial barriers based on cellular structures. *Applied Acoustics*, 74(4):485 – 495, 2013.
- [123] S.S.S. Varanasi, S. Khandelwal, T. Siegmund, J.S. Bolton, and R.J. Cipra. Sound barrier systems, November 20 2014. US Patent App. 14/281,408.
- [124] I.L. Vér and L.L. Beranek. *Noise and vibration control engineering: principles and applications*, volume 97. John Wiley & Sons, 2006.
- [125] Michael Vorländer and Malte Kob. Performance, analysis and predictions in building acoustics practical aspects of mls measurements in building acoustics. *Applied Acoustics*, 52(3):239 – 258, 1997.
- [126] Xiaole Wang, Hui Zhao, Xudong Luo, and Zhenyu Huang. Membrane-constrained acoustic metamaterials for low frequency sound insulation. *Appl. Phys. Lett.*, 108(4):041905, 2016.
- [127] Earl G. Williams. *Fourier Acoustics: Sound Radiation and Nearfield Acoustical Holography*. Academic Press, 1999.
- [128] George S. K. Wong and Tony F. W. Embleton. Arrangement for precision reciprocity calibration of condenser microphones. *The Journal of the Acoustical Society of America*, 66(5):1275–1280, 1979.
- [129] George S. K Wong, Tony F. W Embleton, and American Institute of Physics. *AIP handbook of condenser microphones : theory, calibration, and measurements*. New York : American Institute of Physics, 1995.
- [130] Min Yang, Guancong Ma, Zhiyu Yang, and Ping Sheng. Coupled membranes with doubly negative mass density and bulk modulus. *Phys. Rev. Lett.*, 110(13):134301, 2013.

## Bibliography

- [131] Z. Yang, H. M. Dai, N. H. Chan, G. C. Ma, and Ping Sheng. Acoustic metamaterial panels for sound attenuation in the 50–1000 hz regime. *Applied Physics Letters*, 96(4):041906, 2010.
- [132] Z. Yang, Jun Mei, Min Yang, N. H. Chan, and Ping Sheng. Membrane-type acoustic metamaterial with negative dynamic mass. *Phys. Rev. Lett.*, 101(20):204301, 2008.
- [133] Alfio Yori and Michael Möser. A measurement method for the sound absorption coefficient for arbitrary sound fields and surfaces. *Acta Acustica united with Acustica*, 101(4):668–674, 2015.
- [134] Mutsushige Yuzawa. A method of obtaining the oblique incident sound absorption coefficient through an on-the-spot measurement. *Applied Acoustics*, 8(1):27 – 41, 1975.
- [135] Yong-Bin Zhang, Wang-Lin Lin, and Chuan-Xing Bi. A technique based on the equivalent source method for measuring the surface impedance and reflection coefficient of a locally reacting material. In *Internoise 2014*, 2014.
- [136] Yuguang Zhang, Jihong Wen, Yong Xiao, Xisen Wen, and Jianwei Wang. Theoretical investigation of the sound attenuation of membrane-type acoustic metamaterials. *Physics Letters A*, 376(17):1489 – 1494, 2012.
- [137] C. Zwicker and C.W. Kosten. *Sound absorbing materials*. Elsevier Pub. Co., 1949.

# Curriculum Vitae

## Personal Data

Name	Jochen Metzger
Date of birth	September 2, 1987
Place of birth	Schillingsfürst, Germany

## Education

06/2006	General qualification for university entrance, Reichsstadt-Gymnasium Rothenburg o. d. T., Rothenburg o. d. T., Germany Final exam in mathematics, hystory, biology and german
10/2006 to 06/2012	Dipl.-Ing. mechatronics FAU Erlangen-Nuremberg, Erlangen, Germany Specialization: sensor technologies and optics graduated with honors

## Professional Experience

05/2011 to 09/2011	Internship at BMW Group, Munich
08/2012 to 07/2016	Research and Teaching Assistant Institute of Mechanics and Mechatronics TU Wien, Austria
08/2016 to 03/2017	Research Assistant Institute of Mechanics and Mechatronics TU Wien, Austria